International Journal of Biomaterials

Synthetic Polymers for Biomedical Applications

Lead Guest Editor: Qiang Wei
Guest Editors: Nan-Nan Deng, Junling Guo, and Jie Deng

Synthetic Polymers for Biomedical Applications

International Journal of Biomaterials

Synthetic Polymers for Biomedical Applications

Lead Guest Editor: Qiang Wei
Guest Editors: Nan-Nan Deng, Junling Guo, and Jie Deng

Copyright © 2018 Hindawi. All rights reserved.

This is a special issue published in "International Journal of Biomaterials." All articles are open access articles distributed under the Creative Commons Attribution License, which permits unrestricted use, distribution, and reproduction in any medium, provided the original work is properly cited.

Editorial Board

Lawrence Bonassar, USA
Wen-Cheng Chen, Taiwan
Traian V. Chirila, Australia
Sanjukta Deb, UK
Nicholas Dunne, Ireland
Carlo Galli, Italy
Paul Hatton, UK
Esmaiel Jabbari, USA
Rosalind Labow, Canada
Chwee Teck Lim, Singapore
Feng-Huei Lin, Taiwan
Ravin Narain, Canada
Vijaya Kumar Rangari, USA
Sang-Hoon Rhee, Republic of Korea
Colin Scotchford, UK
Alexander Seifalian, UK
Tai Horng Young, Taiwan

Contents

Hindawi
International Journal of Biomaterials
Volume 2018, Article ID 7158621, 2 pages
https://doi.org/10.1155/2018/7158621

Editorial

Synthetic Polymers for Biomedical Applications

Qiang Wei,[1] **Nan-Nan Deng**,[2] **Junling Guo**,[2] **and Jie Deng**[3]

[1]*Max Planck Institute for Medical Research, Heidelberg, Germany*
[2]*Harvard University, Cambridge, MA, USA*
[3]*University of Freiburg, Freiburg, Germany*

Correspondence should be addressed to Qiang Wei; wei.weiqiang@gmail.com

Qiang Wei, Nan-Nan Deng, Junling Guo, and Jie Deng contributed equally to this work.

Received 13 March 2018; Accepted 13 March 2018; Published 24 April 2018

Copyright © 2018 Qiang Wei et al. This is an open access article distributed under the Creative Commons Attribution License, which permits unrestricted use, distribution, and reproduction in any medium, provided the original work is properly cited.

Polymers have been emerging to be the cornerstones for therapeutic applications as well as the largest and versatile class of biomaterials. Synthetic polymers can be designed and synthesized with a broad variety of structures and appropriate physical and chemical properties, which are of increasing interest in a wide range of biomedical applications as diverse as tissue engineering, drug delivery, therapeutics, diagnostics, and so on.

Since the last decade, the methods of polymer synthesis, processing, and characterization are developing rapidly, which bring both challenges and opportunities to design novel polymeric biomaterials as well as to understand the biological behaviors between biological systems and polymeric materials. Therefore, we launch this special issue, including two review articles and four research articles, to summarize the application of synthetic polymers in biomedical engineering and to illustrate the new development of polymeric biomaterials.

One review article "Strain and Vibration in Mesenchymal Stem Cells" focuses on the effect of various culture conditions and strain or vibration parameters to review the response of mesenchymal stem cells to vibration and cyclic tension and then discuss how polymer scaffolds influence cell response to vibration and strain. The other review article "Scaffolds for Pelvic Floor Prolapse: Logical Pathways" highlights the recently developed macroporous monofilament meshes and electrospinning emerged method, which may fill the gap in the market to treat pelvic organ prolapse. These two review articles indicate the importance of synthetic polymer scaffold in basic research and therapeutics, respectively.

The research articles in this issue extend the application of synthetic polymers in both basic research and therapeutics. Synthetic poly(lactic-co-glycolic acid) (PLGA) is widely considered as a base material for biomedical applications due to its good biocompatibility and degradability. In the article "Influence of Processing Conditions on the Mechanical Behavior and Morphology of Injection Molded Poly(lactic-co-glycolic acid) 85:15," an overview is provided among processing conditions, morphology, and mechanical property relationship of injection molded PLGA. Based on the study of mechanics, PLGA is further processed by injection molding as craniofacial bioresorbable medical devices in the article "Effect of Injection Molding Melt Temperatures on PLGA Craniofacial Plate Properties during *In Vitro* Degradation." The mechanical and physicochemical properties of the PGA plates are evaluated in detail during in vitro degradation. G. Rijal et al. fabricated 3D porous scaffolds via PLGA and another biodegradable synthetic polymer polycaprolactone (PCL) in the article "Application of Synthetic Polymeric Scaffolds in Breast Cancer 3D Tissue Cultures and Animal Tumor Models." It has proven that cancer cells grown on 3D polymeric scaffolds exhibit distinct survival, morphology, and proliferation compared to those on 2D polymeric surfaces. Tumor models produced via these 3D scaffolds have obvious advantages in anticancer drug screening, which can facilitate the observations of cancer biomarker expression, molecular regulation of cancer progression, and drug efficacies across tumors at similar sizes and developmental stages. Polyethylene glycol (PEG) is another one of the most commonly used synthetic polymers for biomaterials. In the article

"Efficient Self-Assembly of mPEG End-Capped Porous Silica as a Redox-Sensitive Nanocarrier for Controlled Doxorubicin Delivery," porous nanosilica particles are modified with PEG shell via disulfide bridges and supramolecular interaction for drug delivery, with benefits of enhanced drug loading capacity and decreased risk of systemic toxicity.

In summary, this special issue connects the synthetic polymers to biomaterials science and engineering. We sincerely hope that the readers enjoy reading the presented original research work in this special issue and get inspired for their future studies.

Acknowledgments

We appreciate the great effort and the kind contributions from the authors and reviewers to this special issue.

Qiang Wei
Nan-Nan Deng
Junling Guo
Jie Deng

Hindawi
International Journal of Biomaterials
Volume 2018, Article ID 1575438, 8 pages
https://doi.org/10.1155/2018/1575438

Research Article

Efficient Self-Assembly of mPEG End-Capped Porous Silica as a Redox-Sensitive Nanocarrier for Controlled Doxorubicin Delivery

Anh Khoa Nguyen,[1,2,3] Thi Hiep Nguyen,[4] Bui Quoc Bao,[1,2] Long Giang Bach,[1,5] and Dai Hai Nguyen[1,2]

[1] *Graduate University of Science and Technology, Vietnam Academy of Science and Technology, Hanoi 100000, Vietnam*
[2] *Institute of Applied Materials Science, Vietnam Academy of Science and Technology, 01 TL29, District 12, Ho Chi Minh City 700000, Vietnam*
[3] *Tra Vinh University, No. 126, Nguyen Thien Thanh, Ward 5, Tra Vinh City, Tra Vinh Province 940000, Vietnam*
[4] *Tissue Engineering and Regenerative Medicine Group, Department of Biomedical Engineering, International University, Vietnam National University-HCMC (VNU-HCMC), Ho Chi Minh City 70000, Vietnam*
[5] *Nguyen Tat Thanh University, 300A Nguyen Tat Thanh, District 4, Ho Chi Minh City 700000, Vietnam*

Correspondence should be addressed to Dai Hai Nguyen; nguyendaihai0511@gmail.com

Received 5 December 2017; Accepted 24 January 2018; Published 1 March 2018

Academic Editor: Nan-Nan Deng

Copyright © 2018 Anh Khoa Nguyen et al. This is an open access article distributed under the Creative Commons Attribution License, which permits unrestricted use, distribution, and reproduction in any medium, provided the original work is properly cited.

Porous nanosilica (PNS) has been regarded as a promising candidate for controlled delivery of anticancer drugs. Unmodified PNS-based nanocarriers, however, showed a burst release of encapsulated drugs, which may limit their clinical uses. In this report, PNS was surface conjugated with adamantylamine (ADA) via disulfide bridges (-SS-), PNS-SS-ADA, which was further modified with cyclodextrin-poly(ethylene glycol) methyl ether conjugate (CD-mPEG) to form a core@shell structure PNS-SS-ADA@CD-mPEG for redox triggered delivery of doxorubicin (DOX), DOX/PNS-SS-ADA@CD-mPEG. The prepared PNS-SS-ADA@CD-mPEG nanoparticles were spherical in shape with an average diameter of 55.5 ± 3.05 nm, a little larger than their parentally PNS nanocarriers, at 49.6 ± 2.56 nm. In addition, these nanoparticles possessed high drug loading capacity, at 79.2 ± 3.2%, for controlled release. The release of DOX from DOX/PNS-SS-ADA@CD-mPEG nanoparticles was controlled and prolonged up to 120 h in PBS medium (pH 7.4), compared to less than 40 h under reducing condition of 5 mM DTT. Notably, the PNS-SS-ADA@CD-mPEG was a biocompatible nanocarrier, and the toxicity of DOX was dramatically reduced after loading drugs into the porous core. This redox-sensitive PNS-SS-ADA@CD-mPEG nanoparticle could be considered a potential candidate with high drug loading capacity and a lower risk of systemic toxicity.

1. Introduction

Over the last several years, an increased amount of porous nanosilica (PNS) has been designed and developed owing to its high biocompatibility and biodegradability, tunable pore size, controllable morphology and easily modifiable surfaces, high chemical and thermal stabilities, straightforward preparation, and ability to carry various guest molecules with the porous pores [1–4]. The unique structure of PNS allows it to effectively encapsulate different guest molecules within the pores and protect them from enzymatic degradation [5–7]. However, encapsulated drugs would burst release from the unmodified PNS nanoparticles, leading to the loss of drugs that reach cancerous cells. In order to overcome this limitation, multifunctional polymer-modified PNS is one of the most critical insights; both interfacial properties of the modified nanocarriers can be engineered and thermal and mechanical features of polymers can be improved at the same

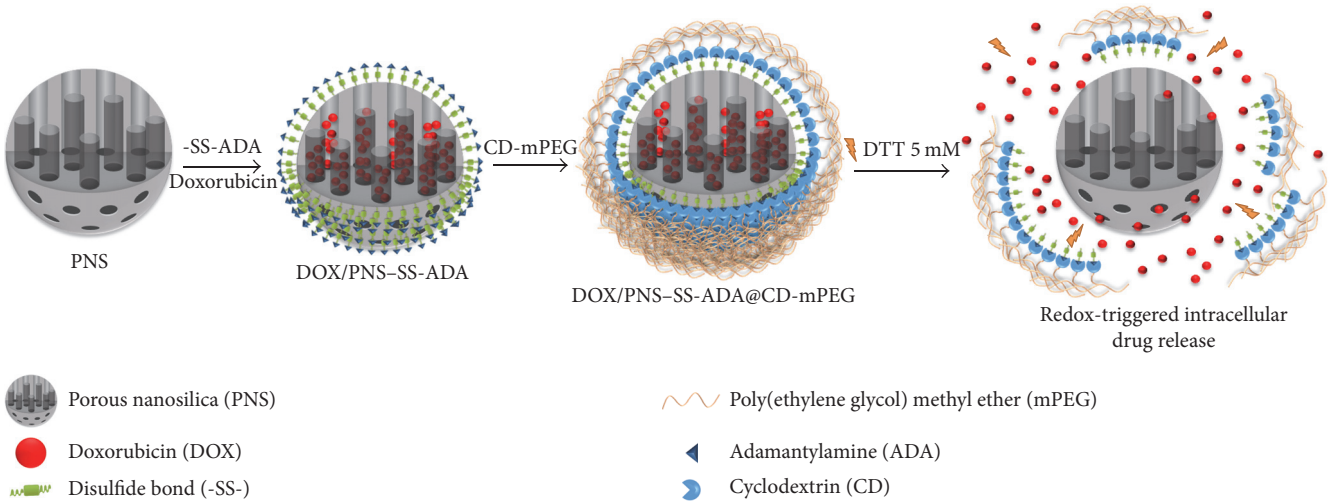

Figure 1: Schematic showing the formation of redox-responsive DOX/PNS-SS-ADA@CD-mPEG nanocarriers.

time. Nevertheless, this preparation can control and delay the rate of drug release instead of deciding when or where to deliver drugs [7, 8].

Recently, stimuli-sensitive PNS has attracted enormous interests due to its ability to respond to both internal stimuli, such as pH, redox potential, and temperature, and external stimuli, including light, magnetic fields, and ultrasound. Therefore, encapsulated drugs can be triggered by using appropriate stimuli [9–13]. The redox stimulus among those stimuli is one of the most effective strategies because the concentration of glutathione (GSH) in cancer cells (2–10 mM) is 100 to 1000-fold higher than that in normal healthy cells (1-2 μM). This phenomenon could offer an opportunity for redox-responsive system to release anticancer drugs at the targeted tumor sites, in order words [14–16]. For instance, Wang et al. modified PNS with polyethylene glycol (PEG) through disulfide bonds to achieve on-demand controlled release of a model drug rhodamine B (RhB). The results of *in vitro* assay showed that RhB was released dramatically under 10 mM GSH condition. Plus, the biocompatibility of the modified PNS nanoparticles increased with increasing surface PEG density [17, 18]. Wang and coworkers also developed a redox and pH dual-responsive nanocarrier for site-specific drug delivery, in which poly(acrylic acid) (PAA) was grafted in the outlets of PNS through cleavable disulfide bonds. RhB was also significantly released in GSH condition or pH 5.0 PBS. This PNS-SS-PAA nanoparticle exhibited dual-responsive drug release property and can be further used as a promising candidate for the treatment of cancer [19]. The complex structure of modified PNS delivery systems, in particular, was capable of loading high levels of drugs. Notably, if the pore entrances of PNS nanosystems have firstly been blocked by caps before drug encapsulation, an amount of nonencapsulated drug would increase [7].

In this study, we prepared potential PNS-based redox-responsive nanocarriers for controlled drug release. The surface of PNS was first modified with adamantylamine (ADA) via disulfide linkages (-SS-) and further functionalized with cyclodextrin-poly(ethylene glycol) methyl ether conjugate (CD-mPEG) via a strong complexation of ADA and CD, PNS-SS-ADA@CD-mPEG. Furthermore, DOX was used to evaluate drug loading into the PNS-SS-ADA@CD-mPEG nanoparticles (Figure 1). The obtained samples were characterized by proton nuclear magnetic resonance (^{1}H NMR), Fourier transform infrared (FTIR), thermogravimetric analysis (TGA), N_2 adsorption-desorption (BET), and transmission electron microscope (TEM). Especially, dithiothretol (DTT) was used to reduce –SS- in PNS-SS-ADA@CD-mPEG. Additionally, MTT assay was performed to determine whether the PNS-SS-ADA@CD-mPEG nanoparticle may reduce the toxicity to HeLa cells of DOX. This study is expected to create a redox-sensitive nanocarrier with high drug loading capacity and low systemic toxicity for controlled drug delivery.

2. Materials and Methods

2.1. Materials. Tetraethyl orthosilicate (TEOS, 98%), *p*-toluenesulfonyl chloride (TsCl), ADA, doxorubicin (DOX, 99%), mPEG (Mw 5000), DTT, 1-ethyl-3-(3-dimethylaminopropyl) carbodiimide (EDC, 97%), N,N-dimethyl formamide (DMF), and ethylenediamine (EDA, 99%) were purchased from Sigma-Aldrich (St. Louis, MO, USA). Cetyltrimethylammonium bromide (CTAB, 99%) was purchased from Merck (USA). DTDP (99%), 3-aminopropythiethoxysilane (APS, 99%), and 4-nitrophenyl chloroformate (PNC, 97%) were purchased from Acros Organics (Geel, Belgium). β-CD was purchased from TCI Co. (Tokyo, Japan). All chemicals were used as received without further purification.

2.2. Preparation of PNS-SS-ADA. According to the literature with minor modification, the overall process of PNS-SS-ADA preparation can be described in four main steps [7]. (1) the synthesis of PNS was performed by sol-gel method.

Briefly, deionized water (diH_2O, 64 mM), ethanol (0.2 mol), CTAB (7.1 mmol), and 2.8% NH_3 solution (0.9 mmol) were mixed at 60°C under stirring for 30 min. TEOS solution (35.8 mmol) was added dropwise into the surfactant solution under constant stirring, and the reaction was continued for 2 h and then filtered. The filtrate was dialyzed using a dialysis membrane (MWCO 6–8 kDa, Spectrum Laboratories, Inc., USA) against diH_2O for 4 days at room temperature and later lyophilized to collect PNS. (2) The preparation of PNS-NH_2 was carried out by mixing APS (5.7 mmol) and PNS (1 g) dissolved in methanol (4 mL); the reaction was kept at 30°C for 8 h before starting sonication for 30 min. Thus, the solution was dialyzed for 4 days against 2 M acetic acid, ethanol (1 v/v, 250 mL), and then immersed into diH_2O for a day. The solution was freeze-dried to form PNS-NH_2 as a white powder. (3) The prepared PNS-NH_2 (1 g) and EDC (0.14 mL) were dissolved together into diH_2O (20 mL) for 10 min. Thereafter, DTDP (0.77 mmol) dissolved in 20 mL of DMF was added to the mixture and the reaction was maintained for 24 h. The samples were purified by a dialysis membrane (MWCO 6–8 kDa) against diH_2O at room temperature for 4 days, followed by lyophilizaytion to obtain PNS-SS-COOH. (4) The obtained PNS-SS-COOH (1 g) and ADA solution (0.77 mmol) were mixed together under stirring, followed by the addition of EDC (0.64 mmol). The reaction was stirred at room temperature for 2 h and filtered. The sample was dialyzed at room temperature and finally lyophilized to get PNS-SS-ADA.

2.3. Preparation of CD-mPEG Conjugate and DOX/PNS-SS-ADA@CD-mPEG. The synthesis of CD-mPEG was carried out in four main steps [7]: (1) mPEG-NH_2 was fabricated under controlled temperature and vacuum conditions. Initially, mPEG (0.16 mmol) was melted down at 65°C under vacuum. Thus, PNC (0.19 mmol) was added to the above mPEG solution under constant stirring for 6 h, followed by the addition of 20 mL of THF solution. The obtained mPEG-PNC was gently dropped into EDA solution (0.23 mmol) and the mixture was stirred at room temperature for 24 h. The solution was dialyzed using dialysis membrane (MWCO 3.5 kDa) and then lyophilized to obtain mPEG-NH_2. (2) β-CD (26.4 mmol) and 10 mL of NaOH solution (8.2 M) were both dissolved in diH_2O (200 mL) under constant stirring for 10 min. TsCl (26.4 mmol) dissolved in 15 mL of acetonitrile was added to the mixture and the reaction was maintained at 25°C for 2 h. The pH value of the solution was adjusted to 8.0. The solid product was collected at 5–8°C for 24 h, achieved under vacuum at room temperature, and dried at 70°C for 2-3 days. (3) In order to synthesize CD-NH_2, CD-OTs (1 mmol) was dispersed in 30 mL of DMF under stirring condition, followed by the addition of EDA (30 mmol). The reaction was carried out for 24 h at 75°C under conditions of stirring and nitrogen flushing. The mixture was evaporated and precipitated in acetone solution (500 mL) for several times and, in addition, the solid product was later dried under vacuum to obtain CD-NH_2. (4) Both mPEG-NH_2 and CD-NH_2 were used with the support of EDC chemistry to obtain CD-mPEG. In detail, CD-NH_2 (7.4 μmol) and EDC (0.09 mmol) were dissolved in 10 mL of diH_2O under constant stirring, followed by the addition of mPEG-NH_2 (0.1 mmol) into the above mixture. After 24 h, the solution was filtered and dialyzed (MWCO 6–8 kDa) for 4 days and finally freeze-fried to collect CD-mPEG for further synthesis.

DOX was encapsulated into the PNS-SS-ADA nanoparticle by a sonication method. First, 5 mg of DOX and 20 mg of PNS-SS-ADA were stirred in diH_2O and sonicated for 10 min. Next, CD-mPEG solution was added to the mixture, sonicated for 10 min, and stirred overnight. The sample was further purified by dialysis membrane (MWCO 3.5 kDa) against diH_2O for 3 h and then lyophilized.

To prepare the empty PNS-SS-ADA@CD-mPEG nanoparticles, the same procedure was employed except the addition of DOX.

2.4. Characterization. Bruker Avance 500 (Bruker Co., USA) was used to record proton NMR spectroscopy of PNS-SS-ADA and CD-mPEG using D_2O as a solvent. FTIR spectra of PNS, PNS-SS-ADA, and PNS-SS-ADA@CD-mPEG were recorded on a Bruker Equinox 55 FTIR (Bruker Co., USA) in order to investigate the presence of SS-ADA and CD-mPEG on the surface of PNS nanoparticles. TGA was carried out using TG Analyzer (Perkin Elmer Pryris 1, USA). N_2 adsorption-desorption isotherms were measured using a NOVA 1000e system (Quantachrome Instruments, USA). The samples were outgassed for 3 h at 150°C before the measurements. Morphology and size of PNS and PNS-SS-ADA@CD-mPEG nanoparticles were imaged by TEM using JEM-1400 (JEOL, Tokyo, Japan) at an accelerating voltage of 300 kV. The samples for TEM observations were prepared by placing a drop of solution in diH_2O (1 mg/mL) onto a carbon-copper grid (300 mesh, Ted Pella, Inc., USA) and air-dried for 10 min.

2.5. DOX Loading Contents and In Vitro DOX Release. The DOX-loaded PNS-SS-ADA@CD-mPEG (DOX/PNS-SS-ADA@CD-mPEG) nanocarriers were prepared using equilibrium dialysis. The DOX loading efficiency (DLE) and DOX loading capacity (DLC) were quantified indirectly from the amount of unloaded DOX ($W_{\text{U-DOX}}$), which was evaluated using a UV-Vis spectrophotometer (NIR-V670, JASCO, Japan). Initially, fresh DOX was stirred in dH_2O to obtain a series of different known concentrations (0–60 μg/mL), which were used as standard samples. The absorbance of the standard and dialysis solutions was recorded at 495 nm using a V-750 UV/Vis spectrophotometer (Jasco Co., Tokyo, Japan). The following equations were used to calculate the DLE and DLC:

$$\text{DLE}\,(\%) = \frac{(5 - W_{\text{U-DOX}})}{5} * 100,$$
$$\text{DLC}\,(\%) = \frac{(5 - W_{\text{U-DOX}})}{(W_{\text{PNS-SS-ADA@CD-mPEG}} + 5 - W_{\text{U-DOX}})} * 100, \quad (1)$$

where 5 mg is the initial amount of DOX for loading experiment; $W_{\text{U-DOX}}$ is the total amount of unloaded DOX in the

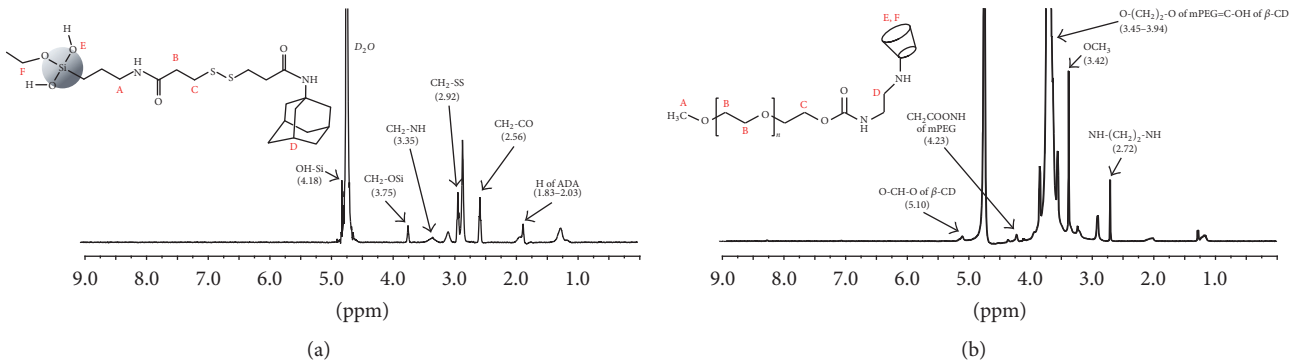

Figure 2: ^{1}H NMR spectra: PNS-SS-ADA (a); CD-mPEG (b).

dialysis solution; $W_{\text{PNS-SS-ADA@CD-mPEG}}$ is the dried weight of polymer in the nanocarrier.

DOX release kinetics from DOX/PNS-SS-ADA@CD-mPEG nanocarriers were conducted in PBS (10 mM, pH 7.4). Each sample (1 mL) was independently transferred into dialysis bags (MWCO 3.5 kDa). These sample bags were immersed in fresh media (14 mL, PBS, and pH 7.4) under constant stirring at 37°C. At specific time intervals, the release medium (14 mL) was collected and an equivalent amount of fresh medium was added. The amount of DOX released was determined using UV-Vis spectrophotometer as mentioned previously [20], especially, the release of DOX from DOX/PNS-SS-ADA@CD-mPEG under reducing condition (5 mM DTT).

2.6. MTT Viability Test. In order to evaluate the cytotoxicity of DOX/PNS-SS-ADA@CD-mPEG, the MTT assay was carried out. HeLa cells (ATCC, Manassas, VA, USA) were seeded in wells of 96-well plates (Sigma-Aldrich Co., St. Louis, MO, USA) with a density of 1×10^4 cells/well in 130 μL of DMEM (Dulbecco's Modified Eagle's medium, Acros Organics, Geel, Belgium) supplemented with 10% Fetal Bovine Serum (FBV) and 1% penicillin-streptomycin, and cultured at 37°C for a day. The media were removed, and thus the cells were incubated with media containing various sample concentrations for later 48 h, followed by removing media and washing twice with PBS.

MTT solution (25 μL, 2 mg/mL) and culture medium (130 μL) were added to each well. The cells were cultured for further 3 h, followed by adding DMSO (130 μL) into each well to dissolve the precipitated purple formazan in 15 min. The samples were then transferred into new transparent 96-wells plates and the absorbance at 570 nm was recorded using a multiplate reader (SpectraMax M2E, Molecular Devices Co., USA).

2.7. Statistical Analysis. The data were expressed as mean ± standard deviation. The statistical data evaluation was performed using Microsoft® Excel.

3. Results and Discussion

3.1. Characterization of PNS-SS-ADA@CD-mPEG. PNS nanoparticles were synthesized using the sol-gel technique

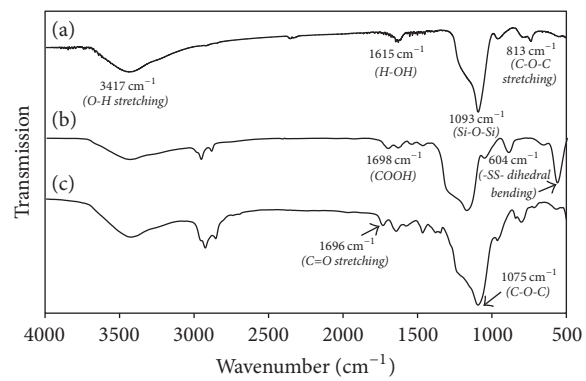

Figure 3: FTIR spectra: PNS (a) [7]; PNS-SS-ADA (b) [7]; PNS-SS-ADA@CD-mPEG (c).

reported in previous literature [21]. Figure 2 shows the proton NMR with assigned protons of PNS-SS-ADA and CD-mPEG. The peak at 4.67 ppm corresponded to D_2O as a solvent. As shown in Figure 2(a), protons at 3.35 ppm (peak A), 2.56 ppm (peak B), 2.92 ppm (peak C), 1.83–2.03 ppm (peak D), 4.18 ppm (peak E), and 3.75 ppm (peak F) were assigned to CH_2-NH, CH_2-CO, CH_2-SS, H of ADA, OH-Si, and CH_2-OSi groups, respectively. The presence of all these signals indicated the successful preparation of PNS-SS-ADA.

The ^{1}H NMR spectrum of CD-mPEG conjugate presents peaks at 3.42 ppm (peak A), 3.45–3.94 ppm (peak B and E), 4.23 ppm (peak C), 5.10 ppm (peak F), and 2.72 ppm (peak D), which corresponded to OCH_3, O-$(CH_2)_2$-O of mPEG skeleton and =C-OH of β-CD, CH_2COONH of mPEG, O-CH-O of β-CD, and NH-$(CH_2)_2$-NH, respectively. These results indicated the success of the synthesis of CD-mPEG.

In addition, the successful conjugation of CD with mPEG was evaluated by FTIR analysis (Figure 3). As shown in the FTIR spectrum of PNS (Figure 3(a)), a band at 1615 cm^{-1} was attributed to the OH bending vibration of water molecules on the surface of PNS. The large sharp peak at 1093 cm^{-1} and peak at 813 cm^{-1} were both assigned to the stretching modes of the siloxane framework, which is the asymmetric stretching frequency of Si-O-Si. Additionally, a broad band observed at 3417 cm^{-1} was associated with OH stretching frequency for the silanol group. These adsorption bands

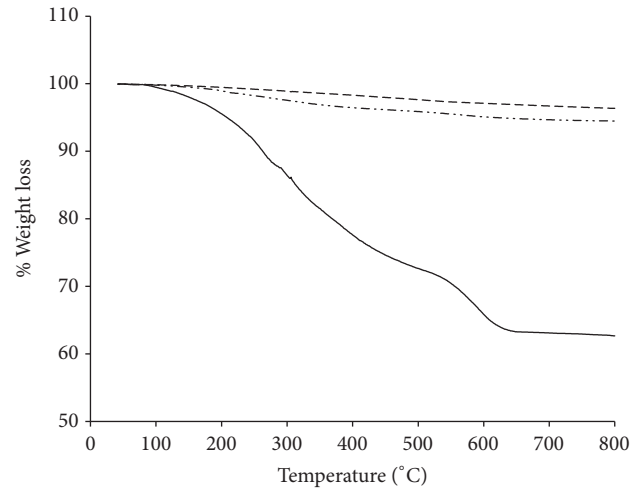

Figure 4: TGA curves: PNS *(dashed curve)*; PNS-SS-ADA *(double dashed dotted curve)*; PNS-SS-ADA@CD-mPEG *(solid curve)*.

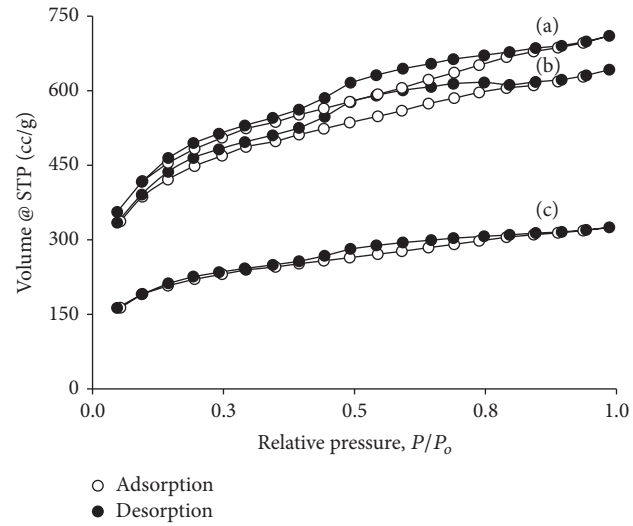

Figure 5: N_2 adsorption-desorption isotherms: PNS (a); PNS-SS-ADA (b); PNS-SS-ADA@CD-mPEG (c).

still exist in the FTIR spectra of PNS-SS-ADA (Figure 3(b)) and PNS-SS-ADA@CD-mPEG (Figure 3(c)). When PNS was immobilized with ADA, the characteristic absorption band at 1698 cm^{-1} was attributed to the adsorption of carboxyl group and two new bands of amantadine, indicating the successful conjugation between ADA and PNS [7]. Figure 3(c) shows the intensity of IR peak appeared at 604 cm^{-1}, which was attributed to –SS- dihedral bending of DTDP. The visible absorption peaks at 1696 cm^{-1} and 1608 cm^{-1} were ascribed to the C=O stretching frequency (amide I) and N-H bending vibration in alkyl chains of mPEG. These results suggested that PNS-SS-ADA@CD-mPEG was prepared [7].

3.2. Particle Properties of PNS-SS-ADA@CD-mPEG. The typical TGA curves of PNS (dotted curve), PNS-SS-ADA (dash-dotted curve), and PNS-SS-ADA@CD-mPEG (solid curve) are shown in Figure 4. The temperature was ramped up 800°C with a heating rate at 10°C/min. As shown in the TGA curve of PNS, only 3.33% weight loss was observed caused by the loss of physisorbed water. There is no statistically significant difference between the weight loss of PNS and PNS-SS-ADA, approximately 2.27%, which may be related to the thermal decomposition of outer layer SS-ADA. By contrast, the total weight loss of PNS-SS-ADA@CD-mPEG was 57.33%, which was much higher than that of PNS (3.33%) and PNS-SS-ADA (5.60%). This increased portion could be attributed to the CD-mPEG conjugate. Furthermore, there remained 42.67% of weight that may be due to the PNS residue, suggesting that the surface of PNS-SS-ADA was immobilized with CD-mPEG.

The N_2 adosrption-desorption isotherms of PNS, PNS-SS-ADA, and PNS-SS-ADA@CD-mPEG are shown in Figure 5. These isotherms exhibit a type IV hysteresis loop with type H_2 hysteresis loops at a relative pressure $P/P_o = 0.4$–0.8, which is caused by capillary condensation of mesoporous adsorption [22]. There were significant differences in pore volume (V_p, cm^3/g) among PNS, PNS-SS-ADA, and PNS-SS-ADA@CD-mPEG, which are 710.40 cm^3/g, 642.20 cm^3/g, and 324.87 cm^3/g, respectively. The reduced V_p of the modified PNS indicated that the mesoporous structure of PNS was affected by surface modification. These results could be explained by the presence of the outer layer on the surface of PNS nanoparticles.

The TEM image and typical particle size histogram fitted by long normal distribution function of PNS and PNS-SS-ADA@CD-mPEG are shown in Figure 6. The morphology of both nanoparticles was spherical in shape, and their particle sizes were also different, 49.6 ± 2.56 nm for PNS and 55.5 ± 3.05 nm for PNS-SS-ADA@CD-mPEG. This difference was attributed to the presence of outer layer SS-ADA@CD-mPEG on the surface of PNS nanoparticles. Previous studies have indicated that nanoparticles less than 20–30 nm are rapidly eliminated by renal excretion, whereas nanoparticles in the range of 30–150 nm can stay in the circulatory system for a longer period of time [23]. One of the most critical insights of PNS is that the bioactive molecules can be significantly loaded into the porous pores of silica nanoparticles. More importantly, the release of DOX from DOX/PNS-SS-ADA@CD-mPEG can be controlled and prolonged due to the presence of SS-ADA@CD-mPEG. These results suggest that the modified PNS-SS-ADA@CD-mPEG nanoparticles have great potential as an efficient and promising candidate for controlling drug release.

3.3. Loading and In Vitro DOX Release. The DOX-loaded formulations were prepared using equilibrium dialysis technique. The DLE and DLC of PNS-SS-ADA@CD-mPEG were found to be 79.2 ± 3.2% and 13.8 ± 2.7%, respectively. These results might be due to the loading of DOX molecules into the PNS-SS-ADA nanoparticles before CD-mPEG conjugation, which prevents the diffusion of DOX to the solution. These findings also demonstrated that PNS-SS-ADA@CD-mPEG nanoparticles have the potential to increase drug encapsulation.

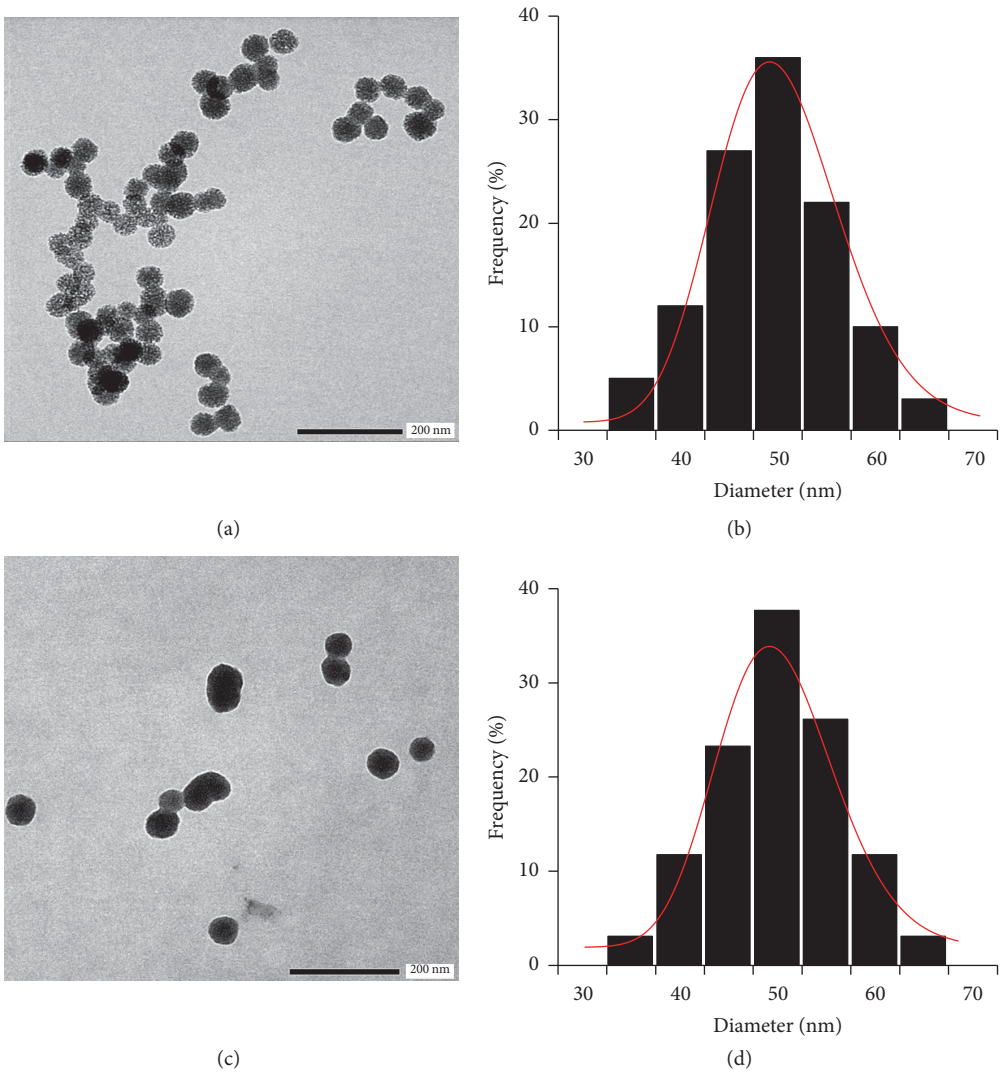

Figure 6: TEM images and particle size histograms: PNS (a, b); PNS-SS-ADA@CD-mPEG (c, d) fitted by log-normal distribution function, respectively.

To further evaluate the redox responsiveness of the modified PNS-SS-ADA@CD-mPEG nanoparticles, *in vitro* release profile of DOX from DOX/PNS-SS-ADA@CD-mPEG nanocarriers was performed under reducing condition of 5 mM DTT. The release rate of the nanocarriers is expected to increase by the addition of DTT-reducing agent used to break down disulfide bonds of DOX/PNS-SS-ADA@CD-mPEG nanoparticles [7, 24, 25]. Figure 7 shows the DOX release behavior of DOX/PNS-SS-ADA@CD-mPEG nanoparticles with and without DTT over a period of 120 h. It can clearly be seen that, in the presence of DTT, the release of DOX from DOX/PNS-SS-ADA@CD-mPEG was significantly faster than that under the physiological condition (pH 7.4). During the first 2 h, the cumulative release amount of DOX was approximately 39.6% as compared with 10.7% in the pH 7.4 PBS buffer. Furthermore, around 89.3% of the total drug amount was released after 120 h for DTT condition; by contrast, 44.3% of DOX was observed within the same time frame in the absence of DTT. The DOX-loaded formulation showed a long-term stable drug release profile up to 120 h in PBS condition (pH 7.4) and a redox-responsive drug release behavior in the presence of DTT. These results indicated the functionalization of disulfide bonds on the surface of PNS, which might undergo swift oxidation and accelerate the DOX release rate in the intracellular region.

3.4. In Vitro Cytotoxicity. The biocompatibility of nanomaterials plays a crucial role in their potential biomedical applications [26, 27]. In this study, the *in vitro* cytotoxicity effect of the prepared PNS-SS-ADA@CD-mPEG, free DOX,and DOX/PNS-SS-ADA@CD-mPEG against HeLa cells was determined. As shown in Figure 8, PNS-SS-ADA@CD-mPEG exhibited cytocompatibility towards the cells with approximately 98% cell viability at 100 μg/mL for 96 h. In contrast, free DOX showed acute toxicity to the cell line; the cell viability dropped to less than 20%

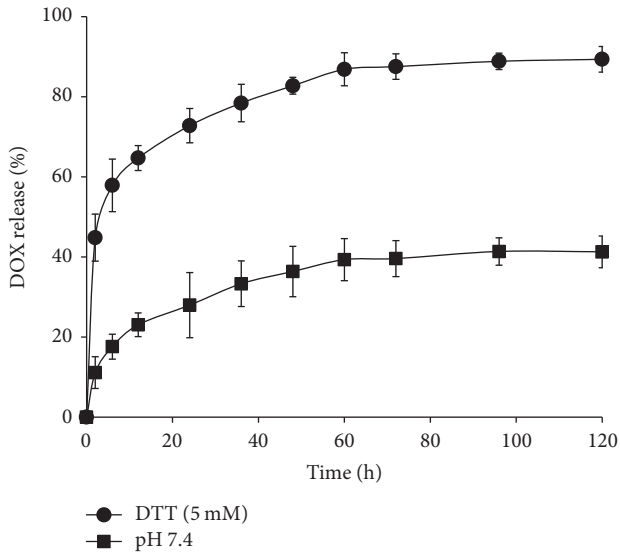

Figure 7: *In vitro* release profiles of DOX from PNS-SS-ADA@CD-mPEG in PBS (pH 7.4) with and without DTT (5 mM).

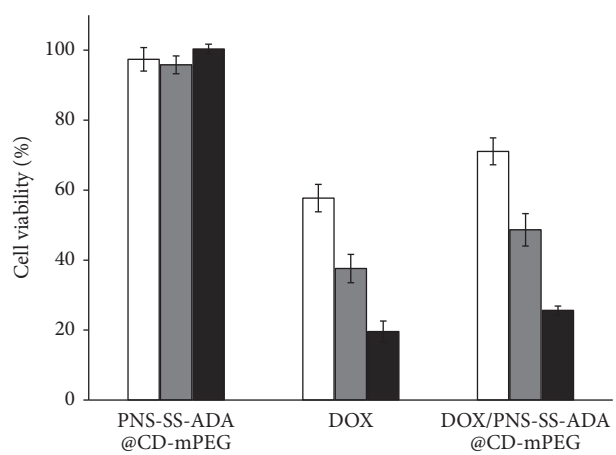

Figure 8: Viability of HeLa cells incubated with PNS-SS-ADA@CD-mPEG (100 μg/mL), free DOX (5 μg/mL), and DOX/PNS-SS-ADA@CD-mPEG (eq. DOX conc.) for 24, 48, and 96 h. The cells were exposed to the samples for the indicated times. The data represent the mean values ± the standard deviation (SD) ($n = 4$).

after 96 h. The DOX/PNS-SS-ADA@CD-mPEG showed the improvement in the cytocompatibility compared with DOX alone, at 70% cell viability for 24 h. The lower cytotoxicity of DOX/PNS-SS-ADA@CD-mPEG nanoparticles can be attributed to their extended drug release characteristic. These results confirmed the promising application of PNS-SS-ADA@CD-mPEG nanocarriers with low systemic toxicity for controlled drug delivery.

4. Conclusion

In this report, PNS-SS-ADA@CD-mPEG nanoparticles have been successfully prepared via the conjugation between PNS-SS-ADA and CD-mPEG. The formed PNS-SS-ADA@CD-mPEG existed in a spherical shape with an average diameter of 55.5 ± 3.05 nm and acted as potential nanocarriers for effectively loading and controlled release of DOX. The prepared PNS-SS-ADA@CD-mPEG nanocarriers showed a high cell viability against HeLa cancer cells. DOX was significantly encapsulated into the formed PNS-SS-ADA@CD-mPEG nanoparticles, at 79.2 ± 3.2%. Moreover, the release of DOX from DOX/PNS-SS-ADA@CD-mPEG nanocarriers was controlled and delayed up to 120 h in PBS buffer (pH 7.4), compared with less than 40 h in buffer with 5 mM DTT. The developed PNS-SS-ADA@CD-mPEG nanoparticle could be a potential candidate for controlling the release of anticancer drugs with high drug loading efficiency and less systemic cytotoxicity.

Conflicts of Interest

The authors declare that there are no conflicts of interest regarding the publication of this paper.

Acknowledgments

This research was funded by Vietnam National Foundation for Science and Technology Development (NAFOSTED) (under Grant no. 104.02-2014.83).

References

[1] M. Xie, H. Shi, Z. Li et al., "A multifunctional mesoporous silica nanocomposite for targeted delivery, controlled release of doxorubicin and bioimaging," *Colloids and Surfaces B: Biointerfaces*, vol. 110, pp. 138–147, 2013.

[2] Y. Zhang, H. F. Chan, and K. W. Leong, "Advanced materials and processing for drug delivery: the past and the future," *Advanced Drug Delivery Reviews*, vol. 65, no. 1, pp. 104–120, 2013.

[3] W. Cha, R. Fan, Y. Miao et al., "Mesoporous silica nanoparticles as carriers for intracellular delivery of nucleic acids and subsequent therapeutic applications," *Molecules*, vol. 22, no. 5, article no. 782, 2017.

[4] T. V. Tran, U. V. Vo, D. Y. Pham et al., "Supramolecular chemistry at interfaces: Host-guest interactions for attaching PEG and 5-fluorouracil to the surface of porous nanosilica," *Green Processing & Synthesis (GPS)*, vol. 5, no. 6, pp. 521–528, 2016.

[5] J. Zhang, M. Niemelä, J. Westermarck, and J. M. Rosenholm, "Mesoporous silica nanoparticles with redox-responsive surface linkers for charge-reversible loading and release of short oligonucleotides," *Dalton Transactions*, vol. 43, no. 10, pp. 4115–4126, 2014.

[6] A. Malfanti, I. Miletto, E. Bottinelli et al., "Delivery of gemcitabine prodrugs employing mesoporous silica nanoparticles," *Molecules*, vol. 21, no. 4, article no. 522, 2016.

[7] T. T. Nguyen Thi, T. V. Tran, N. Q. Tran, C. K. Nguyen, and D. H. Nguyen, "Hierarchical self-assembly of heparin-PEG end-capped porous silica as a redox sensitive nanocarrier for doxorubicin delivery," *Materials Science and Engineering C: Materials for Biological Applications*, vol. 70, part 2, pp. 947–954, 2017.

[8] I. I. Slowing, J. L. Vivero-Escoto, C. W. Wu, and V. S. Y. Lin, "Mesoporous silica nanoparticles as controlled release drug delivery and gene transfection carriers," *Advanced Drug Delivery Reviews*, vol. 60, no. 11, pp. 1278–1288, 2008.

[9] D. H. Nguyen, J. H. Choi, Y. K. Joung, and K. D. Park, "Disulfide-crosslinked heparin-pluronic nanogels as a redox-sensitive nanocarrier for intracellular protein delivery," *Journal of Bioactive and Compatible Polymers*, vol. 26, no. 3, pp. 287–300, 2011.

[10] C. Ding, L. Tong, J. Feng, and J. Fu, "Recent advances in stimuli-responsive release function drug delivery systems for tumor treatment," *Molecules*, vol. 21, no. 12, article no. 1715, 2016.

[11] J. Wen, S. M. Anderson, J. Du et al., "Controlled protein delivery based on enzyme-responsive nanocapsules," *Advanced Materials*, vol. 23, no. 39, pp. 4549–4553, 2011.

[12] Y.-K. Huang, C.-H. Su, J.-J. Chen et al., "Fabrication of Silica-Coated Hollow Carbon Nanospheres Encapsulating Fe3O4 Cluster for Magnetical and MR Imaging Guided NIR Light Triggering Hyperthermia and Ultrasound Imaging," *ACS Applied Materials & Interfaces*, vol. 8, no. 23, pp. 14470–14480, 2016.

[13] J. W. Bae, D. H. Go, K. D. Park, and S. J. Lee, "Thermosensitive chitosan as an injectable carrier for local drug delivery," *Macromolecular Research*, vol. 14, no. 4, pp. 461–465, 2006.

[14] C. Park, K. Oh, S. C. Lee, and C. Kim, "Controlled release of guest molecules from mesoporous silica particles based on a pH-responsive polypseudorotaxane motif," *Angewandte Chemie International Edition*, vol. 46, no. 9, pp. 1455–1457, 2007.

[15] M. Zhao, A. Biswas, B. Hu et al., "Redox-responsive nanocapsules for intracellular protein delivery," *Biomaterials*, vol. 32, no. 22, pp. 5223–5230, 2011.

[16] H. Li, J. Z. Zhang, Q. Tang, M. Du, J. Hu, and D. Yang, "Reduction-responsive drug delivery based on mesoporous silica nanoparticle core with crosslinked poly(acrylic acid) shell," *Materials Science and Engineering C: Materials for Biological Applications*, vol. 33, no. 6, pp. 3426–3431, 2013.

[17] Y. Wang, N. Han, Q. Zhao et al., "Redox-responsive mesoporous silica as carriers for controlled drug delivery: A comparative study based on silica and PEG gatekeepers," *European Journal of Pharmaceutical Sciences*, vol. 72, article no. 3191, pp. 12–20, 2015.

[18] T. V. Tran, T. H. Phuong, N. Q. Tran, C. K. Nguyen, and D. H. Nguyen, "Polymeric chitosan based nanogels as a potential platform for dual targeted drug delivery in cancer therapy," *International Journal of Nanotechnology*, vol. 15, no. 1/2/3, p. 188, 2018.

[19] Y. Wang, Y. Cui, J. Huang et al., "Redox and pH dual-responsive mesoporous silica nanoparticles for site-specific drug delivery," *Applied Surface Science*, vol. 356, pp. 1282–1288, 2015.

[20] T. L. Nguyen, T. H. Nguyen, and D. H. Nguyen, "Development and in Vitro Evaluation of Liposomes Using Soy Lecithin to Encapsulate Paclitaxel," *International Journal of Biomaterials*, vol. 2017, Article ID 8234712, 7 pages, 2017.

[21] N. I. Vazquez, Z. Gonzalez, B. Ferrari, and Y. Castro, "Synthesis of mesoporous silica nanoparticles by sol-gel as nanocontainer for future drug delivery applications," *Boletín de la Sociedad Española de Cerámica y Vidrio*, vol. 56, no. 3, pp. 139–145, 2017.

[22] T. Qian, J. Li, and Y. Deng, "Pore structure modified diatomite-supported PEG composites for thermal energy storage," *Scientific Reports*, vol. 6, Article ID 32392, 2016.

[23] V. M. Thanh, T. H. Nguyen, T. V. Tran et al., "Low systemic toxicity nanocarriers fabricated from heparin-mPEG and PAMAM dendrimers for controlled drug release," *Materials Science and Engineering C: Materials for Biological Applications*, vol. 82, pp. 291–298, 2018.

[24] D. H. Nguyen, Y. K. Joung, J. H. Choi, H. T. Moon, and K. D. Park, "Targeting ligand-functionalized and redox-sensitive heparin-Pluronic nanogels for intracellular protein delivery," *Biomedical Materials*, vol. 6, no. 5, Article ID 055004, 2011.

[25] D. Chang, J. Lei, H. Cui et al., "Disulfide cross-linked nanospheres from sodium alginate derivative for inflammatory bowel disease: Preparation, characterization, and in vitro drug release behavior," *Carbohydrate Polymers*, vol. 88, no. 2, pp. 663–669, 2012.

[26] A. Rashti, H. Yahyaei, S. Firoozi et al., "Development of novel biocompatible hybrid nanocomposites based on polyurethane-silica prepared by sol gel process," *Materials Science and Engineering C: Materials for Biological Applications*, vol. 69, pp. 1248–1255, 2016.

[27] D. Q. Hoang, T. V. Tran, N. Q. Tran et al., "Functionalization of Fe_3O_4 nanoparticles with biodegradable chitosan-grafted-mPEG for paclitaxel delivery," *Green Processing & Synthesis (GPS)*, vol. 5, no. 5, pp. 459–466, 2016.

Hindawi
International Journal of Biomaterials
Volume 2018, Article ID 8040893, 6 pages
https://doi.org/10.1155/2018/8040893

Review Article

Scaffolds for Pelvic Floor Prolapse: Logical Pathways

Julio Bissoli and Homero Bruschini

Hospital das Clínicas da Faculdade de Medicina da Universidade de São Paulo (HCFMUSP), 05410-020 São Paulo, SP, Brazil

Correspondence should be addressed to Julio Bissoli; julio_bissoli@yahoo.com.br

Received 15 May 2017; Accepted 17 August 2017; Published 1 February 2018

Academic Editor: Qiang Wei

Copyright © 2018 Julio Bissoli and Homero Bruschini. This is an open access article distributed under the Creative Commons Attribution License, which permits unrestricted use, distribution, and reproduction in any medium, provided the original work is properly cited.

Pelvic organ prolapse (POP) has borrowed principles of treatment from hernia repair and in the last two decades we saw reinforcement materials to treat POP with good outcomes in terms of anatomy but with alarming complication rates. Polypropylene meshes to specifically treat POP have been withdrawn from market by manufactures and a blank space was left to be filled with new materials. Macroporous monofilament meshes are ideal candidates and electrospinning emerged as a reliable method capable of delivering production reproducibility and customization. In this review, we point out some pathways that seem logical to be followed but have been only researched in last couple of years.

1. Introduction

Greeks created the term "prosthesis" or "to place before." Hernia repair usually consists of placing meshes to assist the suture control of protrusions [1]. In modern history, Theodore Billroth in 1857 inspired all prosthesis designers with his proposition "If we could artificially produce tissue of the density and toughness of fascia and tendon, the secret of the radical cure of the hernia repair would be discovered" [2], but its concept of repair dates back to Greeks who first described silver strands woven sutured with gold wire to act as a prosthesis [3].

Plastic development revolutionized hernia repair firstly with nylon woven prosthesis, abandoned due to loss of strength caused by hydrolysis, followed by other materials as polypropylene (PP), polytetrafluorethylene (PTFE), Dacron, and polyethylene (PE) [4].

In anatomical terms, hernias are quite similar to pelvic organ prolapse where one or more vaginal compartments descend downwards vaginal opening causing vaginal bulging [5] and this similarity brought the same treatment concepts from one to another [6–8]. What was ignored was the thin layer of mucosae capable of covering an occasional prosthesis, the elasticity inherent to the organ (specially during sexual activity), and exuberant vaginal local florae [5, 7].

2. Pelvic Organ Prolapse

In recent years, development of a new kind of mesh specifically designed for vaginal surgery earned some interest because of a major withdraw from mesh market by leading industries after FDA safety warnings on complications of polypropylene in prolapse surgery and due to massive losses on court due to litigation [8–10].

POP is a high prevalent disease occurring in up to 37% of asymptomatic women [11], with lifetime risk of intervention up to 80 years estimated to be 11 to 20% [12, 13] and reoperation rates due to symptoms around 30% [14].

With such high prevalence and failure rates with conventional treatments up to 56% [15], it was a natural movement for doctors and researchers to start developing reinforcements to sutures performed during vaginal compartments treatment.

3. Reinforcements Subtypes

The materials used to reinforce POP treatment can be autologous, heterologous, synthetic absorbable, or inabsorbable [7]. The initial tests with fascia lata, acellular dermis, and rectus sheet did not show superior results to conventional techniques, with 38% failure [16], and are limited by donor

site, pain, surgery time increase, and quality/quantity variable [17, 18] with the clear advantage to not trigger any immune response. Heterologous grafts keep the same or inferior results potentially acting as a carrier to viral and prion diseases [7, 8].

Among synthetic reinforcement, the polyglactin is shown to be absorbed without matrix remodelling and failure before 2 years of implant [19–21] while inabsorbable polypropylene (most widely used) showed 80% success compared to traditional techniques in short time [22] but with midterm complications such erosions/extrusions around 25% [23] causing FDA to release safety warnings in 2008 and 2011 [9, 10] triggering ethical legal problems and prompting leading companies to withdraw from market [8].

Considering limited results with classical approaches and materials, especially after withdrawing of synthetic meshes manufacturers, a blank space emerged to be filled with new materials.

4. Synthetic Meshes Classification

Meshes are a subtype of synthetic matrices with organized woven or knitted pattern. Amid in 1997 classified meshes accordingly to its porosity and filaments structure [25], predicting complications as bigger pores allow higher vascularization, fibroblasts ingrowth, and immune cells infiltration increasing biocompatibility and infection resilience [26]. On the other way, multifilament fibres (with space between filaments inferior to 10 microns) and microporous meshes are less susceptible to cellular ingrowth and macrophage/lymphocyte action (they measure around 9–20 microns) being prone to bacterial colonization.

Theoretically, an ideal material would be a macroporous monofilament type I mesh of Amid [27–29] and practical applications confirm such statement with types II, III, and IV being used for POP and SUI with short-term complication rates around 20–30% [22, 27, 30].

5. Synthetic Matrices Production

There are several methods for higher porosity matrices production, like self-assembly [31], phase separation, solvent casting and particulate leaching, freeze drying, melt moulding, gas foaming, and solid free-forming [32]. All of them with reproducibility limitations and poor control of characteristics such diameter of fibres and pore size, pore geometry, and fibre orientation with electrospinning as an alternative to surpass all these difficulties [33].

6. Electrospinning

Electrospinning is a physical phenomenon observed when a high viscosity polymer solution is exposed to an intense electric field in a recipient where the liquid is extruded in a slow fashion through one small or multiple small orifices (i.e., spinneret). Usually such solution is made by a high molecular weight polymer in a solvent with high vapour pressure (i.e., capable of easily evaporate in a room temperature) and low conductivity with high dielectric constant (i.e., high resistance to stress before brake and allow passage of electric current) [34].

Besides relatively high viscosity of material used, under high electric field produced by a high tension power source, a superficial tension rupture at the tip of the spinneret occurs (usually a blunt tip needle). This rupture creates an instability region causing stretching of viscous solution towards an earthed collector, parallel to the lines of force of electric field, producing micro/nanometric scale fibres in diameter. Such fibres become dried after evaporation of solvent during its pathway to the collector.

This process is known since the beginning of the last century being observed by Rayleigh in 1897, detailed by Zeleny in 1914, and patented by Formhals in 1934 for textile production. Taylor, in his studies about electrostatics (1969), described the jets produced by the technique (today called by his name, Taylor's cone), but electrospinning as a biomedical application emerged only after the 1990s because of its price and reproducibility, being one of the commonest methods of matrix production in bioengineering.

Parameters controlled during electrospinning process are classically divided into solution properties, controlled variables, and environmental parameters [32]. The solution properties included viscosity, superficial tension, conductivity, and molecular weight, while controlled variables are flow rate, electric field intensity, collector distance to the end of the tip of spinneret, size of the tip, and geometry of collector. Environmental parameters are temperature, pressure, and air speed [34].

From all described variables, the most important is the solution concentration to determine, among other things, the diameter of fibres.

7. Polymers

Polymers are big molecules produced by repetition of numerous subunits called monomers and depending on the number of types of repetitive units can be further classified as homopolymers or copolymers. Its name derives from Greek *polus* (i.e., lots of) and *merossu* (i.e., parts), and its physical characteristics are dependent on the size and length of their chain. Usually as polymer chain increases, its degradation time is prolonged, and its viscosity, strength, and rigidity are higher, being common to allude to it in terms of molecular weight (minimum, maximum, and average value) [35].

They can be further subclassified as naturals or synthetics and absorbable or inabsorbable. For bioengineering applications, there are necessary characteristics: their nontoxicity (direct or indirect), nonimmunogenicity, noncarcinogenicity, and biocompatibility (ability to integrate with living tissues). Desirable characteristics are resilience to infection, low cost, ability to be easily manufactured and stored, and absorption/degradation in a fashion that allows repopulation and integration by living cells from target tissue and mechanical properties compatible with target tissue function from day 0, during repopulation until its complete reabsorption (Figure 1) [24].

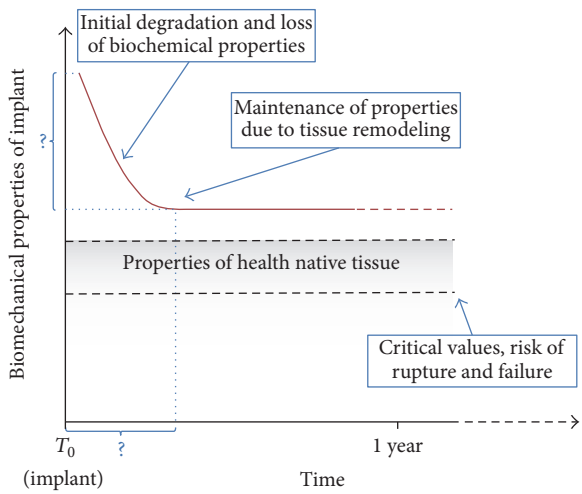

Figure 1: Ideal biomechanical properties of biodegradable scaffolds (adapted from Osman et al. [24]).

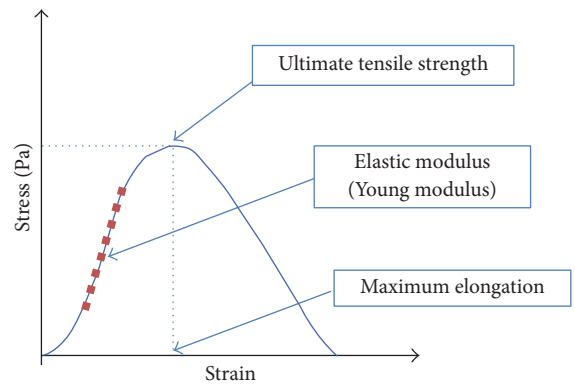

Figure 2: Stress-strain example curve with elastic modulus, ultimate tensile strength, and maximum elongation.

For each target tissue the desirable properties are different. For each polymer used in an implant, a drop in its mechanical properties will occur proportionally to its reabsorption and thus depends on its degradation speed and its micro/nanostructure. Ideally, such characteristics to be mimic should be known previously (ultimate tensile strength, elasticity, and absorption time) and adjusted accordingly to each new microenvironment.

Among the most common polymers electrospun are polylactic acid (PLA), polyglycolic acid (PGA), polyhydroxybutyrate covalerate (PHBV), polycaprolactone (PCL), chitosan, collagen, and polyurethanes (PU).

Aliphatic polyesters like polycaprolactone and polyglycolic acid are materials extensively known since 1960 because of its biocompatibility. They are hydrolysed and/or enzymatically digested to nontoxic subproducts. They usually have high elastic modulus and tensile strength with poor elongation (considered rigid polymers), great candidates for tissue engineering [30].

Polyhydroxyalkanoates as poly(3-hydroxybutyrate-co-3-hydroxyvalerate) (PHBV) are recently investigated in tissue engineering because of its resilience to infection and hydrolysis much like polyurethanes (PU) that additionally have calcification resistance and are known in applications as synthetic rubber for more than 30 years. Both present longer absorption times when compared to polyesters being PU known by its great ability to cope with strain.

8. Biomechanical Tests

There are no standard protocols for biomechanical testing of vaginal tissues, being the best methodologies derived from uniaxial tests (i.e., test performed only in one direction), measured in a tensiometer stress-strain curves. Multiaxial tests or biaxial tests potentially would reflect a model closer to its real mechanical properties, but they are more complex and demand specific software and special equipment making its standardization even more complex than uniaxial tests.

Briefly, the uniaxial biomechanical test consists of firmly securing sample between two clamps connected to a tensiometer and a computer and distending the sample in a controlled fashion. Previous known distance of clamps, sample width and thickness, and constant uniaxial distention of clamps (i.e., keeping the same orientation and speed of force) until sample failure or test manually stops will provide data to calculate its biomechanical characteristics.

The ultimate tensile strength is calculated dividing the load applied to the sample (in Newtons, N) by the cross section area of the sample being reported in N/m2 (Pascals). Strain is calculated dividing elongation of the sample (in meters, m) by its initial length between clamps (in meters, m) resulting in a quotient without units or a percentage. Commonly, such data is plotted on a graph and shows a linear portion where tension is direct proportional to strain (respecting Hooke's Law) where strain is reversible or elastic and then a plateau where elongation is irreversible or plastic followed by an inflection (ultimate tensile strength) with correspondence to X-axis defining maximum strain.

The example can be observed at Figure 2, the elastic modulus or Young modulus can be calculated from inclination of linear portion of the stress-strain curve and it is inversely proportional to elasticity of the sample.

To develop an ideal material for a target tissue, knowledge of its properties is crucial and a few studies showed biomechanical properties for human tissues. The vast majority do not normalize its data using cross section area exhibiting values only in Newtons, preventing posterior comparisons [7, 36, 37].

9. Paravaginal Mechanical Properties

Choe et al. compared 2 × 5 cm strips of fascia lata, dermis, rectum sheet, and vaginal mucosae (measure commonly used at sling surgeries [38]) in women operated for various reasons [39] showing that fascia lata had the biggest tensile strength (217 N), followed by human dermis (122 N) and rectum sheet and vaginal mucosae (both with 42 N).

Lei et al. analysed 43 women after hysterectomy and categorized them in groups, premenopause and postmenopause

Table 1: Elastic modulus, maximum elongation, and ultimate tensile strength in women with and without prolapse (adapted from Lei et al.).

	Control premenopause	Prolapse premenopause	Control postmenopause	Prolapse postmenopause
Elastic modulus (MPa; mean ± EPM)	6.65 ± 1.48	9.45 ± 0.70	10.26 ± 1.10	12.10 ± 1.10
Maximum elongation (mean ± EPM)	1.68 ± 0.11	1.50 ± 0.02	1.37 ± 0.04	1.14 ± 0.06
Ultimate tensile strength (MPa; mean ± EPM)	0.79 ± 0.05	0.60 ± 0.02	0.42 ± 0.03	0.27 ± 0.03

and with or without prolapse (Table 1), testing with uniaxial tests tissues with 5 mm × 25 mm and plotting their stress-strain curves establishing native values considered maximum (premenopause) and minimum (postmenopause) obtaining maximum elongation and elastic modulus references for most publications in this field by being comparable to other samples (i.e., normalized by cross section area) [40]. As a critic to such conclusions it is important to notice that samples tested were from vaginal mucosae closer to apex and not from suspensory ligaments or mucosae closer to cystocele/rectocele common defects.

10. Discussion

We do not know exactly how much is the demand in Newtons for the pelvic floor, but we estimate forces acting on it to be around 2,2 to 13,4 N/cm from stand still to stand with Valsalva [41]. Meanwhile, we know that the best autologous candidate—rectum fascia—could cope up to 16 N/cm with a 25% vertical strain [42].

It is important to highlight that tensile strength alone is not capable of predicting success in reconstructive urogenital surgery, and fascia lata and acellular dermis (both quite strong) also have high relapse rate before 2 years of surgery [19, 43] showing that, for biocompatible absorbable materials, remodelling in the host is probably of higher importance than the initial tensile strength of the implant [44].

We still do not have a substitute for paravaginal weakened tissues with native characteristics in terms of resistance and flexibility and data have shown that we are not close to find it [9, 10, 23, 45], notably a potential replacement for polypropylene meshes used in POP and SUI surgery, efficient by anatomical point of view but with complications in POP case that precludes its use.

Such complications have multiple factors involved, but polypropylene high resistance, inflexibility, and inelasticity certainly play a role heightened by a contraction tendency after the implant, despite being considered biocompatible [8].

Several good candidates had been prospected to replace it, each scaffold with or without specific cell type being regarded as ideal. Oral fibroblasts [46], adipose derived stem cells [47], vaginal fibroblasts [48], and muscle cells [49] all have its qualities and defects being more similar or not to targeted paravaginal tissue, being more easily or not to harvest and/or to cultivate onto scaffolds produced with variations of PLA, PLGA, PU, and processed small intestine submucosae.

Considering costs, regulations, and facilities needed to widespread cell culture to clinical practice, probably the first material produced to replace polypropylene meshes in POP practice will be an off-the-shelf synthetic scaffold with great cell affinity targeted to a specific biomechanical demand of paravaginal tissue.

Animal experiments of at least 6–12 months in a model physiologically relevant to POP will help to establish how degradation and neotissue formation will affect properties of such material.

11. Conclusion

We have been done a lot to replace polypropylene meshes by matrices not only capable of withstanding tension but also capable of interacting with cells and promote tissue remodelling with fibroblasts ingrowth, extracellular matrix production, and angiogenesis [50] and we already made some progress in this regard with POP.

Respecting Billroth's principle and producing materials strong enough but sufficiently elastic to allow natural distention of vaginal tissue [44] and biocompatible to reflect paravaginal properties [51] are the right pathway and surprisingly only recently started to be followed.

Additional Points

Highlights. (i) Pelvic organ prolapse treatment borrowed anatomical concepts from hernia repair without considering local differences in terms of elasticity, florae, and sexual activity. Major brand meshes for POP have been withdrawn from market due to complications and litigious problems. (ii) Despite the logic to know that the material is to be replaced or reinforced and then use this data to develop a new prosthesis, pelvic prolapse lacks in terms of basic research of biomechanical properties and lacked in safety studies before applying polypropylene meshes for this purpose. (iii) To promote true remodelling and cure we not only should think about reinforcement and biomechanical properties but also must develop a material that interacts with cells and promote fibroblast ingrowth and extracellular matrix production. Lack of these combined qualities invariably will lead to failure.

Conflicts of Interest

The authors declare that there are no conflicts of interest regarding the publication of this manuscript.

Acknowledgments

Thanks are due to Professor Chris Chapple for mentoring during fellowship in Sheffield and whose support was of paramount importance and thanks are due to Professor Miguel Srougi for encouragement and vision during all steps of this work. This work was supported by Conselho Nacional de Pesquisa Tecnologia-Programa Ciência sem Fronteiras.

References

[1] P. L. Carter, N. Lloyd, and S. Rene, "Preperitoneal inguinal pioneers," *American Journal of Surgery*, vol. 211, no. 5, pp. 836–838, 2016.

[2] J. E. Skandalakis, G. L. Colborn, L. J. Skandalakis, D. A. McClusky, R. J. Fitzgibbons, and A. G. Greenburg, "Historic aspects of groin hernia repair," *Nyhus Condons Hernia*, 2002.

[3] Y. Bilsel and I. Abci, "The search for ideal hernia repair; mesh materials and types," *International Journal of Surgery*, vol. 10, no. 6, pp. 317–321, 2012.

[4] M. Kapischke and A. Pries, "Theodor Billroth's vision and Karl Ziegler's action: Commemoration of the 40th day of death and the 50th anniversary of conferment of Nobel Prize for Chemistry of Karl Ziegler," *Surgery (United States)*, vol. 155, no. 2, pp. 347–349, 2014.

[5] J. E. Jelovsek, C. Maher, and M. D. Barber, "Pelvic organ prolapse," *The Lancet*, vol. 369, no. 9566, pp. 1027–1038, 2007.

[6] U. Ulmsten, L. Henriksson, P. Johnson, and G. Varhos, "An ambulatory surgical procedure under local anesthesia for treatment of female urinary incontinence," *International Urogynecology Journal and Pelvic Floor Dysfunction*, vol. 7, no. 2, pp. 81–86, 1996.

[7] P. Dällenbach, "To mesh or not to mesh: A review of pelvic organ reconstructive surgery," *International Journal of Women's Health*, vol. 7, pp. 331–343, 2015.

[8] G. Gigliobianco, S. R. Regueros, N. I. Osman et al., "Biomaterials for pelvic floor reconstructive surgery: How can we do better?" *BioMed Research International*, vol. 2015, Article ID 968087, 20 pages, 2015.

[9] D. G. Schultz, *FDA Public Health Notification: Serious Complications Associated with Transvaginal Placement of Surgical Mesh in Repair of Pelvic Organ Prolapse and Stress Urinary Incontinence*, Food Drug Adm, Silver Spring, Md, USA, 2008.

[10] Administration UF and D, Administration UF and D. FDA safety communication: update on serious complications associated with transvaginal placement of surgical mesh for pelvic organ prolapse. July. 2011;13:2011.

[11] S. Swift, P. Woodman, A. O'Boyle et al., "Pelvic Organ Support Study (POSST): the distribution, clinical definition, and epidemiologic condition of pelvic organ support defects," *American Journal of Obstetrics & Gynecology*, vol. 192, no. 3, pp. 795–806, 2005.

[12] J. M. Wu, C. A. Matthews, M. M. Conover, V. Pate, and M. Jonsson Funk, "Lifetime risk of stress urinary incontinence or pelvic organ prolapse surgery," *Obstetrics and Gynecology*, vol. 123, no. 6, pp. 1201–1206, 2014.

[13] M. F. Fialkow, K. M. Newton, G. M. Lentz, and N. S. Weiss, "Lifetime risk of surgical management for pelvic organ prolapse or urinary incontinence," *International Urogynecology Journal*, vol. 19, no. 3, pp. 437–440, 2008.

[14] A. L. Olsen, V. J. Smith, J. O. Bergstrom, J. C. Colling, and A. L. Clark, "Epidemiology of surgically managed pelvic organ prolapse and urinary incontinence," *Obstetrics and Gynecology*, vol. 89, no. 4, pp. 501–506, 1997.

[15] A. L. Clark, T. Gregory, V. J. Smith, and R. Edwards, "Epidemiologic evaluation of reoperation for surgically treated pelvic organ prolapse and urinary incontinence," *American Journal of Obstetrics and Gynecology*, vol. 189, no. 5, pp. 1261–1267, 2003.

[16] C. Maher, B. Feiner, K. Baessler, C. Christmann-Schmid, N. Haya, and J. Marjoribanks, *Transvaginal mesh or grafts compared with native tissue repair for vaginal prolapse. Transvaginal Mesh Grafts Comp Native Tissue Repair Vaginal Prolapse*, 2016, http://dx.doi.org/10.1002/14651858.CD012079.

[17] M. E. Albo, H. E. Richter, L. Brubaker, P. Norton, S. R. Kraus, P. E. Zimmern et al., "Burch colposuspension versus fascial sling to reduce urinary stress incontinence," *The New England Journal of Medicine*, vol. 356, no. 21, pp. 2143–2155, 2007.

[18] A. J. Walter, J. G. Hentz, J. F. Magrina, and J. L. Cornella, "Harvesting autologous fascia lata for pelvic reconstructive surgery: Techniques and morbidity," *American Journal of Obstetrics and Gynecology*, vol. 185, no. 6, pp. 1354–1359, 2001.

[19] M. P. FitzGerald, J. Mollenhauer, P. Bitterman, and L. Brubaker, "Functional failure of fascia lata allografts," *American Journal of Obstetrics and Gynecology*, vol. 181, no. 6, pp. 1339–1346, 1999.

[20] M. H. Safir, A. E. Gousse, E. S. Rovner, D. A. Ginsberg, and S. Raz, "4-Defect repair of grade 4 cystocele," *Journal of Urology*, vol. 161, no. 2, pp. 587–594, 1999.

[21] A. M. Weber, M. D. Walters, M. R. Piedmonte, and L. A. Ballard, "Anterior colporrhaphy: A randomized trial of three surgical techniques," *American Journal of Obstetrics and Gynecology*, vol. 185, no. 6, pp. 1299–1306, 2001.

[22] T. M. Julian, "The efficacy of Marlex mesh in the repair of severe, recurrent vaginal prolapse of the anterior midvaginal wall," *American Journal of Obstetrics & Gynecology*, vol. 175, no. 6, pp. 1472–1475, 1996.

[23] J. Mahon, D. Varley, and J. Glanville, *Summaries of the safety/adverse effects of vaginal tapes/slings/meshes for stress urinary incontinence and prolapse*, Med Healthc Prod Regul Agency, 2012.

[24] N. Osman, S. Roman, J. Bissoli, F. Sefat, S. MacNeil, and C. Chapple, "Designing a novel tissue inductive bio-absorbable implant for pelvic floor repair: An assessment of tensile and surgical handling properties versus polypropylene mesh and porcine small intestine submucosa," *Neurourol Urodyn*, vol. 32, no. 6, pp. 507–932, 2013.

[25] P. K. Amid, "Classification of biomaterials and their related complications in abdominal wall hernia surgery," *Hernia*, vol. 1, no. 1, pp. 15–21, 1997.

[26] M. Cervigni and F. Natale, "The use of synthetics in the treatment of pelvic organ prolapse," *Current Opinion in Urology*, vol. 11, no. 4, pp. 429–435, 2001.

[27] J. C. Winters, M. P. Fitzgerald, and M. D. Barber, "The use of synthetic mesh in female pelvic reconstructive surgery," *BJU International*, vol. 98, no. 1, pp. 70–77, 2006.

[28] C. Birch and M. M. Fynes, "The role of synthetic and biological prostheses in reconstructive pelvic floor surgery," *Current Opinion in Obstetrics & Gynecology*, vol. 14, no. 5, pp. 527–535, 2002.

[29] M. Slack, J. S. Sandhu, D. R. Staskin, and R. C. Grant, "In vivo comparison of suburethral sling materials," *International Urogynecology Journal and Pelvic Floor Dysfunction*, vol. 17, no. 2, pp. 106–110, 2006.

[30] P. Debodinance, M. Cosson, and G. Burlet, "Tolerance of synthetic tissues in touch with vaginal scars: Review to the point of 287 cases," *European Journal of Obstetrics Gynecology and Reproductive Biology*, vol. 87, no. 1, pp. 23–30, 1999.

[31] Y. Hong, R. L. Legge, S. Zhang, and P. Chen, "Effect of amino acid sequence and pH on nanofiber formation of self-assembling peptides EAK16-II and EAK16-IV," *Biomacromolecules*, vol. 4, no. 5, pp. 1433–1442, 2003.

[32] R. Murugan and S. Ramakrishna, "Nano-featured scaffolds for tissue engineering: A review of spinning methodologies," *Tissue Engineering*, vol. 12, no. 3, pp. 435–447, 2006.

[33] S. Roman, N. Mangir, J. Bissoli, C. R. Chapple, and S. MacNeil, "Biodegradable scaffolds designed to mimic fascia-like properties for the treatment of pelvic organ prolapse and stress urinary incontinence," *Journal of Biomaterials Applications*, vol. 30, no. 10, pp. 1578–1588, 2015.

[34] N. Bhardwaj and S. C. Kundu, "Electrospinning: a fascinating fiber fabrication technique," *Biotechnology Advances*, vol. 28, no. 3, pp. 325–347, 2010.

[35] D. W. Van Krevelen and K. Te Nijenhuis, *Chapter 1 - Polymer Properties. In: Properties of Polymers*, Elsevier, Amsterdam, Netherlands, 4th edition, 2009.

[36] Q. P. Pham, U. Sharma, and A. G. Mikos, "Electrospinning of polymeric nanofibers for tissue engineering applications: a review," *Tissue Engineering*, vol. 12, no. 5, pp. 1197–1211, 2006.

[37] S. Ramakrishna, "An iNtroduction to Electrospinning and Nanofibers," in *World Scientific*, 2005.

[38] M. M. Karram and N. N. Bhatia, "Patch procedure: Modified transvaginal fascia lata sling for recurrent or severe stress urinary incontinence," *Obstetrics and Gynecology*, vol. 75, no. 3, pp. 461–463, 1990.

[39] J. M. Choe, R. Kothandapani, L. James, and D. Bowling, "Autologous, cadaveric, and synthetic materials used in sling surgery: comparative biomechanical analysis," *Urology*, vol. 58, no. 3, pp. 482–486, 2001.

[40] L. Lei, Y. Song, and R. Chen, "Biomechanical properties of prolapsed vaginal tissue in pre- and postmenopausal women," *International Urogynecology Journal*, vol. 18, no. 6, pp. 603–607, 2007.

[41] J. A. Ashton-Miller and J. O. L. DeLancey, "On the biomechanics of vaginal birth and common sequelae," *Annual Review of Biomedical Engineering*, vol. 11, no. 1, pp. 163–176, 2009.

[42] K. Junge, U. Klinge, A. Prescher, P. Giboni, M. Niewiera, and V. Schumpelick, "Elasticity of the anterior abdominal wall and impact for reparation of incisional hernias using mesh implants," *Hernia*, vol. 5, no. 3, pp. 113–118, 2001.

[43] D. C. Owens and J. C. Winters, "Pubovaginal Sling Using Duraderm™ Graft: Intermediate Follow-Up and Patient Satisfaction," *Neurourology and Urodynamics*, vol. 23, no. 2, pp. 115–118, 2004.

[44] A. Mangera, A. J. Bullock, C. R. Chapple, and S. MacNeil, "Are biomechanical properties predictive of the success of prostheses used in stress urinary incontinence and pelvic organ prolapse? A systematic review," *Neurourology and Urodynamics*, vol. 31, no. 1, pp. 13–21, 2012.

[45] K. L. Ward and P. Hilton, "A prospective multicenter randomized trial of tension-free vaginal tape and colposuspension for primary urodynamic stress incontinence: Two-year follow-up," *American Journal of Obstetrics and Gynecology*, vol. 190, no. 2, pp. 324–331, 2004.

[46] A. Mangera, A. J. Bullock, S. Roman, C. R. Chapple, and S. Macneil, "Comparison of candidate scaffolds for tissue engineering for stress urinary incontinence and pelvic organ prolapse repair," *British Journal of Urology*, vol. 112, no. 5, pp. 674–685, 2013.

[47] C. J. Hillary, S. Roman, A. J. Bullock et al., "Developing Repair Materials for Stress Urinary Incontinence to Withstand Dynamic Distension," *PLoS ONE*, vol. 11, no. 3, p. e0149971, 2016.

[48] M. J. Hung, M. C. Wen, C. N. Hung, E. S. Ho, G. D. Chen, and V. C. Yang, "Tissue-engineered fascia from vaginal fibroblasts for patients needing reconstructive pelvic surgery," *International Urogynecology Journal*, vol. 21, no. 9, pp. 1085–1093, 2010.

[49] M. Boennelycke, L. Christensen, L. F. Nielsen, S. Gräs, and G. Lose, "Fresh muscle fiber fragments on a scaffold in ratsa new concept in urogynecology?" *American Journal of Obstetrics and Gynecology*, vol. 205, no. 3, pp. 235–e14, 2011.

[50] S. F. Badylak, J. E. Valentin, A. K. Ravindra, G. P. McCabe, and A. M. Stewart-Akers, "Macrophage phenotype as a determinant of biologic scaffold remodeling," *Tissue Engineering A*, vol. 14, no. 11, pp. 1835–1842, 2008.

[51] T. Aboushwareb, P. Mckenzie, F. Wezel, J. Southgate, and G. Badlani, "Is tissue engineering and biomaterials the future for Lower Urinary Tract Dysfunction (LUTD)/Pelvic Organ Prolapse (POP)?" *Neurourology and Urodynamics*, vol. 30, no. 5, pp. 775–785, 2011.

Hindawi
International Journal of Biomaterials
Volume 2018, Article ID 8686794, 13 pages
https://doi.org/10.1155/2018/8686794

Review Article

Strain and Vibration in Mesenchymal Stem Cells

Brooke McClarren and Ronke Olabisi

Department of Biomedical Engineering, Rutgers University, 599 Taylor Rd, Piscataway, NJ 08854, USA

Correspondence should be addressed to Ronke Olabisi; ronke.olabisi@rutgers.edu

Received 20 October 2017; Accepted 28 November 2017; Published 9 January 2018

Academic Editor: Junling Guo

Copyright © 2018 Brooke McClarren and Ronke Olabisi. This is an open access article distributed under the Creative Commons Attribution License, which permits unrestricted use, distribution, and reproduction in any medium, provided the original work is properly cited.

Mesenchymal stem cells (MSCs) are multipotent cells capable of differentiating into any mesenchymal tissue, including bone, cartilage, muscle, and fat. MSC differentiation can be influenced by a variety of stimuli, including environmental and mechanical stimulation, scaffold physical properties, or applied loads. Numerous studies have evaluated the effects of vibration or cyclic tensile strain on MSCs towards developing a mechanically based method of differentiation, but there is no consensus between studies and each investigation uses different culture conditions, which also influence MSC fate. Here we present an overview of the response of MSCs to vibration and cyclic tension, focusing on the effect of various culture conditions and strain or vibration parameters. Our review reveals that scaffold type (e.g., natural versus synthetic; 2D versus 3D) can influence cell response to vibration and strain to the same degree as loading parameters. Hence, in the efforts to use mechanical loading as a reliable method to differentiate cells, scaffold selection is as important as method of loading.

1. Introduction

In tissue engineering and regenerative medicine, mesenchymal stem cells (MSCs) are often preferable to fully differentiated cells, which are limited in supply and do not multiply as rapidly or to as great an extent [1]. MSCs can proliferate for numerous passages. The MSC response to tensile strain and vibration has been researched using various scaffolds and stimulation parameters. Typical MSC responses to various mechanical loading include differentiation into osteocytes and chondrocytes, often guided by the presence of growth factors and calcium. Cell responses have also been guided by the microenvironment, whether cells are in their native environment, a transplanted *in vivo* environment, or cultured using tissue culture plastic, 2D scaffolds, or 3D scaffolds. Even the choice of scaffold material has an impact, that is, whether the scaffold is derived from natural or synthetic material. Although it is well known that MSCs respond to mechanical loading, it is not known how to best load these cells to achieve the desired differentiation. Identifying which combination of scaffold and loading protocol are associated with which MSC fate may permit researchers to reliably control differentiation without using differentiation media. Bending, tension, mechanical compression, hydrostatic compression, fluid shear, and vibration are all experienced by MSCs *in vivo*, as such their effects on MSCs have been explored extensively *in vitro*. When examining the aforementioned loading conditions, tensile strain of tissues is perhaps the easiest to measure *in vivo*, while vibration is the easiest to apply *in vivo*. Thus, for tensile strain and vibration, it is possible to compare their effects when applied *in vivo* versus *in vitro*. Therefore, this review focuses on the effect of tensile strain and vibration on the fate of MSCs in a variety of culture environments.

2. Common Methods to Differentiate MSCs

When maintained *in vitro*, MSCs can be chemically and mechanically differentiated into a variety of tissues such as bone, cartilage, tendon, and ligament [2]. The biochemical factors that promote specific cell responses are well understood and thus enable researchers to successfully guide cell differentiation. Adding chemical factors to cell culture media such as ascorbate, dexamethasone (dex), and bone morphogenetic proteins (BMPs) promotes osteogenesis; serum-free medium and transforming growth factor-β_1 (TGF-β_1) promote chondrogenesis; growth and differentiation factor

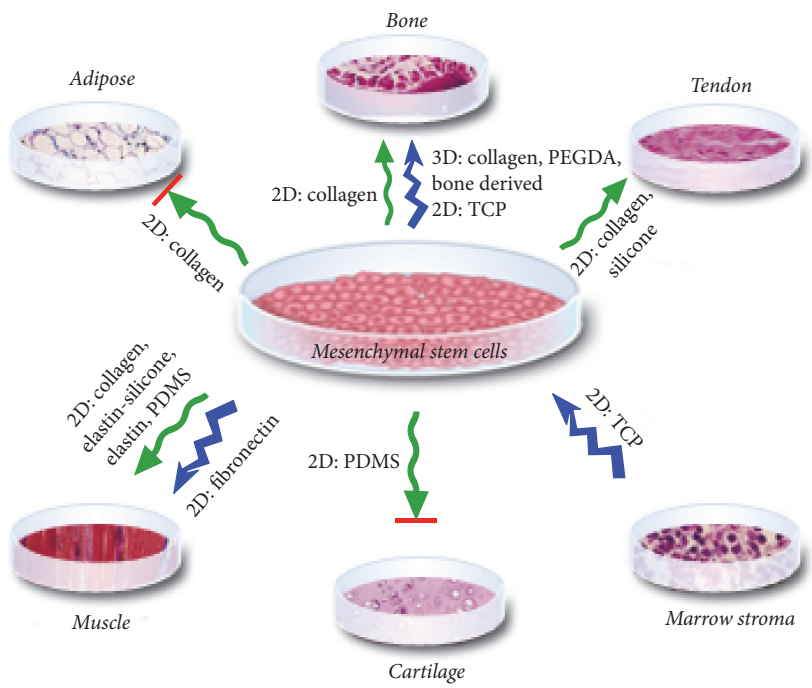

Figure 1: Diagram representing the effects of vibration (blue jagged arrow) and cyclic tensile strain (green squiggly arrow) on MSCs. The arrows depict the loading type. The italics detail the *in vitro* culture conditions in which the differentiation into the indicated lineage was observed. Red lines indicate inhibition of the downstream lineage. Tissue images from Tuan et al. [4], CC BY 4.0.

5 (GDF-5) promotes tenogenesis; platelet derived growth factor (PDGF) promotes myogenesis; and dex, insulin, and 3-isobutyl-1-methylxanthine (IBMX) promote adipogenesis (Figure 1) [3–5]. In addition to chemical factors, mechanical properties such as scaffold stiffness can be used to guide MSC differentiation [1, 6]. For instance, dex is widely used to promote MSC osteodifferentiation and alternately scaffolds with elastic moduli comparable to bone promote MSC osteodifferentiation [3, 6].

In their native environment tissues are subjected to a variety of biochemical signals in addition to a multitude of loading conditions that influence their development. In the absence of appropriate biochemical factors or scaffold mechanical properties, appropriate loading can drive MSC differentiation towards a desired fate [7]. Conversely, inappropriate loading can inhibit a desired fate [8]. MSC response to loading is dependent on stress/strain magnitude, duration, loading type, and force propagation through cytoskeletal configuration and attachment site geometry (for a recent review, see Delaine-Smith and Reilly) [3]. Loading types include such parameters as tension, compression, shear, bending, torsion, electromagnetic inputs, and vibration. Furthermore, loading can be separated into static or cyclic loading. All these loading types are experienced in situ by cells and often in combination. For example, in bone marrow, tension, compression, and fluid-induced shear may all be present but the effects of these forces on the stem cells within the bone marrow are not well understood [3, 9]. A challenge of tissue engineering is identifying the appropriate combination of chemical and mechanical parameters that will differentiate harvested MSCs into specific cell types *in vitro*. Although chemical inducers alone can drive differentiation *in vitro*, after scaffold implantation any biofactors it contains will eventually dissipate; thus the success of the scaffold will be maximized if its mechanical properties continue to influence cells.

3. The Effect of Vibration on Mesenchymal Stem Cells

Although vibration is not necessarily a loading condition experienced in nature, an extensive number of *in vivo* studies have been conducted with whole body vibration [33–39]. Whole body vibration studies have been used to model the cyclic tensile strain imparted on muscle or bone during physical actives such as walking, stair climbing, or weight lifting exercises [34]. The vibration stimulates the skeleton in a manner similar to walking or running and has been found to increase bone mass and bone strength [33–35, 40]. Whole body vibration stimulates osteogenesis of MSCs through mechanotransduction, resulting in a bone mass increase [35, 39]. Whole body vibration may also elicit a response from differentiated cells, which influence MSC differentiation [35]. Investigations exploring the effect of whole body vibration on MSCs may be confounded by the concurrent effect of vibration on differentiated cells. The mechanism of mechanotransduction during vibration in MSCs and subsequent response is not fully understood [36–38]. Additionally, the in situ response of cells to an external load cannot be separated from the systemic response of the whole organism.

Thus, researchers also explore *in vitro* parallels to whole body vibration to tease out the response of MSCs to vibration (summarized in Table 1). As such, the cell environment and

Table 1: Effect of vibration on MSCs.

Environment		Cell	Acceleration	Frequency [Hz]	Results	Ref.
TCP		hMSC	0.3 g	30, 400, 800	Osteogenic	[10]
		mMSC	0.15 g	90	Osteogenic	[11]
		rMSC	0.3 g	60	Osteogenesis inhibited*	[12]
		hMSC	0.1–0.6 g	10, 20, 30, 40	Cell proliferation	[13]
2D	Gelatin	hMSC	0.02 g	15, 30, 45, 60	Inconclusive*	[14]
	Collagen	mMSC	10 μstrain	90	Adipogenesis inhibited	[15]
	Fibronectin	hMSC	Acoustic	200	Myogenic	[16]
3D	Collagen Sponge	hMSC	0.3 g	30	Osteogenic	[13]
	Bone derived	rMSC	0.3 g	40	Osteogenic	[17]
	PEGDA	hMSC	0.3, 3, 6 g	100	Osteogenic	[18]

∗ indicates the addition of differentiation media.

loading factors can be controlled. When subjecting MSCs to vibration, investigators specifically select loading parameters, biochemical additives, and cellular environment to observe or induce differentiation of cells.

3.1. Tissue Culture Plastic. Most *in vitro* vibration studies are performed with a cell monolayer cultured on tissue culture plastic (TCP) [10–13, 41]. The MSC response to vibration depends on frequency, acceleration, and duration of stimulation.

Chen et al. investigated the effects of 0.3 g acoustic vibration at 30, 400, and 800 Hz on human MSCs (hMSCs) in cell culture plates [10]. Cells were stimulated 30 min/day for 7 days. The investigators selected 30 Hz because they noted that osteogenesis was promoted following whole body vibration under 100 Hz [35] and they selected higher frequencies because higher frequencies are more suited for localized body vibrations [10]. The authors found that cell proliferation, calcium deposition, and collagen 1 (Col I) gene expression increased the most following 800 Hz vibrations at 0.3 g (Figure 2). At 800 Hz, adipogenic gene expression and lipid accumulation were decreased while at 30 Hz adipogenesis was promoted. Though acoustic vibration differs from direct mechanical vibration, both methods impart physical vibration to the cells.

Demiray and Özçivici cultured mouse MSCs on glass cover slides within 6 well plates [11]. Plates were stimulated with low magnitude (<1 g) and high frequency (20–90 Hz; LMHF) vibrations of 90 Hz at 0.15 g over 7 days for 15 min/day. The authors hypothesized that low intensity vibrations would induce MSC differentiation into osteogenic cells. Following vibration, cells were tested for osteogenic markers Runx2 and osteocalcin (OC) to identify osteogenic differentiation. While gene expression of vibrated and control cells was similar, the vibrated cells exhibited increased proliferation and morphological changes. Vibrated cells also displayed increased cellular height and increased molecular expression of focal adhesion kinase.

Lau et al. studied the effects of LMHF vibration on rat MSCs cultured on TCP while using osteogenic media [12]. Cells were stimulated with 60 Hz vibrations at 0.3 g for six 1-hour bouts. The authors hypothesized that the vibration would promote osteogenesis based on prior animal and human studies [35, 42]. Following vibration, cells were tested for osteoblast-specific transcription factor Osterix (Osx) to detect osteoblastic differentiation. The MSCs displayed decreased Osx levels and inhibited mineralization, indicating that LMHF vibration did not enhance osteogenic differentiation but seemed to inhibit it. Further, LMHF vibration did not affect proliferation rate. As both the control and test groups contained osteogenic media, rather than a true investigation of the effects of LMHF, the study was more an investigation of the combined effect of LMHF and osteogenic media compared to osteogenic media alone.

Kim et al. tested hMSCs with a wide array of vibration frequencies and accelerations [13]. MSCs were seeded on TCP or a collagen sponge. The collagen sponge was prepared from a cross reaction of chondroitin-6-sulfate and type I collagen [43]. The cells were seeded within the pores of the sponge, creating a multidimensional scaffold. Cells were subjected to varying accelerations of vertical vibration for 10 min/day for 5 days using a custom platform on a shaker. Accelerations varied between 0.1, 0.2, 0.3, 0.4, 0.5, and 0.6 g and frequencies varied between 10, 20, 30, and 40 Hz. Vibration on TCP resulted in a minor increase of proliferation. At 0.2 g and 0.3 g accelerations, proliferation rates increased as frequency increased. For all frequencies, proliferation was significantly higher at 0.3 g compared to other accelerations. The highest proliferation was observed at 0.3 g for both 30 Hz and 40 Hz. Thus, their subsequent experiments were performed with 30 Hz vibrations delivering 0.3 g accelerations. In their differentiation assays, the authors found that the osteoblastic differentiation markers, alkaline phosphatase (ALP) and osteopontin (OPN), were upregulated in vibrated cells while the osteoblastic markers, OC and bone sialoprotein (BSP), were unaffected. Alizarin red staining was increased in MSC monolayers receiving vibration and osteogenic media compared to control, though staining was not increased for vibrated cells that did not receive osteogenic media. MSCs behaved differently on scaffolds compared to TCP. Specifically, while OPG, Col I, and VEGF expression showed significant increases in vibrated groups compared to nonvibrated groups, this effect was observed only in MSCs cultured on scaffolds. These differing results

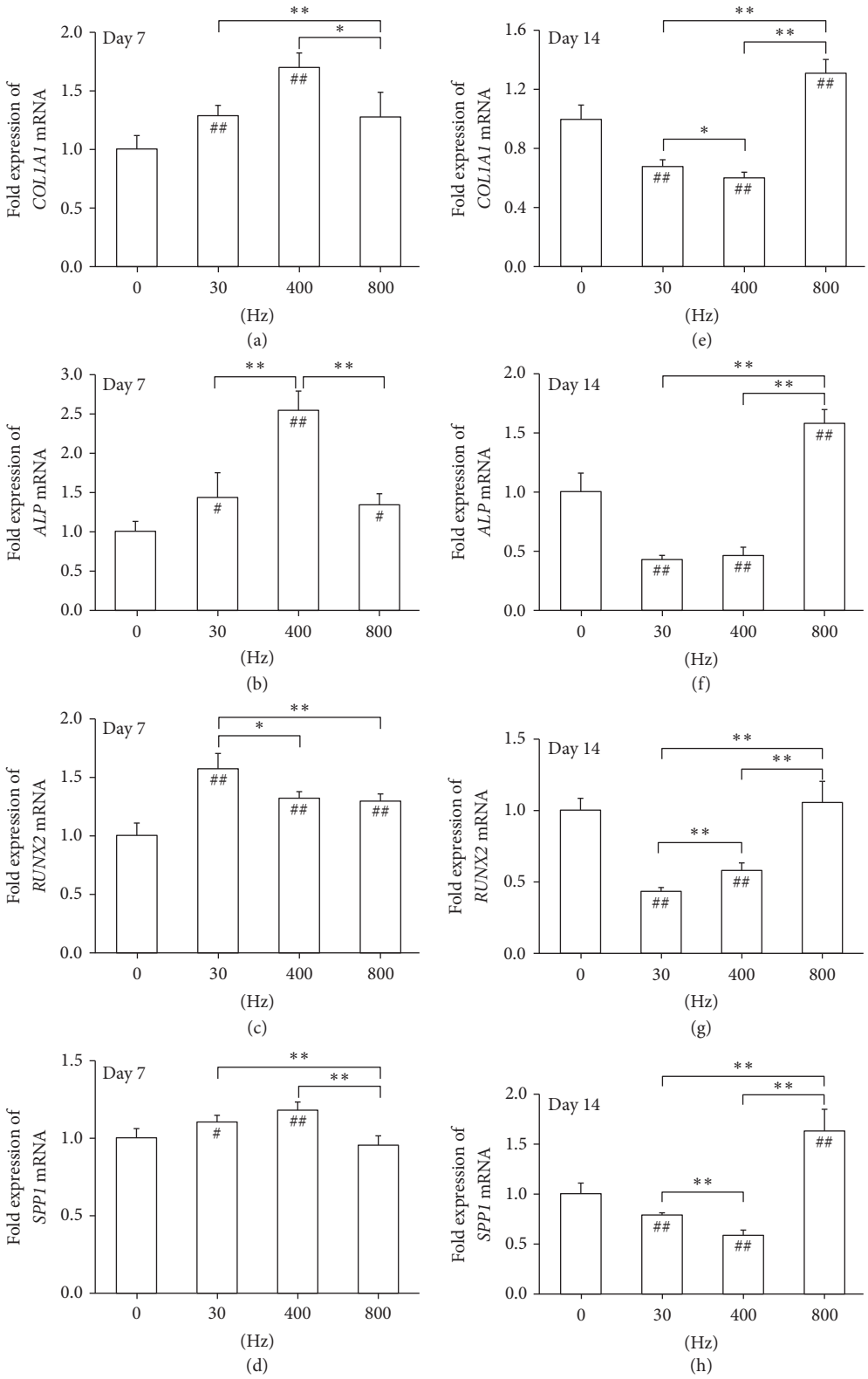

Figure 2: Acoustic-frequency vibratory stimulation (AFVS) modulates expression of mRNA encoding osteogenesis-specific markers in human bone marrow-derived mesenchymal stem cells (BM-MSCs) at the time points of day 7 ((a), (b), (c), and (d)) and day 14 ((e), (f), (g), and (h)). The mRNA levels of COL1A1 ((a), (e)), ALP ((b), (f)), RUNX2 ((c), (g)), and SPP1 ((d), (h)) were measured by real-time RT-PCR. Values are mean ± standard error of four independent experiments ($n = 4$). $^{*}P < 0.05$; $^{**}P < 0.01$ in the indicated groups from unpaired t-test. $^{\#}P < 0.01$; $^{\#\#}P < 0.01$ compared with the 0 Hz control group from unpaired t-test. From Chen et al. [10], CC BY 3.0.

suggest that additional factors, such as microarchitectural differences between scaffolds and TCP, may influence the mechanotransduction of vibration.

It is well known that cells in culture do not behave the same on TCP as they do in scaffolds or in their natural environments [44–48]. The same holds true for cells subjected to vibration [12, 13, 21, 43, 44]. Further, vibrated cells on TCP do not necessarily behave identically between similar investigations. In several LMHF studies, osteogenesis was increased significantly when MSCs on TCP were vibrated at accelerations of 0.3 g at 35 Hz or 45 Hz [49, 50]. Conversely, in other studies that vibrated MSCs on TCP with 0.3 g accelerations at 30 Hz or 60 Hz, osteogenesis was inhibited [13, 21]. Considering the variation in MSC response that TCP elicits, scaffolds may provide a more accurate and consistent in situ representation of the MSC response to vibration.

3.2. Two-Dimensional Scaffolds. Scaffolds provide a more complex cellular interaction than a simple monolayer on TCP. A 2D scaffold has cells cultured on a flat surface while a 3D scaffold has cells embedded within or seeded on a multidimensional surface. Two-dimensional scaffolds for vibration studies are often membranes coated with osteogenic proteins or minerals [15, 16, 51]. Cell attachment and force transmission vary with different scaffolds or bound matrix proteins.

Edwards and Reilly seeded hMSCs in gelatin coated 12-well plates [14]. Plates were subjected to LMHF vibrations of 15, 30, 45, or 60 Hz at 0.02 g. Vibration occurred for 10 or 45 minutes. The authors also investigated the effect of osteogenic media (media containing dex) during their vibration studies. Alkaline phosphatase (ALP) activity was the only measurement of cell commitment. ALP activity was greatest following 45-minute vibrations of 60 Hz with osteogenic media. Forty-eight hours after stimulation, MSCs subjected only to vibration did not demonstrate a statistically relevant increase of ALP activity. ALP activity was greater in cells that had dex+ media compared to dex− media. For dex+ cells, 60 Hz stimulation had a statistically greater ALP activity compared to other frequencies.

Sen et al. investigated the inhibition of adipogenesis in mouse MSCs after vibration [15]. The authors subjected MSCs seeded on a collagen-coated silicon membrane to low intensity vibrations of <10 microstrain, at 90 Hz. The MSCs were stimulated for 20 minutes twice a day. Following vibration, cells were tested for the adipogenic markers adiponectin, PPARγ2, and aP2. The MSCs expressed decreased levels for all adipogenic markers and the development of lipid granules was inhibited. The authors also investigated the synergistic effect of vibration and adipogenic media. The MSCs subjected to vibration and adipogenic media had a statistically insignificant expression of adipogenic markers. The results indicate that adipogenesis was inhibited in cells subjected to vibration and that treatment with adipogenic media did not recover adipogenesis. Conversely, markers for osteogenic differentiation were promoted significantly after vibration, though this effect was only observed in MSCs treated with adipogenic media.

Tong et al. subjected hMSCs to 200 Hz acoustic vibration to replicate vocal cord vibrations [16]. Cells were seeded on PCL scaffolds coated with fibronectin and subjected to vibrations for 12 hrs/day over 7 days continuously or discontinuously. All vibrated cells expressed enhanced F-actin and a5b1 integrin expression. Levels of vocal fold extracellular matrix components were significantly elevated. Myogenic differentiation in MSCs were indicated by elevated levels of tenascin-C, collagen III, and procollagen I, while osteogenic markers were not expressed.

Edwards and Reilly, similar to Lau et al., found that a synergist effect of vibration and osteogenic media promoted osteogenesis [12, 14]. Sen et al. found adipogenesis to be inhibited after vibration, even with the addition of adipogenic media. Tong et al. found myogenic differentiation of hMSCs seeded on fibronectin-coated scaffolds [16]. Each of these studies used a different biological coating on a synthetic scaffold. It is important to consider that the different MSC responses to vibration observed by these studies may in part be explained by different MSC responses to the scaffolds. In short, the biological components of the scaffolds are potentially introducing a compounding biological variable to the investigations, contributing to the observed synergistic responses.

3.3. Three-Dimensional Scaffolds. Few studies of MSC response to vibration *in vitro* have used three-dimensional substrates [10–13, 15, 16, 51]. Three-dimensional substrates translate mechanical force to cells via different mechanisms than 2D substrates [52]. Three-dimensional substrates may better model in situ cell attachment and the resultant effects of mechanical loading [53]. In 3D environments, there are increased cell-to-cell contact and cell-to-extracellular matrix interactions compared to 2D monolayers [53]. Due to these factors, cells within 3D scaffolds likely better model the *in vivo* response to vibration than cells on 2D substrates.

3.3.1. Natural Scaffolds. Kim et al. vibrated hMSCs after inoculation on a collagen sponge [13]. Cells were exposed to 30 Hz vibration at 0.3 g. In their differentiation assay, the authors found that the osteogenic markers OPG, Col I, and VEGF expression were increased after MSCs were vibrated. These results differ from the previously described results of Chen et al., who found increased adipogenesis in TCP-monolayer hMSCs subjected to 30 Hz vibration at 0.3 g. The difference in the response of MSCs within a 3D scaffold and MSCs in a monolayer suggests that factors such as microarchitectural cues may mechanotransduce vibration.

Zhou et al. subjected rat MSCs seeded on 3D bone-derived scaffolds to LMHF vibration [17]. The hollow components of the scaffolds allowed cells to attach within the multidimensional matrix. Rat MSCS seeded on TCP were used as control groups. The authors vibrated cells with 40 Hz at 0.3 g for 6 hours. The vibrated MSCs demonstrated increased levels of osteogenic markers ALP, Coll I, and OC. ALP activity was significantly higher in cells vibrated within 3D scaffolds than cells vibrated on TCP (Figure 3). However, vibration resulted in lower proliferation after day 7. The increased response from vibrated MSCs within 3D scaffolds compared to MSCs on TCP should motivate further investigation of MSCs within 3D scaffolds.

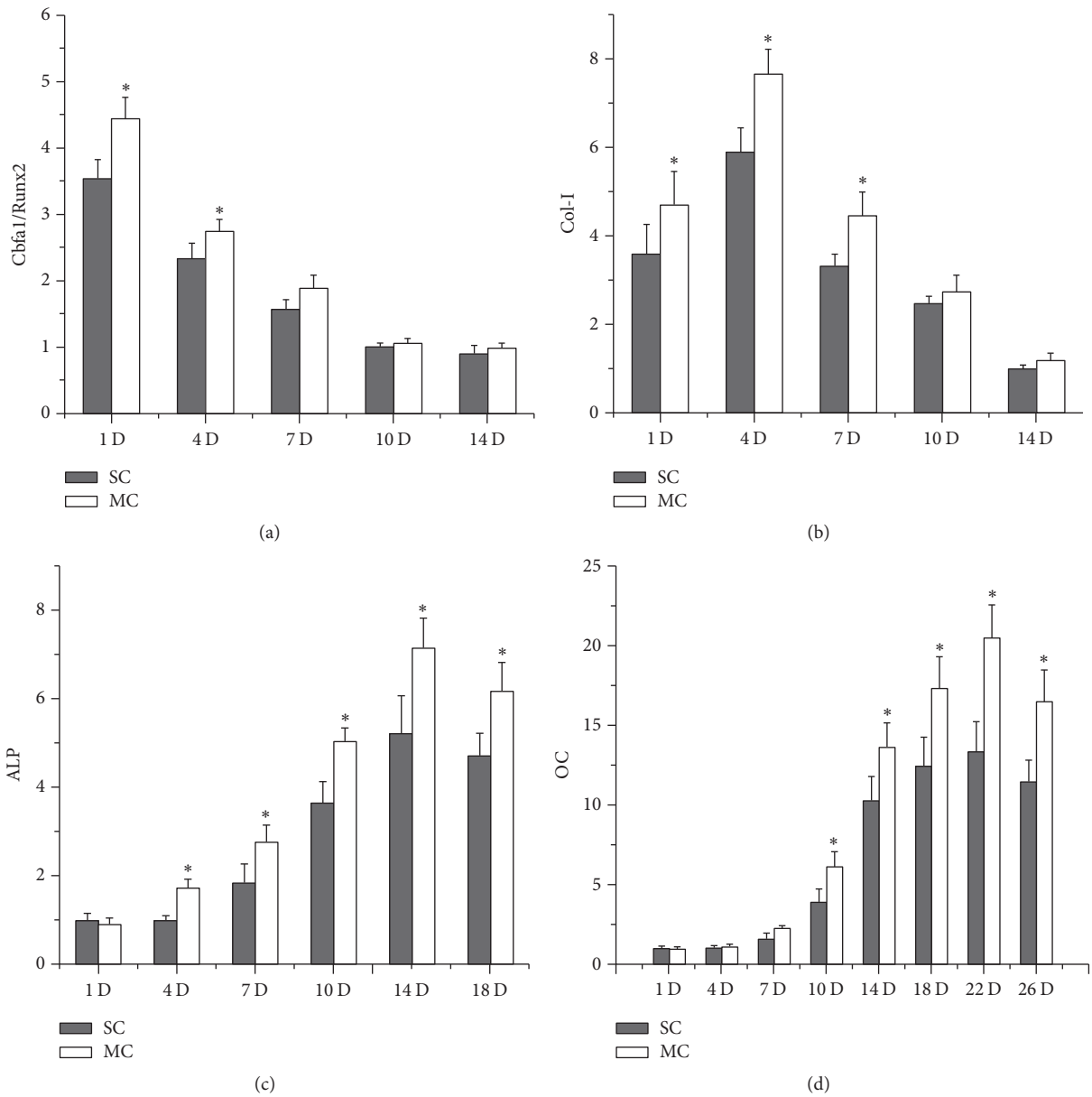

Figure 3: Effect of microvibration on osteogenic gene expressions in BMSC cellular scaffolds. Cbfa1/Runx2, Col I, ALP, and OC mRNA expressions were assayed on days 1, 4, 7, 10, 14, 18, 22, and 26. Data show that microvibration greatly upregulated these mRNA levels at different stages of osteogenesis. Each bar represents the mean ± standard deviation ($n = 3$); $^{*}P < 0.05$. SC, static culture. MC, microvibration culture. Col I, collagen I. ALP, alkaline phosphatase. OC, osteocalcin. From Zhou et al., [17] with kind permission from eCM journal (http://www.ecmjournal.org).

3.3.2. Synthetic Scaffolds. To the author's knowledge, our laboratory has conducted the only vibration studies on MSCs entrapped within a synthetic material [18]. Cells entrapped within PEGDA microspheres were subjected to vibrations of 100 Hz at 0.3 g, 3.0 g, or 6.0 g for 24 hours. Cells were subsequently tested for adipocyte, chondrocyte, and osteoblast differentiation. Osteogenic differentiation in MSCs was observed at 0.3 and 3.0 g accelerations, while 6.0 g accelerations were lethal to cells. Alkaline phosphatase activity was observed on day 4 in MSCs subjected to 0.3 and 3.0 g. Alizarin red staining was also significantly increased in 0.3 and 3.0 g MSCs compared to nonvibrated controls. Chondrogenesis and adipogenesis were not observed at any time point.

The vibration studies expose MSCs to a range of accelerations and frequencies. Accelerations from 0.02 g to 6.0 g were used in combination with frequencies ranging from 10 to 800 Hz (Table 1). With such variations in vibration parameters, it is unsurprising that there is a great variation in observed response. However, when probing further, the disparity in cell response is mostly observed in cells seeded on 2D scaffolds. MSCs on or within 3D scaffolds uniformly

Table 2: Effect of cyclic tensile strain on MSCs seeded on 2D scaffolds.

Scaffold		Cell	Strain (%)	Time (hrs)	Differentiation	Ref.
2D Natural	Collagen	hMSCs	5	24	Myogenic	[19]
		hMSCs	10	24	Myogenic*	[20]
		hMSCs	3, 10	8, 48	Tenogenic (10%)	[21]
		hMSCs	0.8, 5, 10, 15	48	Osteogenesis (<5%) Osteogenic inhibition (>5%)	[22]
2D Natural + synthetic	Elastin	hMSCs	10	24	Myogenic*	[20]
	Silicone	rMSCs	10	N/A	Tenogenic	[23]
	Elastin-silicone	rMSCs	5, 10, 15, 20	24	Myogenic (10%)	[24]
	Elastin-silicone	rMSCs	10	24, 48, 72	Myogenic	[24]

* Myogenic expression transiently increased; expression reduced to basal levels after cell alignment.

differentiated to bone. While 3D scaffolds were tested in a smaller range of vibration parameters (0.3–6 g; 30–100 Hz), these studies may point to a uniform response to MSCs when vibrated within a 3D environment.

4. The Effect of Cyclic Tensile Strain on MSCs

Cyclic uniaxial tensile strain can be applied to cells encapsulated in or seeded on a flexible scaffold. Rigid materials such as TCP cannot be used for tensile strain studies. Silicon scaffolds are regularly used as a synthetic, flexible scaffold. The effects of tensile strain on MSCs, inducing tenogenic, osteogenic, and myogenic responses, have been investigated and are reviewed below [3, 19–32].

4.1. Two-Dimensional Scaffolds

4.1.1. Natural Scaffolds. The following studies investigate the effects of cyclic uniaxial tensile strain with magnitudes between 0.8% and 15% at 1 Hz on MSCs seeded on collagen membranes and other scaffolds (Table 2) [19–22]. The strain magnitudes were selected by the authors to replicate the tensile strain experienced in situ by bone, muscle, and tendon.

Chen et al. seeded hMSCs on collagen type I coated scaffolds and then subjected them to 3% and 10% cyclic tensile strain at 1 Hz for 8 or 48 hours [21]. The authors were investigating osteogenic or tenogenic commitment of MSCs following such strain. For all strains, organized cell alignment was noted. Cells subjected to both strain rates became longer, slenderer in shape, and oriented perpendicular to the axis of strain. hMSCs subjected to 3% strain for 8 hours demonstrated an upregulation of osteoblastic markers with increased levels of ALP and Cbfa1. hMSCs strained at 10% for 48 hours demonstrated significant increases in type I collagen, type III collagen, and tenascin-C, indicating tenogenic differentiation. The authors suggested strain amplitude and duration of strain may influence tenogenic and osteogenic commitment of MSCs.

Park et al. aimed to replicate the strain conditions of vascular smooth muscle on hMSCs seeded on elastin or collagen-coated membranes [20]. MSCs were subjected to 10% uniaxial tensile strain at 1 Hz for 24 hours. Smooth muscle cell (SMC) and osteogenic markers were investigated. Following strain, cells in both scaffolds increased collagen I expression; however, markers of osteogenic differentiation were not significant. After being subjected to strain, levels of smooth muscle markers α-actin, SM-22α, and β-actin were transiently increased in cells on both scaffolds (Figure 4). Expression of α-actin and SM-22α subsequently decreased shortly after cells aligned themselves perpendicular to the direction of strain. After 3 days, SM-22α decreased by 50% on collagen-coated scaffolds and 25% on elastin-coated membranes. Levels of Col I also decreased after alignment. The authors concluded that uniaxial strain may promote MSC differentiation into SMCs if the cell orientation is fixed. Interestingly, the decrease in gene expression after alignment described by Park et al. contradicts the stable gene expression described by Chen et al., who did not observe decreased gene expression from MSCs subjected to 10% strain [20, 21].

Khani et al. investigated the mechanical properties of hMSCs subjected to uniaxial strain with or without chondrogenic media (with TGF-β_1) [19]. hMSCs were seeded on poly(dimethyl siloxane) (PDMS) with a collagen coating to enable cell attachment. For 24 hours seeded hMSCs were subjected to uniaxial strain of 5% at 1 Hz, comparable to physiological levels within human arteries. Strained cells without TGF-β_1 had significantly increased Young's Moduli (E) and elevated levels of the smooth muscle markers ASMA, h1-Calponin, and SM22A. The strained hMSCs demonstrated increased myogenesis with or without TGF-β_1 in the media. After stimulation, these cells had also become aligned perpendicular to the axis of strain. The authors suggested that the realignment of these cells may reinforce the material, creating a stiffer composition, and may ultimately impact mechanotransduction.

Koike et al. subjected hMSCs seeded on collagen I coated membranes to 0.8%, 5%, 10%, and 15% cyclic strain at 1 Hz for 2 days [22]. Cell proliferation significantly increased at 5%, 10%, and 15% strain compared to unloaded controls. At 1-hour and 6-hour markers, Cbfa1/Runx2 increased at 0.8% and 5% strain but decreased at 15% strain. At 24 hours and 48 hours, cell proliferation and Col I increased at 5%, 10%, and 15% strain while Cbfa1/Runx2 expression, osteocalcin expression, and ALP activity were significantly decreased. ALP activity was increased at 0.8% strain. These results indicate that high magnitude mechanical strain will inhibit osteoblastic

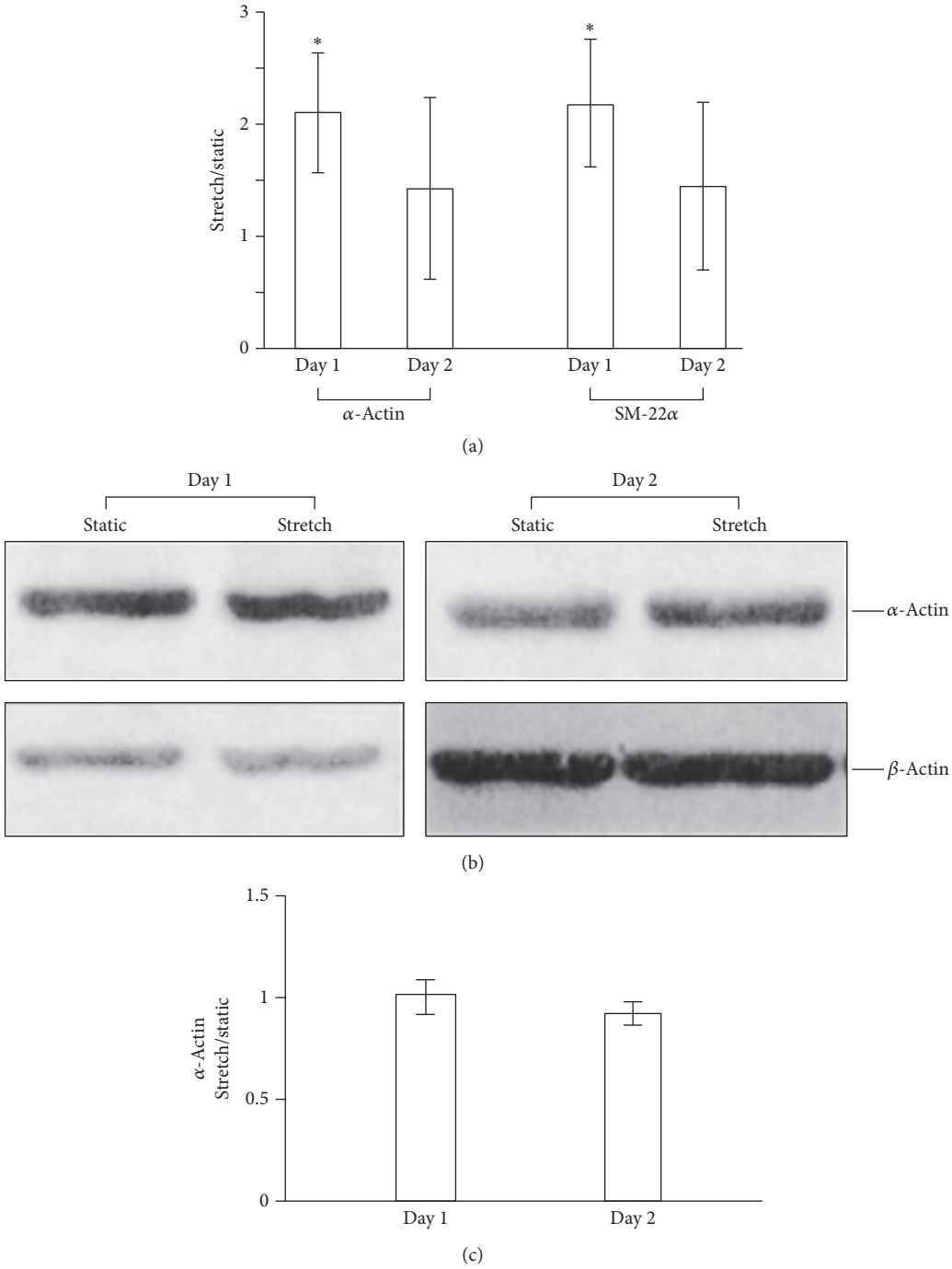

Figure 4: Effects of uniaxial strain on SM marker expression in MSCs. MSCs were cultured on collagen-coated elastic membranes for 1 day and subjected to 10% uniaxial strain at 1 Hz or kept as static controls for 1 and 2 days. (a) The RNA from each sample was reverse-transcribed into cDNA and the gene expression of SM a-actin, SM-22a, and GAPDH was analyzed by qPCR with their respective primers. The expression level of each gene was normalized with the level of GAPDH in the same sample. The ratio of the gene expression (stretch/static) is presented as mean (±) standard deviation from at least three experiments. *Significant difference ($P < 0.05$) from 1. (b) The protein expression of SM a-actin and actin was analyzed by immunoblotting with respective antibody. (c) Statistical analysis of protein expression. The protein expression was quantified, and the expression level of a-actin was normalized with the level of h-actin in the same samples. The ratio of the normalized protein expression (stretch/static) is presented as mean (±) standard deviation from at least three experiments. From Park et al., Biotechnology and Bioengineering [20]. Copyright© 2004 by John Wiley Sons, Inc. Reprinted by permission of John Wiley & Sons, Inc.

differentiation, while strain at low magnitudes may enhance osteoblastic differentiation.

All studies described above used collagen scaffolds to investigate the response of hMSCs to uniaxial tensile strain [19–22]. On collagen scaffolds, MSCs subjected to low magnitude tensile strains (≤3%) underwent osteogenic differentiation [21, 22, 54]. At greater tensile strains (5%), myogenic differentiation was promoted [19, 22]. hMSCs subjected to high magnitude tensile strains (≥10%) showed an inhibition of osteogenic differentiation, transiently enhanced myogenic differentiation, and enhanced tenogenic differentiation [20–22]. The literature generally agrees that MSC osteodifferentiation occurs at lower strain magnitudes than MSC tenodifferentiation [19–22, 54].

4.1.2. Synthetic Scaffolds. Park et al. noted a difference in MSC response to a synthetic scaffold compared to a collagen scaffold [20]. As described in Section 4.1.1, Park et al. subjected MSCs seeded on elastin-coated or collagen-coated scaffolds to 10% uniaxial tensile strain at 1 Hz for 24 hours. The hMSCs transiently upregulated smooth muscle markers. Smooth muscle gene expression was higher in cells seeded on the elastin scaffolds. The authors suggested that the MSCs sensed a difference in the mechanical loading of the two microenvironments.

Zhang et al. subjected rMSCs seeded on a silicone scaffold to 10% tensile strain at 1 Hz [23]. The authors investigated the effect of tensile strain on tenogenesis of hMSCs. The authors also investigated the effects of coculturing hMSCs with ligament fibroblasts. Only cells subjected to strain exhibited morphological changes. After tensile strain, rMSCs had a more elongated fibroblast-like cell type. The strain triggered an early upregulation of Col I and Col III. Tenascin-C expression was also upregulated in cells subjected to strain. Cells subjected to strain demonstrated greater levels of tenogenic gene expression than cells cocultured with fibroblasts but not subjected to strain.

Huang et al. subjected rMSCs seeded on an elastic-silicone membrane to 5%, 10%, 15%, and 20% tensile strain at 1 Hz for 24 hours [24]. The authors investigated the presence of cardiac-related gene expression using negative controls and positive controls. Cells subjected to cyclic strain expressed GATA-4, β-MHC, NKx2.5, and MEF2c. Gene expression was greatest in cells subjected to 10% strain. The researchers then subjected rMSCs to 10% strain at 1 Hz for 24, 48, and 72 hours. The expression of GATA-4, β-MHC, NKx2.5, and MEF2c was significantly increased for all durations of strain. The investigators suggested that cyclic mechanical strain of 10% at 1 Hz induces cardiomyogenic differentiation of MSCs.

Jagodzinski et al. applied tensile strain to hMSCs seeded on a silicone scaffold [55]. Cells were subjected to 2% or 8% strain, six hr/day for three days at 1 Hz. hMSCs were cultivated with (dex+) or without (dex−) dexamethasone. For both strain magnitudes, cells had significantly increased ALP secretion and collagen III upregulation. Cells subjected to 8% strain significantly upregulated Col I and Cbfa1. Cells that underwent strain had significantly greater gene expression, with or without dex, for all markers of gene expression. At both high and low magnitudes of cyclic strain, hMSC osteogenic commitment was enhanced on silicon scaffolds, contrary to the observed trends of hMSCs on collagen scaffolds, which showed tenogenic commitment at high strain magnitudes and osteogenic commitment at low strain magnitudes.

After being subjected to 10% strain, MSCs seeded on synthetic scaffolds demonstrated enhanced myogenic differentiation, resulting in fibroblasts, smooth muscle cells, and cardiac cells [20, 23, 43]. For other strain magnitudes, MSCs seeded on synthetic scaffolds respond differently to tensile strain than MSCs seed on natural scaffolds [20, 23, 24, 55]. Cells on synthetic scaffolds had a greater expression of smooth muscle markers compared to cells on natural scaffolds [20]. Osteodifferentiation was induced at high magnitudes of strain in cells on silicone while osteogenesis was inhibited at high magnitudes of strain in cells on collagen [55]. Thus, demonstrating that the MSC response to strain differs on synthetic-based scaffolds compared to natural scaffolds.

While the preceding scaffolds were comprised of synthetic materials, only one was not modified with elastin. The MSCs on scaffolds comprised of or modified with elastin all exhibited myodifferentiation. The MSCs on truly synthetic scaffolds exhibited tenodifferentiation. Thus, for 2D scaffolds, scaffold type may be more important than the loading.

4.2. Three-Dimensional Scaffolds. Cells entrapped within a scaffold or seeded throughout a structure are subjected to a different microenvironment than cells seeded on a planar scaffold. Subtle differences in loading or cell-cell communication may impact cell response to strain. The following studies investigate the effects of cyclic strain on cells entrapped within 3D scaffolds (Table 3).

4.2.1. Natural Scaffolds. The first study to investigate hMSCs entrapped in 3D collagen matrix under cyclic strain was conducted by Sumanasinghe et al. [25]. The authors subjected hMSCs entrapped within a collagen matrix to 10% or 12% uniaxial cyclic tensile strain at 1 Hz for 4 hr/day. Strain was applied for 7 or 14 days. hMSCs remained highly viable for all strain conditions. hMSCs subjected to 10% strain demonstrated a significant increase in BMP-2 expression for both durations of strain. Cyclic strain of 12% induced a significant increase in BMP-2 expression only in cells subjected to 14 days of strain. The authors concluded that strain alone can induce osteogenic differentiation without the addition of osteogenic supplements.

Sumanasinghe et al. conduced a follow-up study to investigate the expression of proinflammatory MSC cytokines using identical strain conditions (10 or 12%; 1 Hz for 4 hr/day; 7 or 14 days) [26]. The authors also used osteogenic media to evaluate the combined effect of cyclic strain and osteogenic supplements. Initially, hMSCs undergoing strain had reduced viability. After day 6, hMSCs subjected to 10% strain had increased viability. Only strained cells receiving osteogenic media had increased levels of TNFα and IL-Iβ. The authors demonstrated that hMSCs entrapped within a collagen matrix maintain high viability after cyclic strain.

Table 3: Effect of cyclic tensile strain on MSCs within 3D scaffolds.

Scaffold		Cell	Strain (%)	Time (hrs)	Differentiation	Ref.
3D Natural	Collagen	hMSCs	10, 12	28, 56	Osteogenic	[25]
		hMSCs	10	56	Osteogenic	[26]
		hMSCs	10	168	Tenogenic	[27]
		rbMSCs	2.4	96	Inconclusive	[28]
3D Synthetic hydrogel	(RGD/RGE)	hMSCs	3	2, 24	Gene expression ↑ (RGD)	[29]
	PLA	hMSCs	2, 5	15	Inconclusive	[30]
	PEG	hMSCs	10	168	Tenogenic	[31]
	OPC	hMSCs	10	252	Tenogenic	[32]

Charoenpanich et al. entrapped hMSCs, specifically adipose derived stem cells, within a collagen I gel sheet [56]. The entrapped cells were subjected to 10% cyclic tensile at 1 Hz for 4 hr/day over 14 days. The authors performed a microarray analysis of 847 genes and found 184 transcripts affected by tensile strain. Network analysis suggested that strain may impact osteogenic differentiation by upregulation of proinflammatory cytokine regulator interleukin-1 receptor antagonist (IL1RN) and angiogenic inductors including fibroblast growth factor 2 (FGF-2) and vascular endothelial growth factor A (VEGF-A). Cells subjected to strain and osteogenic media resulted in significantly increased calcium deposits, suggesting a synergistic effect of the strain and media driving the cells towards osteogenic differentiation.

Qiu et al. applied cyclic strain to hMSCs seeded along collagen fibers to investigate fibroblastic differentiation [27]. The fibrous scaffold provided a nonplanar microenvironment. The hMSCs were subjected to 10% tensile strain at 1 Hz for 12 hrs/day over 14 days. Collagen I, collagen III, tenascin-C, and fibroblastic transcription factor scleraxis were all found to be significantly upregulated in cyclically strained hMSCs compared to unstrained control cells. Thus, 10% cyclic strain significantly promoted tenogenic differentiation of hMSCs.

Juncosa-Melvin et al. applied strain to rabbit MSCs seeded within collagen sponges [28]. MSCs were subjected to cyclic strain of 2.4% at 0.003 Hz for 8 hrs/day over 12 days. Tenogenic differentiation was not conclusively promoted by cyclic strain, but significant gene expression of collagen I and collagen III was induced by cyclic strain. Strained MSCs showed 3 or 4 times greater collagen I and collagen III production compared to unstrained controls. However, gene expression of fibronectin or decorin was not significantly increased in strained MSCs.

Few studies investigate both the effects of 3D scaffolds and cyclic tensile strain on hMSC differentiation without osteogenic supplements. In the few studies that do not use osteogenic media, most use scaffolds or coatings comprised of collagen, which is a major component in bone and hence provides a biological factor that induces its own cell response [57, 58].

4.2.2. Synthetic Scaffolds. Rathbone et al. investigated the response of hMSCs to cyclic tensile strain entrapped within 3D hydrogels with either the cell attachment tripeptide, arginylglycylaspartic acid (RGD), or a dummy tripeptide, arginyl-glycyl-glutamic acid (RGE) [29]. Cells were either entrapped within a hydrogel with cell attachment sites (RGD) or entrapped within a hydrogel without cell attachment sites (RGE). The authors' hydrogel was composed of Fmoc-FF:Fmoc-RGD/RGE. The hMSCs were subject to 3% strain 1 Hz for 1 hour or 24 hours and evaluated 2 hours or 24 hours after strain. Cells within hydrogels demonstrated high viability. The authors investigated CCNL2, WDR61, and BAHCC1 as potentially important mechanosensitive genes. After 1 hour of strain, hMSCs on monolayers significantly downregulated CCNL2, WDR61, and BAHCC1. After 24 hours of strain, hMSCs on monolayers significantly upregulated BAHCC1. BAHCC1 was not expressed by hMSCs in either of the 3D scaffolds. WDR61 was significantly upregulated by hMSCs in both 3D scaffolds after 1 hr of strain. CCNL2 was upregulated in hMSCs only in scaffolds with RGD. The cell response differed when in a monolayer or in a 3D scaffold and when within 3D scaffolds with or without RGD, thus indicating the impact of attachment sites on mechanotransduction in otherwise identical scaffolds.

Kreja et al. applied strain to hMSCs seeded throughout a novel textured PLA scaffold to investigate fibroblastic differentiation [30]. Cells were subjected to 2% or 5% strain at 1 Hz for 1 hr/day over 15 days. The authors analyzed the gene expression of ligament matrix markers: collagen I, collagen III, fibronectin, tenascin-C, decorin, MMP-1, MMP-2, and inhibitors TIMP-1 and TIMP-2. Cells subjected to strain did not demonstrate significant gene expression except in the downregulation of both MMP-1 and TIMP-2 in cells subjected to 5% strain. For both strain parameters, tenogenic differentiation was not promoted in hMSCs.

Yang et al. investigated the effects of strain on hMSCs entrapped within fast and slow degrading MMP-sensitive PEG hydrogels to investigate tenogenic differentiation [31]. Cells were subjected to 10% strain at 1 Hz for 12 hrs/day over 14 days. Cell realignment in response to the strain direction was not observed. hMSCs within the slow degrading hydrogel upregulated collagen III by 3.8-fold and upregulated tenascin-C by 2.5-fold while hMSCs within the fast degrading hydrogel upregulated collagen III by 2.1-fold and upregulated tenascin by 1.7-fold. The authors suggested that cyclic straining promoted tenogenic differentiation and that the presence of strain had a greater influence on cell differentiation than the difference in composition between the hydrogels.

Doroski et al. expanded the Yang et al. investigation where hMSCs entrapped with PEG-based hydrogels were cyclically strained [31, 32]. The researchers entrapped hMSCs within oligo(poly(ethylene glycol) fumarate) (OPF). Cells were then subjected to 10% strain at 1 Hz for 12 hrs/day over 21 days. By day 21, cyclic strain significantly upregulated the tenogenic markers collagen I, collagen III, and tenascin-C, while osteogenic, chondrogenic, and adipogenic markers were not increased. Thus, the cyclic strain promoted tenogenic differentiation.

It is interesting to note that collagen derived scaffolds mostly resulted in osteodifferentiation while synthetic scaffolds mostly resulted in tenodifferentiation. These results indicate that if seeking to differentiate MSCs using mechanical loading such as tensile strain, the scaffold material type will influence the MSC fate as much as the loading parameters will.

5. Summary

The response of MSCs subjected to cyclic strain and vibration appear to vary with loading parameter as much as it varies with culture conditions. Unsurprisingly, for similar loading conditions, TCP produced different results than 2D scaffolds, which in turn produced different results than 3D scaffolds. The varying effects of natural and synthetic scaffolds on MSC differentiation may be explained by the differing elastic moduli between these scaffolds or it may be the distinct microarchitecture of a natural scaffold compared to featureless synthetic scaffolds, or the dominating factor may be the native biochemical cues contained within natural scaffolds. These questions warrant further investigation if mechanical loading is to be pursued as an alternate method to induce MSC differentiation.

6. Future Perspectives

Future investigations of MSC differentiation using vibration and cyclic strain should explore varying types of natural scaffolds in concert with the loading parameters. Collagen is a primary component of bone and as such makes an ideal bone scaffold. Vibration within 3D collagen scaffolds ultimately led to osteogenic differentiation. Future studies utilizing scaffolds optimized for myogenic, adipogenic, or tenogenic differentiation should be explored to tease out whether vibration and/or cyclic strain in 3D scaffolds consistently leads to osteogenic differentiation or whether vibration and/or cyclic strain in 3D scaffolds leads to tissue optimized for that 3D scaffold.

Conflicts of Interest

The authors declare that they have no conflicts of interest.

References

[1] H. Lv, L. Li, M. Sun et al., "Mechanism of regulation of stem cell differentiation by matrix stiffness," *Stem Cell Research & Therapy*, vol. 6, no. 1, article no. 103, 2015.

[2] C. Vater, P. Kasten, and M. Stiehler, "Culture media for the differentiation of mesenchymal stromal cells," *Acta Biomaterialia*, vol. 7, no. 2, pp. 463–477, 2011.

[3] R. M. Delaine-Smith and G. C. Reilly, "Mesenchymal stem cell responses to mechanical stimuli," *Muscle, Ligaments and Tendons Journal*, vol. 2, no. 3, pp. 169–180, 2012.

[4] R. Tuan, G. Boland, and R. Tuli, "Adult mesenchymal stem cells and cell-based tissue engineering," *Arthritis Research & Therapy*, vol. 5, no. 1, 2003.

[5] C. Nombela-Arrieta, J. Ritz, and L. E. Silberstein, "The elusive nature and function of mesenchymal stem cells," *Nature Reviews Molecular Cell Biology*, vol. 12, no. 2, pp. 126–131, 2011.

[6] Y.-R. V. Shih, K.-F. Tseng, H.-Y. Lai, C.-H. Lin, and O. K. Lee, "Matrix stiffness regulation of integrin-mediated mechanotransduction during osteogenic differentiation of human mesenchymal stem cells," *Journal of Bone and Mineral Research*, vol. 26, no. 4, pp. 730–738, 2011.

[7] P. M. Tsimbouri, P. G. Childs, G. D. Pemberton et al., "Stimulation of 3D osteogenesis by mesenchymal stem cells using a nanovibrational bioreactor," *Nature Biomedical Engineering*, vol. 1, no. 9, pp. 758–770, 2017.

[8] L. Tan, B. Zhao, F. Ge, D. Sun, and T. Yu, "Shockwaves inhibit chondrogenic differentiation of human mesenchymal stem cells in association with adenosine and A2B receptors," *Scientific Reports*, vol. 7, no. 1, article 14377, 2017.

[9] U. A. Gurkan and O. Akkus, "The mechanical environment of bone marrow: A review," *Annals of Biomedical Engineering*, vol. 36, no. 12, pp. 1978–1991, 2008.

[10] X. Chen, F. He, D.-Y. Zhong, and Z.-P. Luo, "Acoustic-frequency vibratory stimulation regulates the balance between osteogenesis and adipogenesis of human bone marrow-derived mesenchymal stem cells," *BioMed Research International*, vol. 2015, Article ID 540731, 10 pages, 2015.

[11] L. Demiray and E. Özçivici, "Bone marrow stem cells adapt to low-magnitude vibrations by altering their cytoskeleton during quiescence and osteogenesis," *Turkish Journal of Biology*, vol. 39, no. 1, pp. 88–97, 2015.

[12] E. Lau, W. D. Lee, J. Li et al., "Effect of low-magnitude, high-frequency vibration on osteogenic differentiation of rat mesenchymal stromal cells," *Journal of Orthopaedic Research*, vol. 29, no. 7, pp. 1075–1080, 2011.

[13] I. S. Kim, Y. M. Song, B. Lee, and S. J. Hwang, "Human mesenchymal stromal cells are mechanosensitive to vibration stimuli," *Journal of Dental Research*, vol. 91, no. 12, pp. 1135–1140, 2012.

[14] J. Edwards and G. C. Reilly, "Low magnitude, high frequency vibration modulates mesenchymal progenitor differentiation," *Journal of Orthopaedic Research*, vol. 36, article 2186, 2011.

[15] B. Sen, Z.-H. Xie, N. Case, M. Styner, C. T. Rubin, and J. Rubin, "Mechanical signal influence on mesenchymal stem cell fate is enhanced by incorporation of refractory periods into the loading regimen," *Journal of Biomechanics*, vol. 44, no. 4, pp. 593–599, 2011.

[16] Z. Tong, R. L. Duncan, and X. Jia, "Modulating the behaviors of mesenchymal stem cells via the combination of high-frequency vibratory stimulations and fibrous scaffolds," *Tissue Engineering Part: A*, vol. 19, no. 15-16, pp. 1862–1878, 2013.

[17] Y. Zhou, X. Guan, Z. Zhu et al., "Osteogenic differentiation of bone marrow-derived mesenchymal stromal cells on bone-derived scaffolds: effect of microvibration and role of ERK1/2 activation," *European Cells and Materials*, vol. 22, pp. 12–25, 2011.

[18] S. Mehta, "Hydrogel encapsulation of cells mimics the whole body response to LMHF vibrations," Available from Dissertations & Theses @ Rutgers University; ProQuest Dissertations & Theses Global, 2015.

[19] M.-M. Khani, M. Tafazzoli-Shadpour, Z. Goli-Malekabadi, and N. Haghighipour, "Mechanical characterization of human mesenchymal stem cells subjected to cyclic uniaxial strain and TGF-β1," *Journal of the Mechanical Behavior of Biomedical Materials*, vol. 43, pp. 18–25, 2015.

[20] J. S. Park, J. S. F. Chu, C. Cheng, F. Chen, D. Chen, and S. Li, "Differential effects of equiaxial and uniaxial strain on mesenchymal stem cells," *Biotechnology and Bioengineering*, vol. 88, no. 3, pp. 359–368, 2004.

[21] Y. J. Chen, C. H. Huang, I. C. Lee, Y. T. Lee, M. H. Chen, and T. H. Young, "Effects of cyclic mechanical stretching on the mRNA expression of tendon/ ligament-related and osteoblast-specific genes in human mesenchymal stem cells," *Connective Tissue Research*, vol. 49, no. 1, pp. 7–14, 2008.

[22] M. Koike, H. Shimokawa, Z. Kanno, K. Ohya, and K. Soma, "Effects of mechanical strain on proliferation and differentiation of bone marrow stromal cell line ST2," *Journal of Bone and Mineral Metabolism*, vol. 23, no. 3, pp. 219–225, 2005.

[23] L. Zhang, X. Wang, H. Chen, and N. Tran, "Cyclic stretching and co-culture with fibroblasts promote the differentiation of rat mesenchymal stem cells to ligament fibroblasts," *Journal of Biomechanics*, vol. 39, pp. S579–S580, 2006.

[24] Y. Huang, L. Zheng, X. Gong et al., "Effect of cyclic strain on cardiomyogenic differentiation of rat bone marrow derived mesenchymal stem cells," *PLoS ONE*, vol. 7, no. 4, Article ID e34960, 2012.

[25] R. D. Sumanasinghe, S. H. Bernacki, and E. G. Loboa, "Osteogenic differentiation of human mesenchymal stem cells in collagen matrices: Effect of uniaxial cyclic tensile strain on bone morphogenetic protein (BMP-2) mRNA expression," *Tissue Engineering Part A*, vol. 12, no. 12, pp. 3459–3465, 2006.

[26] R. D. Sumanasinghe, T. W. Pfeiler, N. A. Monteiro-Riviere, and E. G. Loboa, "Expression of proinflammatory cytokines by human Mesenchymal stem cells in response to cyclic tensile strain," *Journal of Cellular Physiology*, vol. 219, no. 1, pp. 77–83, 2009.

[27] Y. Qiu, J. Lei, T. J. Koob, and J. S. Temenoff, "Cyclic tension promotes fibroblastic differentiation of human MSCs cultured on collagen-fibre scaffolds," *Journal of Tissue Engineering and Regenerative Medicine*, vol. 10, no. 12, pp. 989–999, 2016.

[28] N. Juncosa-Melvin, K. S. Matlin, R. W. Holdcraft, V. S. Nirmalanandhan, and D. L. Butler, "Mechanical stimulation increases collagen type I and collagen type III gene expression of stem cell-collagen sponge constructs for patellar tendon repair," *Tissue Engineering Part A*, vol. 13, no. 6, pp. 1219–1226, 2007.

[29] S. R. Rathbone, J. R. Glossop, J. E. Gough, and S. H. Cartmell, "Cyclic tensile strain upon human mesenchymal stem cells in 2D and 3D culture differentially influences CCNL2, WDR61 and BAHCC1 gene expression levels," *Journal of the Mechanical Behavior of Biomedical Materials*, vol. 11, pp. 82–91, 2012.

[30] L. Kreja, A. Liedert, H. Schlenker et al., "Effects of mechanical strain on human mesenchymal stem cells and ligament fibroblasts in a textured poly(L-lactide) scaffold for ligament tissue engineering," *Journal of Materials Science: Materials in Medicine*, vol. 23, no. 10, pp. 2575–2582, 2012.

[31] P. J. Yang, M. E. Levenston, and J. S. Temenoff, "Modulation of mesenchymal stem cell shape in enzyme-sensitive hydrogels is decoupled from upregulation of fibroblast markers under cyclic tension," *Tissue Engineering Part A*, vol. 18, no. 21-22, pp. 2365–2375, 2012.

[32] D. M. Doroski, M. E. Levenston, and J. S. Temenoff, "Cyclic tensile culture promotes fibroblastic differentiation of marrow stromal cells encapsulated in poly(ethylene glycol)-based hydrogels," *Tissue Engineering Part A*, vol. 16, no. 11, pp. 3457–3466, 2010.

[33] C. Snow-Harter, M. L. Bouxsein, B. T. Lewis, D. R. Carter, and R. Marcus, "Effects of resistance and endurance exercise on bone mineral status of young women: A randomized exercise intervention trial," *Journal of Bone and Mineral Research*, vol. 7, no. 7, pp. 761–769, 1992.

[34] D. R. Taaffe, T. L. Robinson, C. M. Snow, and R. Marcus, "High-impact exercise promotes bone gain in well-trained female athletes," *Journal of Bone and Mineral Research*, vol. 12, no. 2, pp. 255–260, 1997.

[35] C. T. Rubin, R. Recker, D. Cullen, J. Ryaby, J. McCabe, and K. McLeod, "Prevention of postmenopausal bone loss by a low-magnitude, high-frequency mechanical stimuli: a clinical trial assessing compliance, efficacy, and safety," *Journal of Bone and Mineral Research*, vol. 19, no. 3, pp. 343–351, 2004.

[36] H. Merriman and K. Jackson, "The effects of whole-body vibration training in aging adults: A systematic review," *Journal of Geriatric Physical Therapy*, vol. 32, no. 3, pp. 134–145, 2009.

[37] H. Seidel and R. Heide, "Long-term effects of whole-body vibration: a critical survey of the literature," *International Archives of Occupational and Environmental Health*, vol. 58, no. 1, pp. 1–26, 1986.

[38] M. Cardinale and J. Rittweger, "Vibration exercise makes your muscles and bones stronger: Fact or fiction?" *British Menopause Society*, vol. 12, no. 1, pp. 12–18, 2006.

[39] J. Wang, K. Leung, S. Chow, and W. Cheung, "The effect of whole body vibration on fracture healing – a systematic review," *European Cells and Materials*, vol. 34, pp. 108–127, 2017.

[40] F. Tian, Y. Wang, and D. D. Bikle, "IGF-1 signaling mediated cell-specific skeletal mechano-transduction," *Journal of Orthopaedic Research*, 2017.

[41] P. G. Childs, C. A. Boyle, G. D. Pemberton et al., "Use of nanoscale mechanical stimulation for control and manipulation of cell behaviour," *Acta Biomaterialia*, vol. 34, pp. 159–168, 2016.

[42] S. Judex, X. Lei, D. Han, and C. Rubin, "Low-magnitude mechanical signals that stimulate bone formation in the ovariectomized rat are dependent on the applied frequency but not on the strain magnitude," *Journal of Biomechanics*, vol. 40, no. 6, pp. 1333–1339, 2007.

[43] S. J. Hwang, Y. M. Song, T. H. Cho et al., "The implications of the response of human mesenchymal stromal cells in three-dimensional culture to electrical stimulation for tissue regeneration," *Tissue Engineering Part: A*, vol. 18, no. 3-4, pp. 432–445, 2012.

[44] M. Kabiri, B. Kul, W. B. Lott et al., "3D mesenchymal stem/stromal cell osteogenesis and autocrine signalling," *Biochemical and Biophysical Research Communications*, vol. 419, no. 2, pp. 142–147, 2012.

[45] E. Cukierman, R. Pankov, and K. M. Yamada, "Cell interactions with three-dimensional matrices," *Current Opinion in Cell Biology*, vol. 14, no. 5, pp. 633–639, 2002.

[46] J. A. Pedersen and M. A. Swartz, "Mechanobiology in the third dimension," *Annals of Biomedical Engineering*, vol. 33, no. 11, pp. 1469–1490, 2005.

[47] A. Bartholomew, C. Sturgeon, M. Siatskas et al., "Mesenchymal stem cells suppress lymphocyte proliferation in vitro and prolong skin graft survival in vivo," *Experimental Hematology*, vol. 30, no. 1, pp. 42–48, 2002.

[48] J. M. Gimble, F. Guilak, M. E. Nuttall, S. Sathishkumar, M. Vidal, and B. A. Bunnell, "*In vitro* differentiation potential of mesenchymal stem cells," *Transfusion Medicine and Hemotherapy*, vol. 35, no. 3, pp. 228–238, 2008.

[49] M. Vanleene and S. J. Shefelbine, "Therapeutic impact of low amplitude high frequency whole body vibrations on the osteogenesis imperfecta mouse bone," *Bone*, vol. 53, no. 2, pp. 507–514, 2013.

[50] H.-F. Shi, W.-H. Cheung, L. Qin, A. H.-C. Leung, and K.-S. Leung, "Low-magnitude high-frequency vibration treatment augments fracture healing in ovariectomy-induced osteoporotic bone," *Bone*, vol. 46, no. 5, pp. 1299–1305, 2010.

[51] J. H. Edwards, "Vibration stimuli and the differentiation of musculoskeletal progenitor cells: Review of results," *World Journal of Stem Cells*, vol. 7, no. 3, pp. 568–582, 2015.

[52] J. Starke, K. Maaser, B. Wehrle-Haller, and P. Friedl, "Mechanotransduction of mesenchymal melanoma cell invasion into 3D collagen lattices: Filopod-mediated extension-relaxation cycles and force anisotropy," *Experimental Cell Research*, vol. 319, no. 16, pp. 2424–2433, 2013.

[53] F. Pampaloni, E. G. Reynaud, and E. H. K. Stelzer, "The third dimension bridges the gap between cell culture and live tissue," *Nature Reviews Molecular Cell Biology*, vol. 8, no. 10, pp. 839–845, 2007.

[54] J. Tan, X. Xu, Z. Tong et al., "Decreased osteogenesis of adult mesenchymal stem cells by reactive oxygen species under cyclic stretch: a possible mechanism of age related osteoporosis," *Bone Research*, vol. 3, article 15003, 2015.

[55] M. Jagodzinski, M. Drescher, J. Zeichen et al., "Effects of cyclic longitudinal mechanical strain and dexamethasone on osteogenic differentiation of human bone marrow stromal cells," *European Cells and Materials*, vol. 7, pp. 35–41, 2004.

[56] A. Charoenpanich, M. E. Wall, C. J. Tucker, D. M. K. Andrews, D. S. Lalush, and E. G. Loboa, "Microarray analysis of human adipose-derived stem cells in three-dimensional collagen culture: osteogenesis inhibits bone morphogenic protein and wnt signaling pathways, and cyclic tensile strain causes upregulation of proinflammatory cytokine regulators and angiogenic factors," *Tissue Engineering Part A*, vol. 17, no. 21-22, pp. 2615–2627, 2011.

[57] E. Donzelli, A. Salvadè, P. Mimo et al., "Mesenchymal stem cells cultured on a collagen scaffold: In vitro osteogenic differentiation," *Archives of Oral Biolog*, vol. 52, no. 1, pp. 64–73, 2007.

[58] G. Papavasiliou, S. Sokic, and M. Turturro, "Synthetic PEG hydrogels as extracellular matrix mimics for tissue engineering applications," in *Biotechnology Molecular Studies and Novel Applications for Improved Quality of Human Life*, 2012.

Hindawi
International Journal of Biomaterials
Volume 2017, Article ID 8074890, 9 pages
https://doi.org/10.1155/2017/8074890

Research Article

Application of Synthetic Polymeric Scaffolds in Breast Cancer 3D Tissue Cultures and Animal Tumor Models

Girdhari Rijal, Chandra Bathula, and Weimin Li

Department of Biomedical Sciences, Elson S. Floyd College of Medicine, Washington State University, Spokane, WA 99210, USA

Correspondence should be addressed to Weimin Li; weimin.li@wsu.edu

Received 23 October 2017; Accepted 22 November 2017; Published 17 December 2017

Academic Editor: Jie Deng

Copyright © 2017 Girdhari Rijal et al. This is an open access article distributed under the Creative Commons Attribution License, which permits unrestricted use, distribution, and reproduction in any medium, provided the original work is properly cited.

Preparation of three-dimensional (3D) porous scaffolds from synthetic polymers is a challenge to most laboratories conducting biomedical research. Here, we present a handy and cost-effective method to fabricate polymeric hydrogel and porous scaffolds using poly(lactic-co-glycolic) acid (PLGA) or polycaprolactone (PCL). Breast cancer cells grown on 3D polymeric scaffolds exhibited distinct survival, morphology, and proliferation compared to those on 2D polymeric surfaces. Mammary epithelial cells cultured on PLGA- or PCL-coated slides expressed extracellular matrix (ECM) proteins and their receptors. Estrogen receptor- (ER-) positive T47D breast cancer cells are less sensitive to 4-hydroxytamoxifen (4-HT) treatment when cultured on the 3D porous scaffolds than in 2D cultures. Finally, cancer cell-laden polymeric scaffolds support consistent tumor formation in animals and biomarker expression as seen in human native tumors. Our data suggest that the porous synthetic polymer scaffolds satisfy the basic requirements for 3D tissue cultures both *in vitro* and *in vivo*. The scaffolding technology has appealing potentials to be applied in anticancer drug screening for a better control of the progression of human cancers.

1. Introduction

2D *in vitro* cell culture models have been instrumental in addressing various questions and providing invaluable knowledge in the field of cancer cell biology for decades. With the advancement of research technologies, some of the drawbacks of 2D cell culture models have been identified that include the lack of cell-ECM interactions and differences in cell morphology, proliferation rate, viability, polarity, motility, differentiation, and sensitivity to therapeutics compared to the characteristics of cells *in vivo* [1–6]. These limitations of 2D culture systems have become hindrance to the progress of our understanding of the mechanisms of cancer initiation and progression and of developing therapeutic approaches to treat human cancers, highlighting the needs for better culture platforms that are able to closely mimic tissue environments where native cancer cells live.

With the integration of the spatial concept, various 3D cell culture systems have been developed to overcome the limitations of 2D cultures. There is a remarkable increase in the use of 3D cultures over the past 10 years [7], resulting in many interesting findings that are distinct from the effects seen in the traditional 2D cultures. For instance, cells grown in 3D cultures display changes in metabolic characteristics, such as increased glycolysis [8], in gene expression patterns, such as upregulation of VEGF and angiopoietin genes involved in angiogenesis [9–11], and in production of chemokines, such as interleukin-8 [12], compared to cells grown on 2D surfaces. It is noteworthy that genome wide gene expression analysis comparing gene expression patterns of U87 cells grown in 2D and 3D cultures with a cohort of 53 pediatric high grade gliomas revealed significant similarities between the 3D, but not the 2D, culture samples and the human brain tumors [13]. Moreover, several studies have shown increased chemoresistance of cancer cells grown in 3D systems compared to the cells in 2D cultures [14–16], recapitulating the responses of cancer cells to chemotherapeutics *in vivo*. Depending on scientific questions to be addressed and specific experimental design, 3D scaffolds applied in biomedical research are predominantly fabricated using either natural materials, such as native tissue proteins and algae, or synthetic polymers, such as PLGA, PCL, and poly(ethylene glycol) (PEG) [7, 17, 18]. The advantages of synthetic polymeric scaffolds are their abundant availability, low cost, suitability for large-scale

3D bioprinting and reconstruction of certain tissue structures, and flexibility to be tailored to meet specific physical requirements of different culture systems [19–24].

In this study, we focused on characterizing the efficacies of applying the synthetic polymer scaffolds fabricated using PLGA and PCL with a modified gas foaming approach for 3D tissue cultures and animal models in breast cancer research. The viability, morphology, proliferation, and receptor expression of breast cancer cells as well as their responses to anticancer drug and development into tumors in animals with the support of the 3D scaffolds were investigated.

2. Materials and Methods

2.1. Polymer Coating on Slides. Microscopic glass slides were cleaned with 70% ethanol, air-dried in a biological safety cabinet, coated with 2% of PCL (Sigma-Aldrich), PLGA (Sigma-Aldrich), or PCL and PLGA (1 : 1 ratio) dissolved in chloroform (Sigma-Aldrich) for 1 hour, air-dried in a biological safety cabinet, and rinsed twice with 1x PBS before cell seeding.

2.2. 3D Porous Scaffold Fabrication from Polymer. To fabricate porous scaffolds with similar pore sizes as decellularized mouse breast tissues (~100 μm) [16], 1.0 gram of PLGA or 0.5 gram of PCL was dissolved in 1 ml of chloroform followed by adding 1 gram of sodium bicarbonate ($NaHCO_3$, Sigma-Aldrich) into the solution. The solutions were slowly dispensed into the semispherical molds (4 mm in diameter) built in porcelain panels, which were kept in −80°C freezer for 1-2 hours and freeze-dried at −50°C for 48 hours as described previously [16]. The scaffolds were then washed in 0.1 N hydrochloric acid (HCl) solution for 6 hours (replacing the solution hourly) at room temperature to generate the pores after releasing CO_2 produced by the $NaHCO_3$ and HCl reactions from the scaffolds, followed by washing in distilled water for several times until the pH of the water became neutral. The scaffolds were soaked in 70% ethanol for 3–5 hours, washed three times in 1x PBS for 10 minutes, and kept in 1x PBS until use. The generation of PCL and PLGA combined scaffolds was achieved by mixing equal volume (1 : 1 ratio) of PCL and PLGA solutions and following the same procedures as described above.

2.3. In Vitro 2D and 3D Cultures. MCF10A cells (American Type Culture Collection, ATCC) were maintained in 1x DMEM/F12 50/50 (Mediatech) supplemented with 10 μg/ml insulin, 20 ng/ml EGF, 0.5 μg/ml hydrocortisone, 100 ng/ml cholera toxin, 5% horse serum, and 1% Penicillin-Streptomycin. MDA-MB-231 cells (ATCC) were maintained in 1x DMEM (Mediatech) supplemented with 10% FBS and 1% Penicillin-Streptomycin. The polymer-coated slides (circular, 12 mm in diameter; ThermoFisher Scientific) or the scaffolds were placed in 24-well or 96-well plates, washed several times with sterile 1x PBS, and preconditioned with culture medium. MCF10A or MDA-MB-231 cells suspended in the respective culture medium were seeded on the slides or scaffolds (1×10^5 per slide or scaffold) and allowed to attach to the matrices for 45 minutes. The cells were then cultured in the medium under optimal conditions (37°C, 5% CO_2) and collected at indicated time points, analyzed, or used in downstream experiments. For longer period of culturing time, the culture medium was replenished every other day.

2.4. Live and Dead Cell Assay. The cell cultures on the polymer-coated slides or polymer scaffolds were briefly washed with 1x PBS (37°C) twice and incubated in the Live/Dead Cell Staining solution (2 μM of calcein-AM and 4 μM of EhtD-III in 1x PBS, PromoKine) at room temperature for 30 minutes. Images were captured using epifluorescence microscopy (Zeiss Axio Imager M2). Live cells take the calcein-AM stain and fluorescence green under EGFP filter, while dead cells take the EthD-III stain and fluorescence red under Texas Red filter.

2.5. Proliferation Assay. The proliferation of the cells grown on the coated slides and scaffolds was measured using the CCK-8 reagent (Sigma-Aldrich) at the time points indicated. Briefly, CCK-8 solution was added at a 1 : 10 dilution into the cultures and incubated (37°C, 5% CO_2) for 3 hours. The supernatants of the cultures were collected and the colorimetric reactions within the supernatants that reflect the proliferation status were measured using a Synergy 2 microplate reader (BioTek) for the absorbance at 490 nm. Error bars represent standard deviations (SD) of the means of three independent experiments.

2.6. Cell Surface Receptor Expression. The cells cultured on the polymer-coated slides at about 80% confluency were washed with cold 1x PBS twice and fixed in 4% cold paraformaldehyde. Immunofluorescence staining was performed as previously described [25] using primary antibodies against integrin-α2 (mouse, Santa Cruz Biotechnology, sc-74466) and collagen type 1 (rabbit, Abcam, ab34710) as set 1 as well as integrin α6 (rabbit, Invitrogen, 710201) and laminin-β3 (mouse, Santa Cruz Biotechnology, sc-33178) as set 2 along with Alexa Fluor® dye-conjugated anti-rabbit and anti-mouse (Thermo Fisher Scientific) secondary antibodies to detect the expression of the integrin receptors on the surface of the cells in response to the polymer matrices.

2.7. Response of Cells to Anticancer Drug. T47D breast cancer cells (ATCC, 1×10^5 cells per scaffold) were seeded on the 3D scaffolds and cultured in 96-well plates for 7 days. (Z)-4-Hydroxytamoxifen (4-HT, Abcam, ab1419430) at the final concentration of 1 μM was administered in alternate days from 7th to 14th day of culture. Cell survival experiment was performed using the Live/Dead assay as described above. Triplicate independent experiments were performed for statistical significance.

2.8. In Vivo Tumor Formation. MDA-MB-231 cells (1×10^5 cells/scaffold) were seeded on spherical porous PLGA scaffolds (4 mm-diameter) and cultured under optimal conditions (37°C, 5% CO_2) for 24 hours prior to implantation. The blank (without cells as negative controls) and cell-laden scaffolds were implanted into the right and the left 4th inguinal mammary fat pads, respectively, of 8-week-old

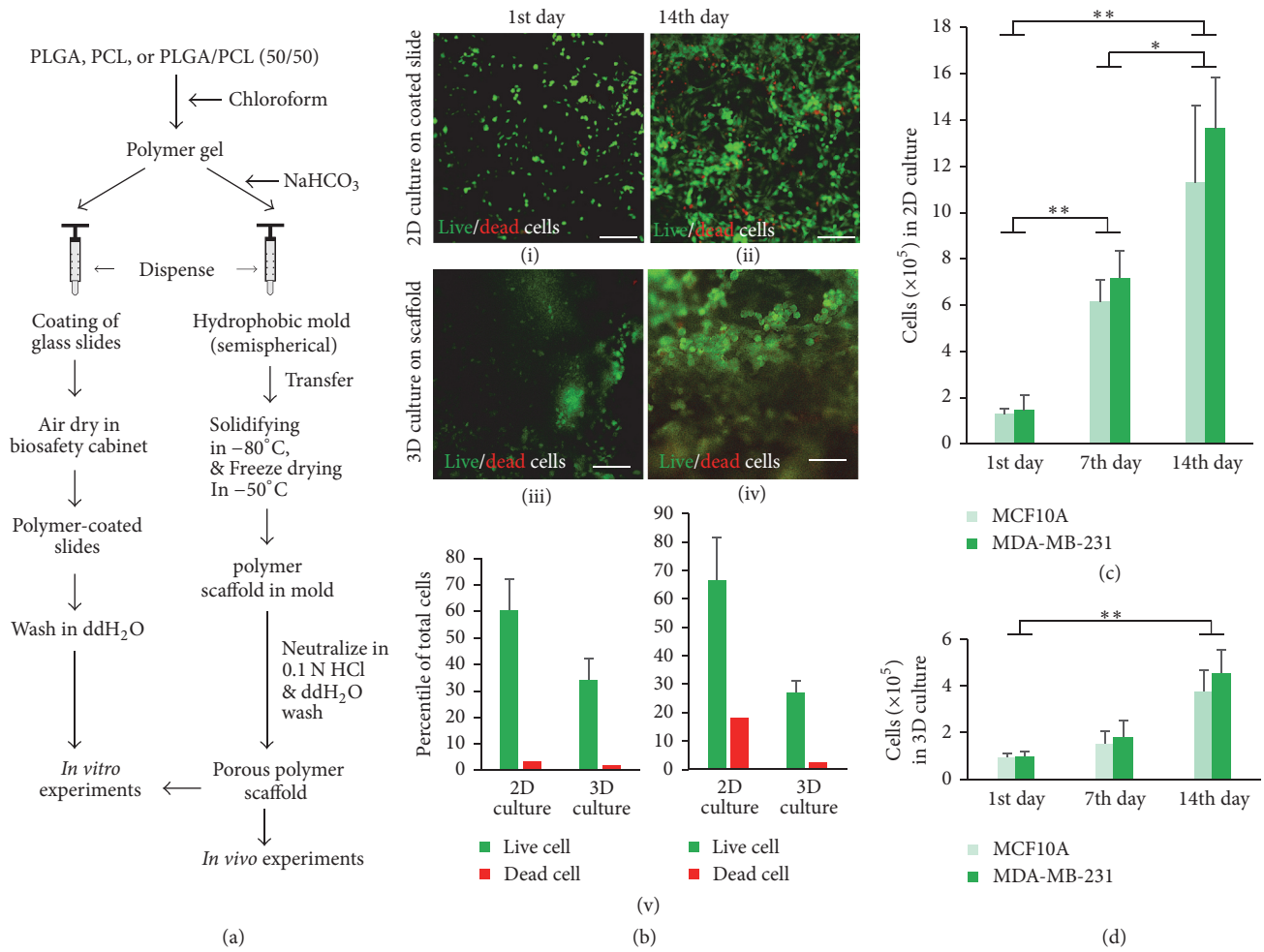

FIGURE 1: *Cell survival, morphology, and growth status on polymeric scaffolds.* (a) Main procedures of preparing PLGA-coated slides and 3D porous PLGA scaffolds. (b) Examination of MDA-MB-231 cell survival on PLGA-coated slides ((b)(i) and (b)(ii)) and porous PLGA scaffolds ((b)(iii) and (b)(iv)) using live and dead assays. Scale bars, 100 μm. The number of live and dead cells in the 2D and 3D cultures were quantified in ((b)(v)). (c) Proliferation rate of MCF10A and MDA-MB-231 cells on PLGA-coated slides. (d) Proliferation rate of MCF10A and MDA-MB-231 cells on porous PLGA scaffolds. $^{*}p < 0.05$, $^{**}p < 0.01$.

female NOD-SCID mice (Charles River Laboratories). Each implantation condition had six replicates. The growth of the tumors was monitored using spectrum computed tomography (CT) on an *in vivo* imaging system (IVIS, PerkinElmer). The tumors were collected into ice-cold 4% paraformaldehyde 4 weeks after implantation, paraffin embedded, cross-sectioned, antigen retrieved (1 mM EDTA solution, 10 mM Tris Base, and 0.05% Tween 20; pH 9.0), and stained with HER2 (rabbit, Cell Signaling Technology, 2165) and Ki-67 (mouse, Cell Signaling Technology, 9449) primary antibodies followed by Alexa fluorophore-conjugated secondary antibodies. Images were captured using fluorescence microscopy as described before [25].

2.9. Statistical Analysis. One-way ANOVA was performed using the StatPlus (Build 6.0.0/Core v5.9.92, AnalystSoft) software to analyze the statistical data. Error bars represent standard error of the mean (SEM) of three independent experiments unless otherwise indicated.

3. Results and Discussion

3.1. Cell Survival, Morphology, and Proliferation on the Polymeric Scaffolds. To examine the survival of cancer cells grown on the polymeric substrata, human triple (ER, PR, and HER2 receptor) negative breast cancer MDA-MB-231 cells were cultured on PLGA-coated microscopic glass slides (2D) and porous PLGA scaffolds (3D), respectively, as described in the methods and illustrated in Figure 1(a) for 14 days. The Day 1 and Day 14 culture samples were collected and stained with the Live/Dead Cell assay kit as described in the methods. This staining method labels live cells in green color and the dead cells in red color when observing the cells under fluorescence microscope. Our results showed that the number of dead cells detected on PLGA-coated glass slides (Figures 1(b)(i) and 1(b)(v)) or on PLGA 3D scaffolds (Figures 1(b)(iii) and 1(b)(v)) were negligible on Day 1. However, the number of dead cells detected on the PLGA-coated glass slides was markedly higher (Figures 1(b)(ii) and 1(b)(v)) than those on

the 3D PLGA porous scaffolds (Figures 1(b)(iv) and 1(b)(v)) on Day 14. The reason for increased cell death in the 2D cultures could be due to the faster proliferation rate of MDA-MB-231 cells on flat surface compared to that of the cells on 3D scaffolds, consistent with the previous observations where other scaffolding materials were used in 3D cell cultures [16, 26]. Because of the nature of the staining and imaging method, some of the cells grown on 3D scaffolds appeared to be out of focus due to the growth of cells at different focal planes/depths of the 3D scaffolds (Figure 1(b)(iii) and 1(b)(iv)).

We next inspected the morphological differences between cancer cells grown on polymeric 2D surfaces and those on polymeric 3D scaffolds. The results showed that the MDA-MB-231 cells grown on the 2D PLGA surfaces were in spindle shapes and populated the surface areas in a more or less universal way (Figure 1(b)(ii)) while those cultured on the 3D PLGA scaffolds exhibited round shapes and expand as cell clusters (Figure 1(b)(iv)). These data are consistent with previous studies that showed distinct morphological features of cells grown on 3D scaffolds compared to those of cells gown on 2D cultures [27–29]. The morphological differences between the two types of cultures could be the results of two factors. One is the distinct physical features of the surfaces of the 2D flat and 3D porous scaffolds, with the former being smooth and even and the latter being rough and uneven because of the existing pores on the surfaces of the scaffolds. The other is the spatial interactions between the neighboring cells and between the cells and the substrata, with the 2D interactions being "bidirectional" at lateral and basal surfaces of the cells and the 3D interactions being "multidirectional" at most or all of the surfaces of the cells. The multidirectional interaction feature of the 3D cell cultures resembles the characteristics of the closed environment of native tissues, where the living cells attach to and interact with the surrounding matrices or/and other cells at all directions. Moreover, even though cancer cells grown in 2D culture can grow on top of each other when the cell population reaches confluency, they hardly form tumoroids as can be commonly achieved in 3D cultures. Therefore, the morphological properties of cancer cells within 3D microenvironments could be a fundamental factor contributing to cancer cell growth, motility, tumor development, and resistance to therapeutic drugs.

Cancer cell proliferation after adapting the living environment is essential for tumor growth. To assess the support of PLGA in cell proliferation both in 2D and in 3D cultures, MCF10A and MDA-MB-231 cells were grown on the PLGA-coated glass slides and the porous PLGA scaffolds for 14 days. Cell proliferation rates were measured using CCK-8 reagent on Day 1, Day 7, and Day 14 of culture. The results showed that MCF10A and MDA-MB-231 cells grown on the PLGA-coated glass slides proliferated rapidly during the culturing time (Figure 1(c)). Though a similar trend was observed in the 3D cultures, the proliferation rate of the cells was substantially lower than that of the 2D cultures (Figures 1(c) and 1(d)). In addition, the proliferation rate of MDA-MB-231 cells is slightly higher than that of MCF10A cells in both 2D and 3D cultures (Figures 1(c) and 1(d)). A similar discrepancy in cell proliferation between 2D and 3D cultures was observed in our previous studies using native tissue ECM as scaffolding materials [16] and in studies using other materials [22, 30]. However, increased proliferation rate was observed in JIMT1 breast cancer cells grown on Matrigel compared to regular 2D cultures [31], suggesting a cell type- or/and culture system-related phenotype that should be taken into account for different experimental purposes. Overall, the proliferation rates of cell lines displayed in 3D culture models resemble those of tumor models *in vivo*.

3.2. Surface Receptor Expression of the Cells on Polymeric Scaffolds. Type I collagen is one of the major components of breast tissue ECM [16] and integrin $\alpha 2\beta 1$ is a primary receptor for type I collagen [32]. To investigate whether the synthetic polymers support the expression of ECM proteins and cell surface receptors, MCF-10A and MDA-MB-231 cells were cultured on the PLGA-coated slides for 24 hours, fixed with 4% paraformaldehyde, and stained with antibodies against type I collagen and integrin $\alpha 2$ as described previously [25]. Immunofluorescence (IF) microscopy detected strong staining signals of type I collagen and integrin $\alpha 2$ in both MCF10A and MDA-MB-231 cells (Figures 2(b), 2(c), 2(f), and 2(g)). Although the MDA-MB-231 cells appeared to be a bit smaller than the MCF10A cells on the PLGA-coated slides, the overall expression of type I collagen and integrin $\alpha 2$ in the cancer cells is lower than in the normal MCF10A cells (Figures 2(b)–2(d) and 2(f)–2(h)). These data are consistent with a previous report of lower integrin $\alpha 2$ (ITGA2) expression in primary breast cancers compared to normal breast tissues [33]. In addition, basal level expression of integrin $\alpha 2\beta 1$ may favor breast cancer cell migration and tumor growth [34, 35] since high levels of the integrin receptor inhibit cancer cell migration [36]. We observed a nice colocalization of integrin $\alpha 2$ receptors with type I collagen in the cells especially around the edges of the cells, implicating local deposition of type I collagen on the slide surface and the binding of integrin $\alpha 2$ receptors to the deposited collagen for the attachment and migration of the cells. Similarly, we examined the expression levels of type I collagen and integrin $\alpha 2$ in MCF10A and MDA-MB-231 cells grown on PCL- or PLGA/PCL- (50/50) coated slides, and the results were coherent with those seen on the PLGA substratum (data not shown). Moreover, we did not notice significant differences in the morphology, viability, and cell proliferation of the cells grown on PLGA, PCL, or 3D PLGA/PCL (50/50) surfaces (data not shown). These data suggest that the synthetic polymeric surfaces or scaffolds could be used to study certain aspects of cancer biology. However, care needs to be taken into account in terms of the choices of different types of synthetic materials and fabrication methods to make 3D scaffolds for either biomedical or bioengineering applications owing to different advantages and limitations of the respective approaches compared to some biomaterial-based model systems [7].

3.3. Response of Cells Grown on the Polymeric Scaffold to Drugs. Traditionally, the efficacies of anticancer prodrugs were initially tested in 2D cell culture systems, and the promising drug candidates from these studies were further evaluated in animal experiments before entering clinical

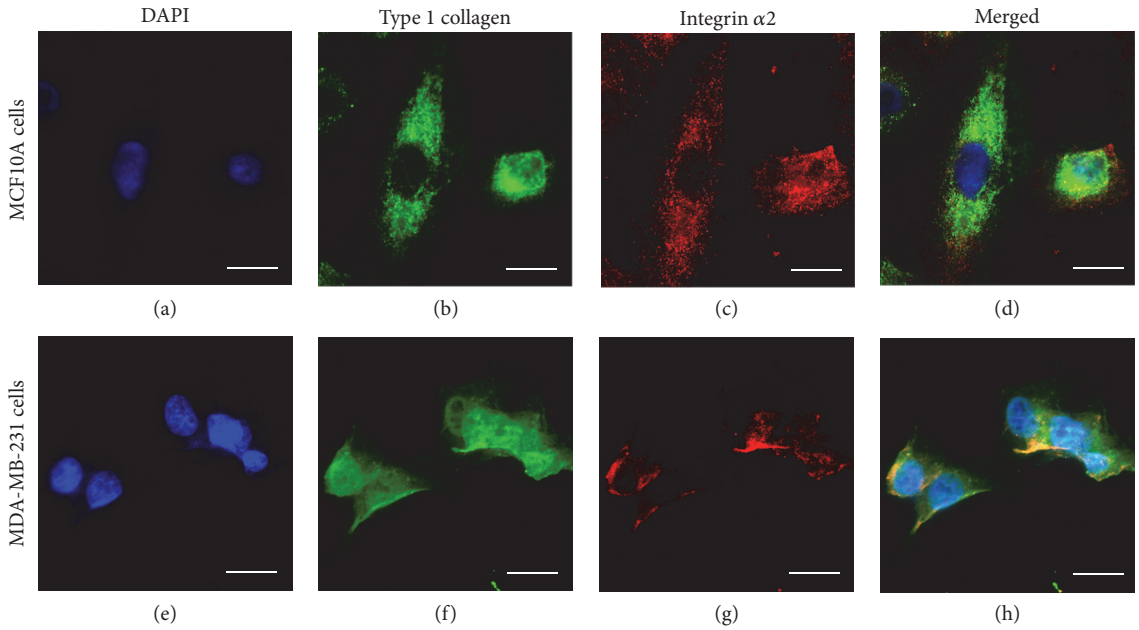

Figure 2: *Type I collagen and integrin 2 receptor expression in breast epithelial cells cultured on PLGA-coated surfaces*. The expression and deposition of type I collagen (green) as well as its cell surface receptor integrin $\alpha 2$ (red) expression was inspected in MCF10A and MDA-MB-231 cells grown on the PLGA-coated glass slides using IF staining couple with confocal microscopy. The nuclei of the cells were stained with DAPI (Blue). Scale bars, 10 μm.

trials. However, the majority of drug candidates that were efficacious in 2D cultures failed in animal studies or clinical trials. One of the main reasons attributed to these drug testing failures is the inability of 2D culture systems to mimic the natural tissue microenvironment for cells living in them behave as they would be in native tissues. There is increasing evidence supporting 3D tissue cultures as better models to test efficacies of drug candidates [7].

In this study, we examined the effect of 4-hydroxytamoxifen (4-HT), an active metabolite of the estrogen receptor (ER) antagonist tamoxifen, on the ER-positive luminal A type of breast cancer T47D cells grown on 3D PLGA scaffolds. The cells were treated with 1 μM 4-HT on alternate days starting on Day 7 through Day 13 after cell seeding on the scaffolds, and the images were taken on Day 8 and Day 14 time points. The viability of the cells was analyzed using live and dead cell assays as described before. In consistency with the drug testing results seen in biomaterial-based 3D tissue culture studies [16] and animal models [37–39], T47D cells grown on 3D PLGA scaffolds were less sensitive to 4-HT than those on PLGA-coated slides (data not shown). T47D cells treated with vehicle solvent only showed increased cell proliferation on Day 14 compared to Day 7 and did not show significant differences in cell viability on Day 7 or Day 14 in cells grown on the 3D scaffolds (Figures 3(a)–3(c) and 3(h)–3(j)). However, the proliferation of T47D cells on the scaffolds was markedly decreased after 4-HT treatment as exhibited in the Day 7 and Day 14 images (Figures 3(d)–3(g) and 3(k)–3(n)). A close to complete cell death was observed in 4-HT-treated samples on Day 14 (Figures 3(k)–3(n)). These data collectively support the notion that cancer cells cultured in 3D environments develop chemoresistance as seen in native tumors and suggest that the polymeric scaffolds can be used as tissue-mimicry environments to study cancer cell responses to therapeutic drugs. The chemoresistance noticed in 3D cultures could be due to the heterogeneous populations of cancer cells and the complex physiochemical properties of the ECM environments deposited by the cells within the 3D structures that affect the permeability of the drugs and overexpression of multidrug resistance proteins [40–42].

3.4. The Polymeric Scaffold Support of Tumor Formation. To assess the capabilities of the polymeric porous scaffolds in supporting tumor formation in mice, porous PLGA scaffolds were coated with MDA-MB-231 cells, cultured for 24 hours, and implanted into mammary fat pads of NOD/SCID mice. Blank scaffolds without cells were used as negative control. Tumor growth was monitored by an *in vivo* imaging system (IVIS) spectrum CT, and tumor sizes were measured with caliper. The tumors were collected 4 weeks after implantation, paraffin embedded, and cross-sectioned for immunohistochemistry (IHC) staining and analyzed with IF microscopy. The animal whole body tomographic images taken at the experimental end point demonstrated that tumor lumps were developed from the cancer cell-laden scaffolds, but not the blank scaffold control groups, during the period of observation (Figures 4(a) and 4(f)). The IF images showed that, by end of week 4 after implantation, the scaffolds were occupied by cells as illustrated by DAPI staining of nuclei of the cells on the cross sections of the samples (Figures 4(b) and 4(g)). As expected, the proliferating cell nuclear antigen biomarker Ki-67 was nondetectable in the blank scaffold

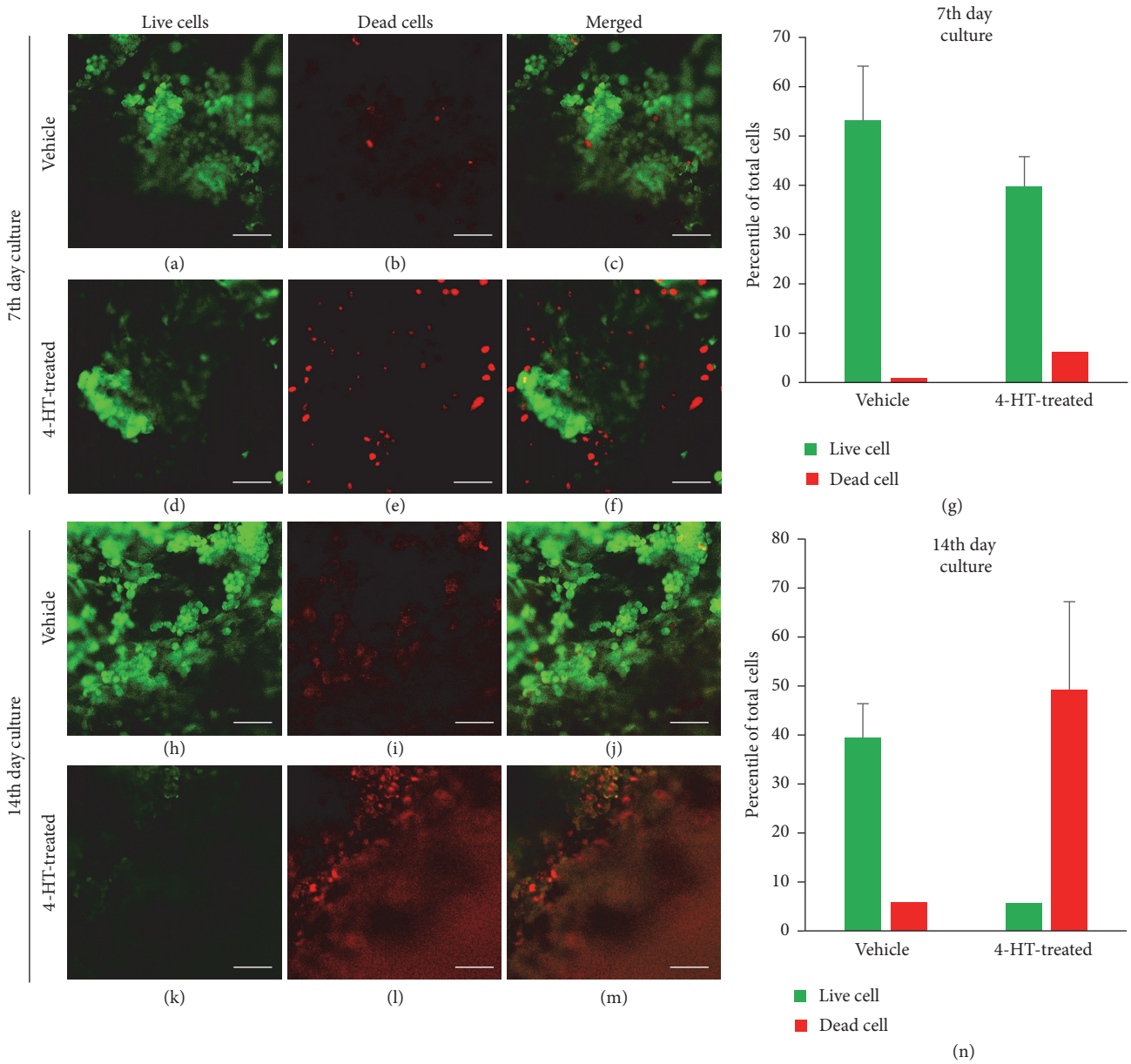

Figure 3: *Sensitivity of cancer cells grown on 3D PLGA scaffolds to anticancer drugs*. MDA-MB-231 cells cultured on the scaffolds for 7 days were treated with 4-HT every other day and examined for cell survival on Day 8 and Day 14, respectively. Live cells were indicated by green signals and dead cells in red signals. Scale bars, 100 μm.

implants and was detected at high levels within the tumors derived from the MDA-MB-231 cell-laden PLGA scaffolds (Figures 4(c) and 4(h)), indicating that fast proliferation of the cancer cell population was established in the scaffolds embedded within the native breast tissues. On the other hand, the HER2 receptors, which were negative in the MDA-MB-231 cells, were detected in some of the stromal cells within the normal and tumor tissues but not in the cancer cells (Figures 4(d) and 4(i)). We did not notice significant differences in tumor sizes when comparing the PLGA scaffold groups with the PCL or PLGA/PCL (50/50) scaffold groups in parallel animal experiments (data not shown). These data support the feasibility of applying the porous polymeric scaffolds in animal tumor model generation with the advantage of consistent tumor formation within reasonable period of time.

4. Conclusions and Remarks

3D cell cultures have overcome many limitations of 2D culture models in cancer biology studies. Our data have added further insights into how the synthetic polymer scaffolds can be successfully used in 3D tissue cultures and in animal tumor models. The phenotypes of the cancer cells we observed in the 3D cultures with regard to survival,

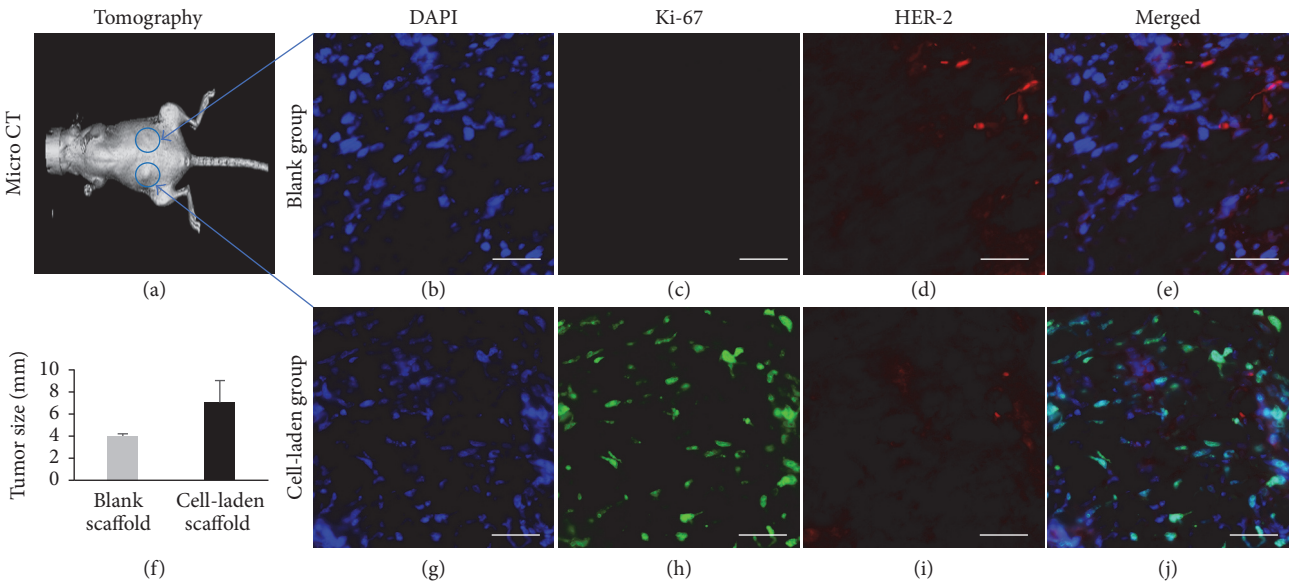

Figure 4: *Support of the polymeric scaffolds for tumor formation in mice.* Blank porous PLGA scaffolds (without MDA-MB-231 cells) and MDA-MB-231 cell-laden PLGA scaffolds were implanted into the mammary fat pads of the mice. Tumor growth were dynamically observed using IVIS during 4 weeks of the period ((a) and (f)). The cross sections of the tumors collected at the end point of the experiments were stained for DAPI (blue, (b) and (g)), Ki-67 (green, (c) and (h)), and HER2 (red, (d) and (i)). Scale bars, 100 μm.

morphology, proliferation, type I collagen and its receptor expression, and response to 4-HT treatment are very encouraging for additional research applications of the system in cancer research. For example, cancer cell migration and interaction with other types of cells within the 3D pores of the scaffolds can be studied. Because of the nonbiological features of the polymeric materials, nucleic acids and proteins can be extracted from the 3D cultures for further analysis without interference from biomolecules derived from native tissues.

Since the conventional tumor generation model, which injects cancer cells into the dorsal subcutaneous or mammary fat pads of animals, has big variations in tumor growth [43–45], our 3D porous scaffold-based animal tumor model can be very useful in consistently generating experimental tumors for both biomedical research and preclinical drug screening. Animal tumors produced using this scaffolding method can facilitate the observations of cancer biomarker expression, molecular regulation of cancer progression, and drug efficacies across tumors at similar sizes and developmental stages. Importantly, this easy and economically inexpensive scaffolding method could be adapted to bioengineering and other relevant fields. However, despite the rapid progress in the development of 3D culture models, there is not a one-for-all 3D system that could recapitulate all the features of native human tumors, and each model has its own advantages and disadvantages. Hence, it is important to select the 3D culture systems that best fit specific research purposes.

Conflicts of Interest

The authors declare that there are no conflicts of interest.

Authors' Contributions

Weimin Li and Girdhari Rijal designed the project. Girdhari Rijal performed the experiments. Girdhari Rijal, Chandra Bathula, and Weimin Li wrote and edited the manuscript.

Acknowledgments

The authors thank the colleagues in the Department of Biomedical Sciences for scientific discussion. They also greatly appreciate the consistent supports from the vivarium staff on the WSU Spokane campus. This project was supported by a WSU Startup Fund to Weimin Li.

References

[1] F. Pampaloni, E. G. Reynaud, and E. H. K. Stelzer, "The third dimension bridges the gap between cell culture and live tissue," *Nature Reviews Molecular Cell Biology*, vol. 8, no. 10, pp. 839–845, 2007.

[2] B. M. Baker and C. S. Chen, "Deconstructing the third dimension: how 3D culture microenvironments alter cellular cues," *Journal of Cell Science*, vol. 125, part 13, pp. 3015–3024, 2012.

[3] J. A. Hickman, R. Graeser, R. de Hoogt et al., "Three-dimensional models of cancer for pharmacology and cancer cell biology: capturing tumor complexity in vitro/ex vivo," *Biotechnology Journal*, vol. 9, no. 9, pp. 1115–1128, 2014.

[4] M. J. Bissell, A. Rizki, and I. S. Mian, "Tissue architecture: The ultimate regulator of breast epithelial function," *Current Opinion in Cell Biology*, vol. 15, no. 6, pp. 753–762, 2003.

[5] T. Mseka, J. R. Bamburg, and L. P. Cramer, "ADF/cofilin family proteins control formation of oriented actin-filament bundles in the cell body to trigger fibroblast polarization," *Journal of Cell Science*, vol. 120, part 24, pp. 4332–4344, 2007.

[6] G. D. Prestwich, "Evaluating drug efficacy and toxicology in three dimensions: using synthetic extracellular matrices in drug discovery," *Accounts of Chemical Research*, vol. 41, no. 1, pp. 139–148, 2008.

[7] G. Rijal and W. Li, "3D scaffolds in breast cancer research," *Biomaterials*, vol. 81, pp. 135–156, 2016.

[8] M. T. Santini, G. Rainaldi, R. Romano et al., "MG-63 human osteosarcoma cells grown in monolayer and as three-dimensional tumor spheroids present a different metabolic profile: a (1)H NMR study," *FEBS Letters*, vol. 557, no. 1–3, pp. 148–154, 2004.

[9] U. Cheema, R. A. Brown, B. Alp, and A. J. MacRobert, "Spatially defined oxygen gradients and vascular endothelial growth factor expression in an engineered 3D cell model," *Cellular and Molecular Life Sciences*, vol. 65, no. 1, pp. 177–186, 2008.

[10] M. Valcarcel, B. Arteta, A. Jaureguibeitia et al., "Three-dimensional growth as multicellular spheroid activates the proangiogenic phenotype of colorectal carcinoma cells via LFA-1-dependent VEGF: implications on hepatic micrometastasis," *Journal of Translational Medicine*, vol. 6, article 57, 2008.

[11] P. A. Kenny, G. Y. Lee, C. A. Myers et al., "The morphologies of breast cancer cell lines in three-dimensional assays correlate with their profiles of gene expression," *Molecular Oncology*, vol. 1, no. 1, pp. 84–96, 2007.

[12] C. Fischbach, J. K. Hyun, S. X. Hsiong, M. B. Evangelista, W. Yuen, and D. J. Mooney, "Cancer cell angiogenic capability is regulated by 3D culture and integrin engagement," *Proceedings of the National Acadamy of Sciences of the United States of America*, vol. 106, no. 2, pp. 399–404, 2009.

[13] S. J. Smith, M. Wilson, J. H. Ward et al., "Recapitulation of Tumor Heterogeneity and Molecular Signatures in a 3D Brain Cancer Model with Decreased Sensitivity to Histone Deacetylase Inhibition," *PLoS ONE*, vol. 7, no. 12, Article ID e52335, 2012.

[14] L. David, V. Dulong, D. Le Cerf, L. Cazin, M. Lamacz, and J.-P. Vannier, "Hyaluronan hydrogel: An appropriate three-dimensional model for evaluation of anticancer drug sensitivity," *Acta Biomaterialia*, vol. 4, no. 2, pp. 256–263, 2008.

[15] J. L. Horning, S. K. Sahoo, S. Vijayaraghavalu et al., "3-D tumor model for in vitro evaluation of anticancer drugs," *Molecular Pharmaceutics*, vol. 5, no. 5, pp. 849–862, 2008.

[16] G. Rijal and W. Li, "A versatile 3D tissue matrix scaffold system for tumor modeling and drug screening," *Science Advances*, vol. 3, no. 9, Article ID e1700764, 16 pages, 2017.

[17] Y. Y. Brahatheeswaran, T. Maekawa, and D. S. Kumar, "Polymeric scaffolds in tissue engineering application: a review," *International Journal of Polymer Science*, vol. 2011, Article ID 290602, pp. 1–19, 2011.

[18] M. S. Shoichet, "Polymer scaffolds for biomaterials applications," *Macromolecules* , vol. 43, no. 2, pp. 581–591, 2009.

[19] G. Rijal, B. S. Kim, F. Pati, D.-H. Ha, S. W. Kim, and D.-W. Cho, "Robust tissue growth and angiogenesis in large-sized scaffold by reducing H_2O_2-mediated oxidative stress," *Biofabrication*, vol. 9, no. 1, Article ID 015013, 2017.

[20] A. Naz, Y. Cui, C. J. Collins, D. H. Thompson, and J. Irudayaraj, "PLGA-PEG nano-delivery system for epigenetic therapy," *Biomedicine & Pharmacotherapy*, vol. 90, pp. 586–597, 2017.

[21] S. Taghavi, M. Ramezani, M. Alibolandi, K. Abnous, and S. M. Taghdisi, "Chitosan-modified PLGA nanoparticles tagged with 5TR1 aptamer for in vivo tumor-targeted drug delivery," *Cancer Letters*, vol. 400, pp. 1–8, 2017.

[22] Q. L. Loh and C. Choong, "Three-dimensional scaffolds for tissue engineering applications: role of porosity and pore size," *Tissue Engineering Part B: Reviews*, vol. 19, no. 6, pp. 485–503, 2013.

[23] P. X. Ma and J.-W. Choi, "Biodegradable polymer scaffolds with well-defined interconnected spherical pore network," *Tissue Engineering Part A*, vol. 7, no. 1, pp. 23–33, 2001.

[24] R. Izquierdo, N. Garcia-Giralt, M. T. Rodriguez et al., "Biodegradable PCL scaffolds with an interconnected spherical pore network for tissue engineering," *Journal of Biomedical Materials Research Part A*, vol. 85, no. 1, pp. 25–35, 2008.

[25] W. Li, M. Petrimpol, K. D. Molle, M. N. Hall, E. J. Battegay, and R. Humar, "Hypoxia-induced endothelial proliferation requires both mTORC1 and mTORC2," *Circulation Research*, vol. 100, no. 1, pp. 79–87, 2007.

[26] B. Weigelt, A. T. Lo, C. C. Park, J. W. Gray, and M. J. Bissell, "HER2 signaling pathway activation and response of breast cancer cells to HER2-targeting agents is dependent strongly on the 3D microenvironment," *Breast Cancer Research and Treatment*, vol. 122, no. 1, pp. 35–43, 2010.

[27] J. N. Li, P. Cao, X. N. Zhang, S. X. Zhang, and Y. H. He, "In vitro degradation and cell attachment of a PLGA coated biodegradable Mg-6Zn based alloy," *Journal of Materials Science*, vol. 45, no. 22, pp. 6038–6045, 2010.

[28] K. M. Hakkinen, J. S. Harunaga, A. D. Doyle, and K. M. Yamada, "Direct comparisons of the morphology, migration, cell adhesions, and actin cytoskeleton of fibroblasts in four different three-dimensional extracellular matrices," *Tissue Engineering Part A*, vol. 17, no. 5-6, pp. 713–724, 2011.

[29] E. Knight and S. Przyborski, "Advances in 3D cell culture technologies enabling tissue-like structures to be created in vitro," *Journal of Anatomy*, vol. 227, no. 6, pp. 746–756, 2015.

[30] C. M. Taylor, B. Blanchard, and D. T. Zava, "Estrogen receptor-mediated and cytotoxic effects of the antiestrogens tamoxifen and 4-hydroxytamoxifen," *Cancer Research*, vol. 44, no. 4, pp. 1409–1414, 1984.

[31] V. Hongisto, S. Jernström, V. Fey et al., "High-throughput 3D screening reveals differences in drug sensitivities between culture models of JIMT1 breast cancer cells," *PLoS ONE*, vol. 8, no. 10, Article ID e77232, 2013.

[32] C. G. Knight, L. F. Morton, D. J. Onley et al., "Identification in collagen type I of an integrin $\alpha 2\beta 1$-binding site containing an essential GER sequence," *The Journal of Biological Chemistry*, vol. 273, no. 50, pp. 33287–33294, 1998.

[33] W. Ding, X.-L. Fan, X. Xu et al., "Epigenetic silencing of ITGA2 by MiR-373 promotes cell migration in breast cancer," *PLoS ONE*, vol. 10, no. 8, Article ID e0135128, 2015.

[34] G. P. H. Gui, J. R. Puddefoot, G. P. Vinson, C. A. Wells, and R. Carpenter, "In vitro regulation of human breast cancer cell adhesion and invasion via integrin receptors to the extracellular matrix," *British Journal of Surgery*, vol. 82, no. 9, pp. 1192–1196, 1995.

[35] A. Lochter, M. Navre, Z. Werb, and M. J. Bissell, "$\alpha 1$ and $\alpha 2$ integrins mediate invasive activity of mouse mammary carcinoma cells through regulation of stromelysin-1 expression," *Molecular Biology of the Cell*, vol. 10, no. 2, pp. 271–282, 1999.

[36] M. M. Zutter, S. A. Santoro, W. D. Staatz, and Y. L. Tsung, "Re-expression of the $\alpha 2\beta 1$ integrin abrogates the malignant phenotype of breast carcinoma cells," *Proceedings of the National Acadamy of Sciences of the United States of America*, vol. 92, no. 16, pp. 7411–7415, 1995.

[37] M. Cekanova and K. Rathore, "Animal models and therapeutic molecular targets of cancer: utility and limitations," *Drug Design, Development and Therapy*, vol. 8, pp. 1911–1922, 2014.

[38] R. F. Song, X. J. Li, X. L. Cheng et al., "Paclitaxel-loaded trimethyl chitosan-based polymeric nanoparticle for the effective treatment of gastroenteric tumors," *Oncology Reports*, vol. 32, no. 4, pp. 1481–1488, 2014.

[39] H. Zhang, H. Hu, H. Zhang et al., "Effects of PEGylated paclitaxel nanocrystals on breast cancer and its lung metastasis," *Nanoscale*, vol. 7, no. 24, pp. 10790–10800, 2015.

[40] C. Sánchez, P. Mendoza, H. R. Contreras et al., "Expression of multidrug resistance proteins in prostate cancer is related with cell sensitivity to chemotherapeutic drugs," *The Prostate*, vol. 69, no. 13, pp. 1448–1459, 2009.

[41] X. Xu, M. C. Farach-Carson, and X. Jia, "Three-dimensional in vitro tumor models for cancer research and drug evaluation," *Biotechnology Advances*, vol. 32, no. 7, pp. 1256–1268, 2014.

[42] M. Håkanson, M. Textor, and M. Charnley, "Engineered 3D environments to elucidate the effect of environmental parameters on drug response in cancer," *Integrative Biology*, vol. 3, no. 1, pp. 31–38, 2011.

[43] C. Fischbach, R. Chen, T. Matsumoto et al., "Engineering tumors with 3D scaffolds," *Nature Methods*, vol. 4, no. 10, pp. 855–860, 2007.

[44] B. Kocatürk and H. H. Versteeg, "Orthotopic injection of breast cancer cells into the mammary fat pad of mice to study tumor growth," *Journal of Visualized Experiments*, no. 96, Article ID e51967, 2015.

[45] E. Iorns, K. Drews-Elger, T. M. Ward et al., "A new mouse model for the study of human breast cancer metastasis," *PLoS ONE*, vol. 7, no. 10, Article ID e47995, 2012.

Hindawi
International Journal of Biomaterials
Volume 2017, Article ID 1256537, 11 pages
https://doi.org/10.1155/2017/1256537

Research Article

Effect of Injection Molding Melt Temperatures on PLGA Craniofacial Plate Properties during *In Vitro* Degradation

Liliane Pimenta de Melo,[1] Gean Vitor Salmoria,[1,2] Eduardo Alberto Fancello,[1,3] and Carlos Rodrigo de Mello Roesler[1]

[1] *LEBm Biomechanics Engineering Laboratory, University Hospital (HU), Federal University of Santa Catarina, 88040-900 Florianópolis, SC, Brazil*
[2] *NIMMA Laboratory of Innovation on Additive Manufacturing and Molding, Federal University of Santa Catarina, 88040-900 Florianópolis, SC, Brazil*
[3] *GRANTE, Department of Mechanical Engineering, Federal University of Santa Catarina, 88040-900 Florianópolis, SC, Brazil*

Correspondence should be addressed to Liliane Pimenta de Melo; liliane.eng@gmail.com

Received 10 June 2017; Revised 24 July 2017; Accepted 30 July 2017; Published 6 September 2017

Academic Editor: Junling Guo

Copyright © 2017 Liliane Pimenta de Melo et al. This is an open access article distributed under the Creative Commons Attribution License, which permits unrestricted use, distribution, and reproduction in any medium, provided the original work is properly cited.

The purpose of this article is to present mechanical and physicochemical properties during *in vitro* degradation of PLGA material as craniofacial plates based on different values of injection molded temperatures. Injection molded plates were submitted to *in vitro* degradation in a thermostat bath at 37 ± 1°C by 16 weeks. The material was removed after 15, 30, 60, and 120 days; then bending stiffness, crystallinity, molecular weights, and viscoelasticity were studied. A significant decrease of molecular weight and mechanical properties over time and a difference in FT-IR after 60 days showed faster degradation of the material in the geometry studied. DSC analysis confirmed that the crystallization occurred, especially in higher melt temperature condition. DMA analysis suggests a greater contribution of the viscous component of higher temperature than lower temperature in thermomechanical behavior. The results suggest that physical-mechanical properties of PLGA plates among degradation differ per injection molding temperatures.

1. Introduction

Poly(lactic-co-glycolic acid), PLGA, is a biocompatible, biodegradable, and FDA-approved polymer. In the last two decades, PLGA has been considered as one of the most promising polymers for biomedical engineering applications, such as plates and screws in craniofacial surgery [1–4]. One of the techniques used in the manufacturing of medical devices is injection molding, which allows the development of complex mold geometries. However, mechanical properties stability and physicochemical properties of the resorbable material can also be strongly influenced by manufacturing process and design of the devices [5–8].

PLGA plates and screws must have suitable strength and ductility for biomechanical function, biocompatibility, and degradation. In particular, melt processing temperatures during injection molding could develop different microstructures of the manufactured device, including other operative parameters, such as mold temperature, injection flow rate, and holding pressure [9]. As semicrystalline, PLGA devices are heterogeneous systems comprised of highly anisotropic crystallites, a phase in which the chains show long-range 3D order. The size and distribution of these crystals and the viscoelasticity are extremely dependent on the molecular weight distribution and the conditions under which the material is processed [10]. In manufacturing, the parameters can affect viscosity and chain orientation during the process of molded devices, where crystallinity is an important parameter because it can increase flexural stiffness and decrease the impact properties of the final product [10, 11].

Once properties of resorbable polymers devices are established, degradation rate must be evaluated. Many factors could influence degradation rate, such as implant site, mechanical stress, molar mass distribution, chemical/stereoisometric composition, crystallinity, morphology, size and geometry of the carrier, and surface roughness

[10, 12–17]. Biodegradation and reabsorption process of poly(α-hydroxy acids) is a succession of events. Material is initially hydrated exposed to the body's aqueous fluids. With water molecules presence, the degradation process occurs through the hydrolysis of the ester linkages, resulting in products in the form of soluble and nontoxic oligomers (or monomers). The degradation proceeds passive hydrolytic cleavage, characterized by changes in molecular weight, glass transition temperature (T_g), moisture content, and mechanical properties, such as tensile and compressive strength [13, 18, 19]. Therefore, time for osteosynthesis must be less than the time of the mechanical properties retention.

In this work, PLGA plates were designed and manufactured by injection molding as craniofacial bioresorbable medical devices. Two different melt temperatures were tested for the injection molding process (i.e., 240 and 280°C). The high melt temperature condition was defined as the upper work limit temperature of injection molding manufacturing, while lower temperature was defined by minimum processability temperature. For both conditions, PLGA craniofacial plates were evaluated by mechanical properties (bending stiffness, flexural maximum strength, and storage modulus), physicochemical properties (crystallinity and transitions temperatures), and morphology during *in vitro* degradation.

2. Materials and Methods

2.1. Material. Poly(L-lactic-co-glycolic acid) 85/15 granules (PURASORB PLG 8531) were purchased by PURAC Biomaterials (Netherlands). The PLGA 85/15 showed an average molecular weight, Mn = 224.27 g/mol, and a polydispersity index of 1.87 (Gel Permeation Chromatography, Viscotek VE 2001, Viscotek Detector TDA 302, USA, 2008). The transition temperatures declared by the manufacturer are Tg = 57 ± 1°C and Tm = 140°C and intrinsic viscosity was 3.04 dl/g (chloroform, 25°C, c = 0.1 g/dl) (PURAC, 2012).

2.2. Plates Design and Processing. The implant was designed by 3D CAD SolidWorks 2014 software (Concord, MA). The design of the craniofacial plate device is characterized by 2 mm of thickness, 5.8 mm of width, and 38.7 mm of length and by 8 aligned holes of 2 mm semicircle screw thread. The pellets of PLGA were processed using an injection molding machine (ARBURG 270S, 250-70 model). To investigate processing influence on PLGA plates properties, two different melt injection temperatures were considered: low temperature (T = 240°C, PLGA_low$T$) and high temperature (T = 280°C, PLGA_high$T$). The other processing parameters were kept constant, as summarized in Table 1.

2.3. In Vitro Hydrolytic Degradation. Injection molded plates (0.25 ± 0.01 g per sample/plate) were desinfected by immersion in 70% v/v ethanol. Samples were immersed (n = 16, per each condition, per time point) in the phosphate-buffered saline (PBS) solution (0.25 g/30 ml, pH = 7.4) by storing them in the thermostatic bath (37 ± 1°C) for 15, 30, 60, and 120 days. At each time point, the degradation solution pH (pH = 7.4) was recorded and the samples were removed from the buffer solution, washed, and held in distilled water for 1 hour to remove as much buffer solution as possible. They were weighed in the wet condition and then dried in a vacuum oven at 23°C for 8 h. The samples were kept under vacuum prior to the characterization tests.

Table 1: Injection molding parameters used to produce PLGA plates. All the production parameters were kept constant while varying the melt injection temperature (240°C for PLGA_low$T$ and 280°C for PLGA_high$T$).

	PLGA_low$T$	PLGA_high$T$
Melt injection temperatures	240°C	280°C
Mold temperature	25°C	
Injection pressure	1500 MPa	
Holding pressure	25 MPa	
Injection time	2 s	
Cooling time	90 s	
Screw speed	100 rpm	

2.4. Dynamic Mechanical Analyses. PLGA_low$T$ and PLGA_high$T$ specimens were submitted to the mechanical characterization, performed by a Dynamic Mechanical Analyzer (DMA Q800, TA Instruments) at the different degradation points (i.e., 0, 15, 30, 60, and 120 days). For viscoelasticity analysis, samples (n = 6, gauge length = 16 mm) were tested by setting 1 Hz frequency and 0.1% relative strain of area. DMA tests were performed in the temperature range of 30–80°C at a temperature rate of 3°C min^{-1}. From each test, storage modulus (E'), loss modulus (E''), and tan $\delta(E''/E')$ trends in function of the temperature were obtained and the transition temperatures were determined as peak in tan δ trends.

For three-point bending tests, samples (n = 5, gauge length = 10 mm) were tested in three-point flexural mode (ASTM D790) [20], kept at 37°C, using a test speed of 2 N min^{-1}. The considered mechanical parameters were bending stiffness (E_f), maximum bending deformation (ε_f), and flexural stress (σ_f), calculated according to the following equation:

$$\sigma_f = \frac{3PL}{2bd^2}, \tag{1}$$

where σ_f is stress in the outer fibers at midpoint (MPa); P is load at a given point on the load-deflection curve (N); L is support span (mm); b is width of beam tested (mm); and d is depth of beam tested (mm).

2.5. Differential Scanning Calorimeter Analysis. The crystallinity and thermal properties (melting point, T_m, glass transition temperature, T_g, enthalpy of cold crystallization, ΔH_c, and enthalpy of melting, ΔH_m) were obtained by using a DSC (Shimadzu DSC-6000) in a nitrogen atmosphere of 19 cm^3 m^{-1}, using aluminum oxide as standard. The applied heating rate was 10°C min^{-1}, from 10 to 250°C, using an average sample size of 7 mg taken from the central region of

Table 2: Mechanical properties of injection molded PLGA 85/15 plates (mean ± standard deviation, $n = 3$): flexural stiffness, E; flexural strength, σ_r; and maximum flexural strain, ε_r ($^*p < 0.05$).

		E (GPa)*	σ_r (MPa)*	ε_r (%)*
PLGA_low$T$	0 days	2.2 ± 0.1	41.4 ± 11.8	2.6 ± 0.8
	15 days	2.1 ± 0.2	54.6 ± 3.9	3.5 ± 0.5
	30 days	1.5 ± 0.1	12.5 ± 7.7	1.3 ± 0.7
	60 days	1.2 ± 0.1	19.05 ± 0.8	2.8 ± 0.4
PLGA_high$T$	0 days	1.9 ± 0.1	30.1 ± 3.1	2.3 ± 0.2
	15 days	2.1 ± 0.07	42.3 ± 7.2	2.9 ± 0.6
	30 days	1.9 ± 0.3	24.5 ± 15.3	1.8 ± 0.7
	60 days	0.5 ± 0.1	4.1 ± 0.8	1.0 ± 0.1

molded specimens ($n = 3$). Degree of crystallinity (X_c) was determined by using the following formula:

$$X_c = 100 \times \left(\frac{\Delta H_m - \Delta H_{cc}}{\Delta H_m^c} \right) \times \frac{1}{1 - m_f}, \quad (2)$$

where ΔH_m is enthalpy of fusion, ΔH_{cc} is enthalpy of cool crystallization, ΔH_m^c is heat of melt of purely crystalline PLA, taken as 93 J/g [10, 19], and $(1 - m_f)$ is weight fraction of the polymer in the sample. Crystallization temperature (T_{cc}) was obtained from the second heating.

2.6. Fourier Transform Infrared Spectroscopy. Fourier transform infrared spectroscopy (FT-IR) was performed using attenuated total reflection (ATR) mode on a Shimadzu spectrometer, model TENSOR 27. The spectra of the samples ($n = 3$) were obtained in 4000 to 600 cm^{-1} wavenumbers by 4 cm^{-1} resolution. FTIR analysis identified bioresorbable copolymer functional groups and the possible changes due to the degradation.

2.7. Gel Permeation Chromatography. Molar mass distribution of the PLGA copolymer was verified by a high-performance liquid chromatography (GPC) Viscotek VE 2001 coupled to the Viscotek Detector TDA 302, Houston, Texas, USA (2008). THF solvent was used as the mobile phase and the parameters included flow rate at 1000 ml/min, injection volume of 100 ul, increment volume of 0.00333 ml, and detector and column temperature of 45°C. The injected volume was always 100 μL and flow velocity was 1 $cm^3\,min^{-1}$. PLA samples were used as standard.

2.8. Scanning Electron Microscopy. SEM was used to observe the surface morphology of PLGA plates during the *in vitro* degradation. At each time point (i.e., 0, 15, 30, 60, and 120 days), PBS was removed from the samples and immersed in distilled water for 2 h. After that, the samples were kept under vacuum for SEM observation. The samples ($n = 2$) were covered with a thin layer of gold/palladium using a cathodic spray (Diode Sputtering System, International Scientific Instruments) and observed at different magnifications (original ×13) with an acceleration voltage of 10 kV in a scanning electron microscope (SEM) Jeol JSM-6390L model.

2.9. Statistical Data Treatment. Analysis of variance (ANOVA) was performed considering a statistical significance set at 0.05; p value was investigated for significance of the factors among melt temperatures. All data are reported as mean ± standard deviation.

3. Results

3.1. Mechanical Tests Analyses. The flexural stiffness, flexural strength, and maximum flexural strain of PLGA_ low and PLGA_high$T$ are summarized in Table 2.

Flexural stiffness values, E, showed 2.2 ± 0.1 and 1.9 ± 0.1 GPa for plates without degradation (0 days) for PLGA_low$T$ and PLGA_high$T$, respectively, and the flexural strength, σ_r, was 41.4±11.8 and 30.1±3.1 MPa, respectively. In the flexural test, PLGA plates presented break under all conditions. This is probably due to the presence of crystallinity and chain organization during the solidification of the material in the injection molding process. PLGA_low$T$ plates support additional load, exhibiting greater flexural strength at 0 days of degradation. Flexural curves for PLGA_low$T$ and PLGA_high$T$ during degradation are shown in Figure 1.

Mechanical properties decrease especially after 30 days studied. DMA curves of PLGA_low$T$ and PLGA_high$T$ during the degradation study are shown in Figure 2. Storage modulus (E') showed comparable trends and values for the two injection molding temperatures. The storage modulus E' (T_g at 37°C) was 1.2 ± 0.2 GPa for both conditions in plates without degradation. The behavior of $\tan\delta$ was different for the two conditions processed. In particular, the highest values achieved for PLGA_high$T$ are related to a higher loss modulus. This behavior suggests a greater contribution of the viscous component of PLGA_high$T$ than PLGA_low$T$ in thermomechanical behavior. T_g detected as peak in the $\tan\delta$ trend was 57.4 ± 1.8°C for both conditions.

Storage modulus E' is the component related to the elastic energy stored; and E'' is related to dissipated viscous energy. Both properties decreased significantly at point 3 (60 days).

3.2. Differential Scanning Calorimeter Analysis. Values of crystallinity (X_c), transition temperatures (T_g, T_{m1}, T_{m2}, T_c), and enthalpies detected by DSC ($\Delta H_{cc}, \Delta H_m, \Delta H_g$) are shown in Table 3. The values correspond to PLGA_low$T$ and

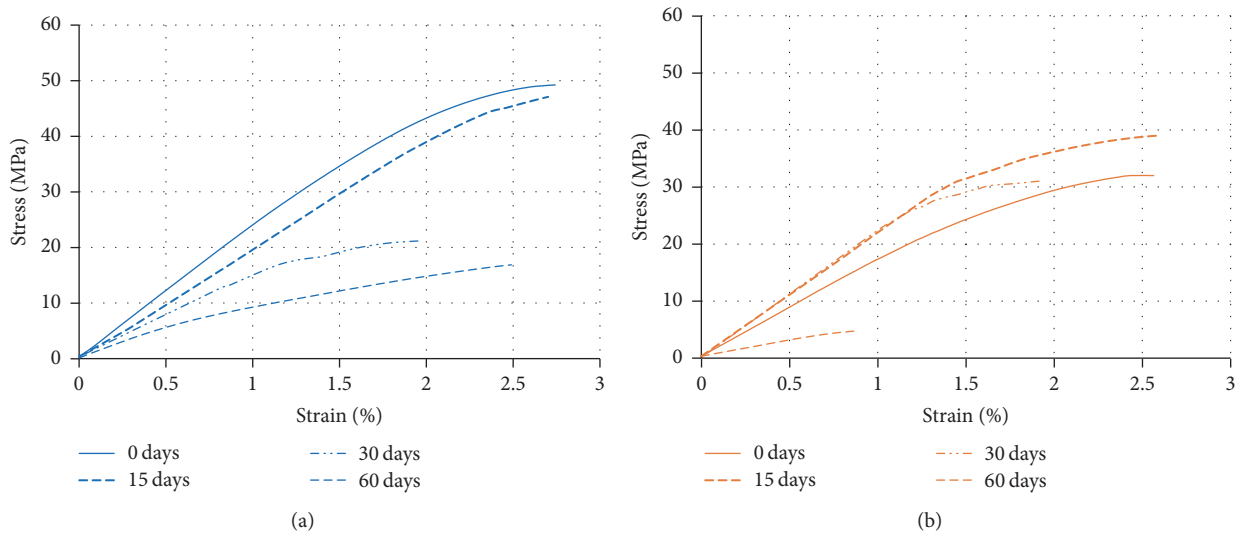

Figure 1: Representative stress-strain curves of PLGA_low$T$ (a) and PLGA_high$T$ (b) at all degradation time points obtained by flexural tests.

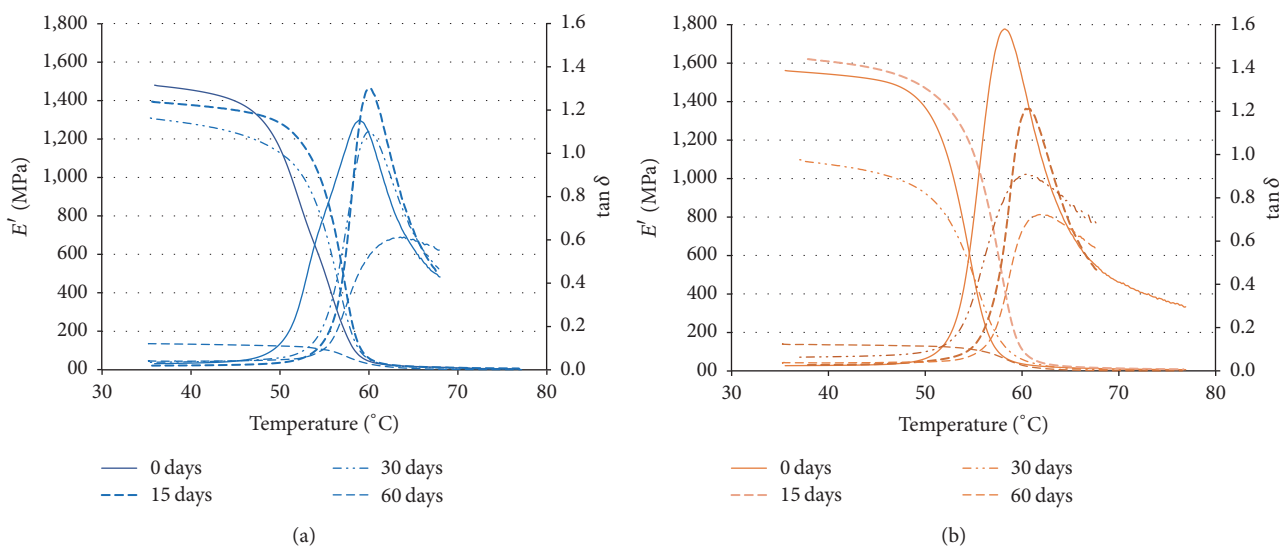

Figure 2: Representative curves of storage modulus (E') and tan $\delta(E''/E')$ as a function of the temperature obtained by DMA of the different degradation points (e.g., 0, 15, 30, 60, and 120 days) for PLGA_low$T$ (a) and PLGA_high$T$ (b).

PLGA_high$T$, (i.e., 0, 15, 30, 60, and 120 days) and for PLGA_pellet as a control.

The glass transition temperature occurs at 56.0 ± 0.5°C for PLGA_low$T$ and at 52.7 ± 0.9°C for PLGA_high$T$ at the first point studied without degradation (i.e., 0 days). The glass transition temperature of the preprocessed PLGA samples (pellet) was detected at 60.4 ± 1.8°C. Changes in transition temperatures for PLGA_low$T$ and PLGA_high$T$, compared to PLGA_pellet, may be referred to changes related to the molecular chain during the injection molding processing. The endothermic melting peak of PLGA_low$T$ appeared at 156.6 ± 0.2°C. Considering PLGA_high$T$, this peak occurs twice in one shoulder at 151.0 ± 2.2°C and 157.9 ± 1.1°C, due to differences in crystallinity. Percent crystallinity was measured by the calculation of (2).

The DSC curves show the difference in the endothermic peaks and the presence of high crystallinity only for PLGA_high$T$. In addition, there is shoulder presence indicating two melt temperatures (146 and 157°C), related to the PGA (15%) and PLA (85%) fractions, respectively. For PLGA_low$T$, a very mild melting endotherm occurs at 153.1 ± 0.3°C, which could indicate a second T_m, even if this value is very close to the detected T_m.

The decrease presented by Tg of the copolymer (Figure 3), as a function of the degradation time, in the period from 0 to 120 days (from 56.0 ± 0.5°C with 0 days to 41.7 ± 6.6°C for PLGA_low$T$ in 120 days and from 52.7 ± 0.9 to 41.6 ± 0.8°C for PLGA_high$T$) indicates rapid hydrolytic degradation of plates in PBS medium. In fact, this is characteristic of PLGA copolymers. At the beginning of the degradation process, T_g

Table 3: Degree of crystallinity (X_c) and thermal properties measured by DSC: glass-transition temperature (T_g), melting point (T_m), enthalpy of cold crystallization (ΔH_c), enthalpy of glass (ΔH_g), and enthalpy of melting (ΔH_m) ($^*p < 0.05$).

		T_g [°C]*	T_{m1} [°C]	T_{m2} [°C]	T_c [°C]*	ΔH_{cc} [J/g]*	ΔH_m [J/g]*	ΔH_g [J/g]*	X_c [%]*
	Pellet	60.4 ± 1.8	—	146.1 ± 0.1	—	—	33.4 ± 2.4	1.7 ± 0.4	35.7
PLGA_low$T$	0 days	56.0 ± 0.5	153.1 ± 0.3	156.6 ± 0.2	130.7 ± 2.4	−2.3 ± 0.6	4.3 ± 1.5	5.1 ± 0.5	7.1
	15 days	53.0 ± 3.2	153.8 ± 2.2	157.5 ± 1.8	131.0 ± 0.1	−8.9 ± 2.2	5.0 ± 2.6	5.9 ± 1.3	14.8
	30 days	51.8 ± 1.2	153.6 ± 0.9	156.4 ± 1.0	99.9 ± 7.7	−17.5 ± 3.1	14.5 ± 6.9	9.6 ± 4.0	34.1
	60 days	48.3 ± 0.3	138.7 ± 4.2	147.3 ± 5.4	87.4 ± 4.1	−35.3 ± 7.8	28.6 ± 6.8	7.1 ± 12.0	68.2
	120 days	41.7 ± 6.6	120.4 ± 0.2	133.5 ± 1.0	95.5 ± 0.1	−30.2 ± 0.9	19.7 ± 8.7	14.1 ± 3.8	53.3
PLGA_high$T$	0 days	52.7 ± 0.9	151.0 ± 2.2	157.9 ± 1.0	124.5 ± 4.2	−24.0 ± 8.1	17.9 ± 5.1	3.1 ± 0.3	44.7
	15 days	52.5 ± 3.1	154.1 ± 0.1	157.2 ± 2.0	127.1 ± 14.5	−9.9 ± 4.3	7.9 ± 3.0	9.1 ± 0.4	19.0
	30 days	52.6 ± 0.8	152.0 ± 0.1	156.6 ± 0.4	102.1 ± 8.3	−68.6 ± 3.6	19.1 ± 7.1	10.5 ± 0.5	93.7
	60 days	52.0 ± 1.1	153.7 ± 0.7	157.7 ± 1.7	89.0 ± 3.9	−47.9 ± 2.2	7.9 ± 7.0	11.8 ± 6.5	59.6
	120 days	41.6 ± 0.8	144.4 ± 2.8	152.4 ± 3.2	96.6 ± 1.3	−28.9 ± 6.9	23.2 ± 4.1	0.4 ± 0.1	55.7

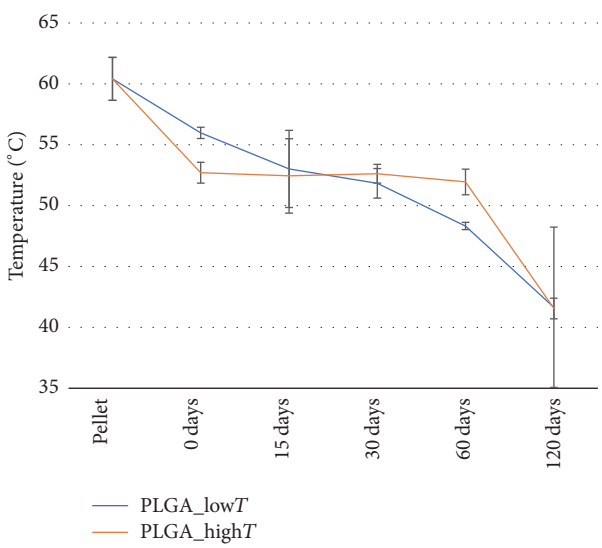

Figure 3: Glass transition temperatures (Tg) measured by the DSC for PLGA_low$T$ and PLGA_high$T$.

decrease could be associated with the plasticizing effect of the plates by the H_2O absorption [17]. Moreover, there is an advanced degree of degradation of plates from 60 days.

3.3. Fourier Transform Infrared Spectroscopy. Absorption bands were identified in the spectrum of the PLGA_low$T$ and PLGA_high$T$ plates at the different degradation periods: an intense band between 1760 and 1750 cm^{-1}, characteristic of carbonyl (C=O), present in the two monomers, and a bonding band (C-O) between 1300 cm^{-1} and 1150 cm^{-1}, characteristic of the ester groups. The absorption bands that are characteristic of the functional groups present in the PLGA copolymer can be observed in the spectra (Figure 4) and are shown in Table 4.

The presence of the O-C=O group near the absorption band 1600–1500 cm^{-1} indicates signs of degradation; note that the presence of this band occurs in 60 and 120 days of degradation in PBS solution. Usually the appearance of

Table 4: Absorption bands identified in the FT-IR assay characteristic of the functional groups present in the PLGA copolymer.

Absorption bands (cm^{-1})	Groups
3000–2850	CH, CH_3 e CH_2
1760–1745	C=O
1600–1500	O-C=O (oligomer)
1450–1370	CH_3 and CH_2
1350–1150	CH_2 and CH
1300–1150	C-O
800–750	CH

a band at 3400 cm^{-1} relating to vibration of OH bands in groups -COO-H and -CO-H at the ends of strings is observed, indicating a reduction in their size, and also the occurrence of the peak at 1605 cm^{-1} corresponds to the asymmetric stretch of the -COO- group in oligomers.

3.4. Gel Permeation Chromatography. Figure 5 shows the molar mass distribution (e.g., M_n, M_w, M_z, and M_p) of the PLGA studied for the pellet and for the other times of degradation.

Based on the results presented, PLGA plates have a narrow (low polydispersity) and monomodal (only one peak) molar mass distribution. The pellet represents unprocessed PLGA, in which high molecular mass (e.g., 183407 ± 28895 Da) was identified. As shown in Figure 5, values of molar mass M_n decrease from pellet to 0 days of degradation, which can be explained by material processing during injection molding.

PLGA plates' degradation can be observed by mass loss during the time of contact with the phosphate buffer solution; however, the degradation speed between PLGA_low$T$ and PLGA_high$T$ was different. This behavior probably occurred due to the reduction of the amorphous phase of the polymers, since the molecular interaction of the solution with the copolymer is more propitious in the amorphous phase. According to Middleton and Tipton (2000) [12], in the first stage of degradation, there is diffusion of water in the amorphous regions of the polymer and hydrolytic cleavage

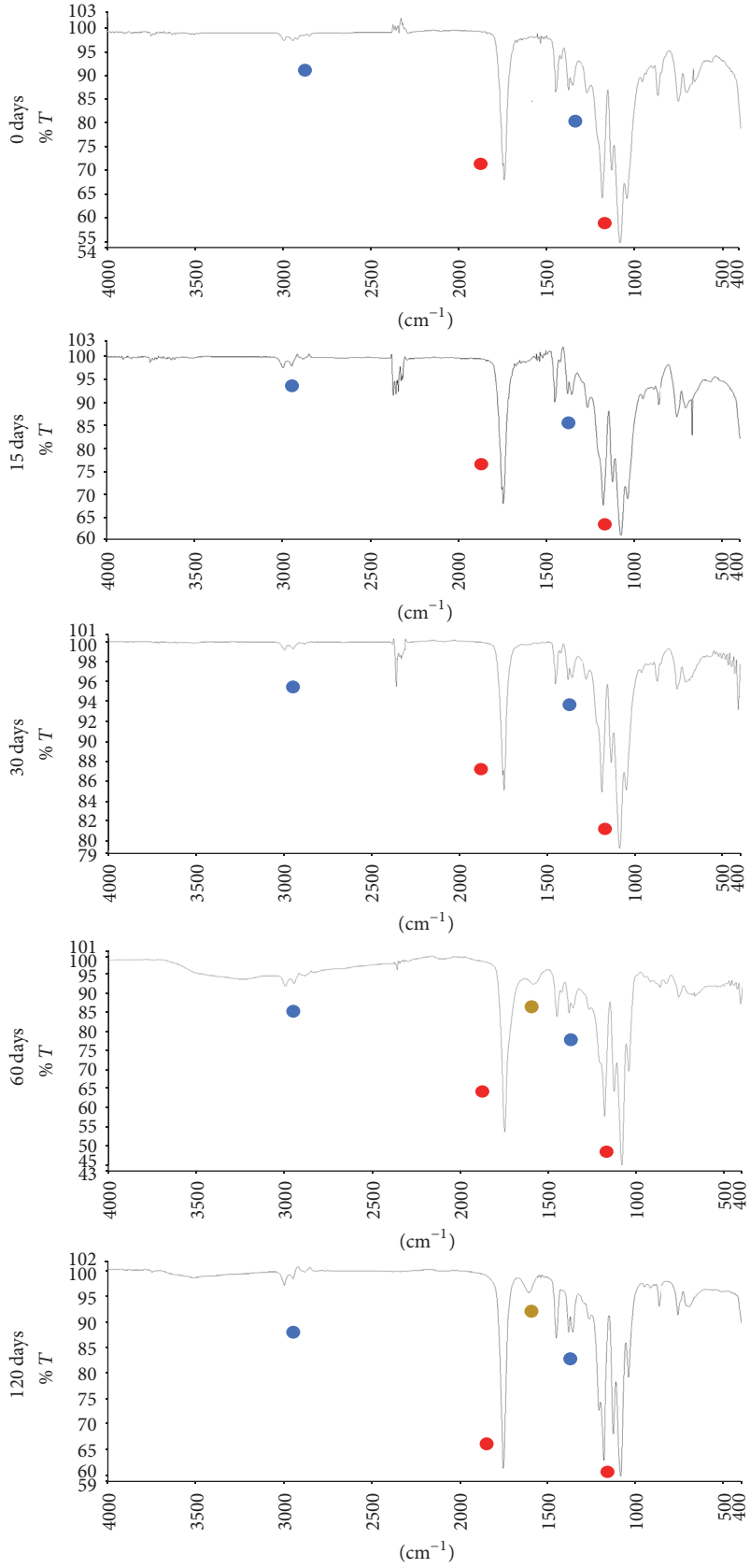

Figure 4: Spectrum related to degradation points 0 to 4 of PLGA plates for the period of 0, 15, 30, 60, and 120 days, respectively. Ester groups = red: 1760–1745 cm^{-1} and 1300–1150 cm^{-1}; alkanes groups = blue: 3000–2800 cm^{-1} and 1450–1370 cm^{-1}; oligomer groups = yellow: 1600–1500 cm^{-1}.

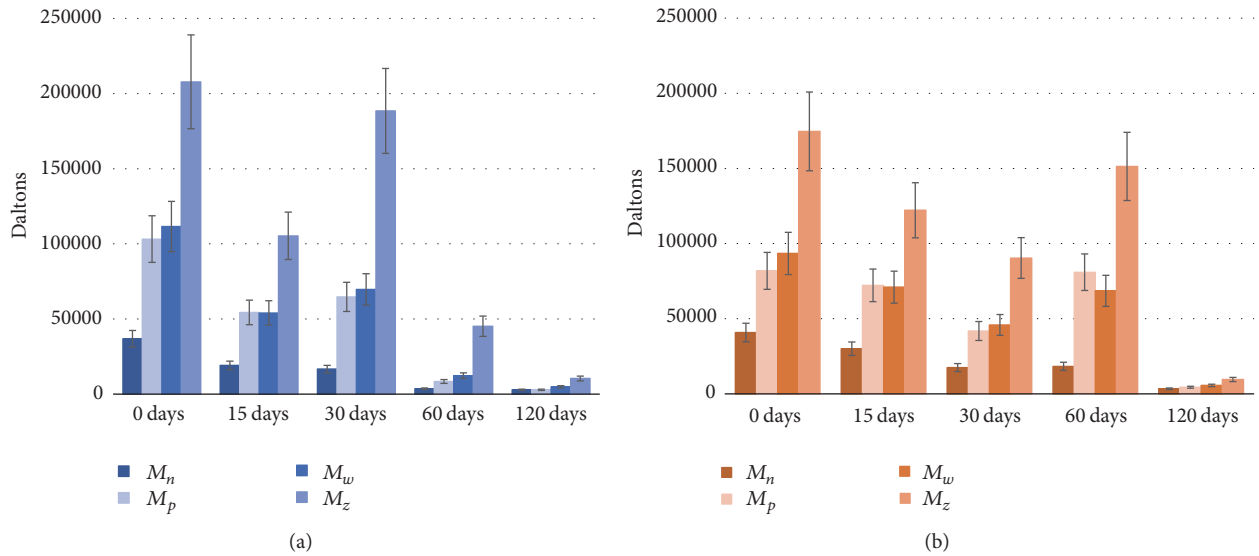

Figure 5: Molar mass (mean ± deviation) of the PLGA plates in the 0, 15, 30, 60, and 120 days of degradation in PBS solution for PLGA_low$T$ (a) and PLGA_high$T$ (b).

of the ester bonds of the polymer chains. After much of the amorphous phase undergoing degradation begins the second stage in the crystalline phase; therefore, there is a percentage increase in the degree of crystallinity.

3.5. Scanning Electron Microscopy. PLGA plates' degradation during the immersion period in phosphate buffer solution (PBS, 37°C) is qualitatively confirmed by the SEM images (magnification ×13), as shown in Figure 6.

Figure 7 shows the material degradation process for PLGA_low$T$ and PLGA_high$T$, which coincides with the results obtained from the SEM analyses.

Initially transparent PLGA plates become opaque when degradation process begins. The whitish aspect of the device is clear in the first 15 days in phosphate buffer solution, which is an indication of the influence of the degradation process, as a function of the organization of the chains during the degradation. During the process, the deformation and brittle feature of the material can be noted. After 120 days, it was possible to notice the crumbling of the material and the absence of mechanical properties. The whitish form can be noted in point 1 for PLGA_high$T$, which is less evident in PLGA_low$T$. That could indicate that PLGA_high$T$ is more sensitive to hydrolytic degradation in less time.

4. Discussion

PLGA copolymer is a promising material for medical devices applications as craniofacial plates. Medical devices manufactured from aliphatic polyesters degrade through hydrolysis of the polymer backbone primarily through a bulk degradation process that includes decline of molecular weight, reduction in mechanical properties, and loss of mass. Hydrolytic degradation can be evaluated through molar mass (GPC), presence of polar groups or oligomers and monomers (FTIR), and changes in mechanical properties (DMA), transition temperature changes (DSC), and surface and geometry (SEM) [21–23]. This study reported the *in vitro* degradation of PLGA craniofacial plates tested in two different melt temperatures of the injection molding process (i.e., 240 and 280°C), corresponding to the processable limits of PLGA, at different time points. Physicochemical properties such as molecular weight and mechanical properties were monitored by FTIR, DSC, and DMA analysis. The results suggested that the property changes differ according to the injection molding temperature.

The flexural strengths for the PLGA plates studied in this work ranged from 1.9 ± 0.1 to 2.2 ± 0.1 GPa, which compared with the stiffness (E) of bone (E_{bone} ~ 6–20 GPa), metal (E_{metal} = 100–200 GPa), and poly(lactic acid) (11–72 MPa) [24], indicating a possible use of these plates under investigation in non-load-bearing body sites, such as for craniofacial bone fractures. However, bioresorbable plates PGA-based copolymers have higher degradation rate than other bioresorbable polymers, which limits the useful time of the devices [25, 26]. Both PLGA plates conditions (i.e., PLGA_low$T$ and PLGA_high$T$) showed rapid degradation, regardless of the different characteristics of the microstructure during the degradation.

The evaluated mechanical properties of PLGA_low$T$ and PLGA_high$T$ showed suitable values at the beginning of degradation [27–30]. However, PLGA_high$T$ plates reached flexural strength peak and maximum flexural strain after 15 days, as observed in Figure 1. A possible reason for this result is related to the diffusion effect order from PBS solution to PLGA plates: first, the diffusion occurs to lower molecular weight chains of PLGA and then to higher molecular chains. In addition, degradation of resorbable polymers begins from higher molecular weight to lower molecular weight chains over time on PBS solution. In addition, smaller polymer chains can rearrange and relax over time before larger chains degrade. Thus, the diffusion to the solution of lower

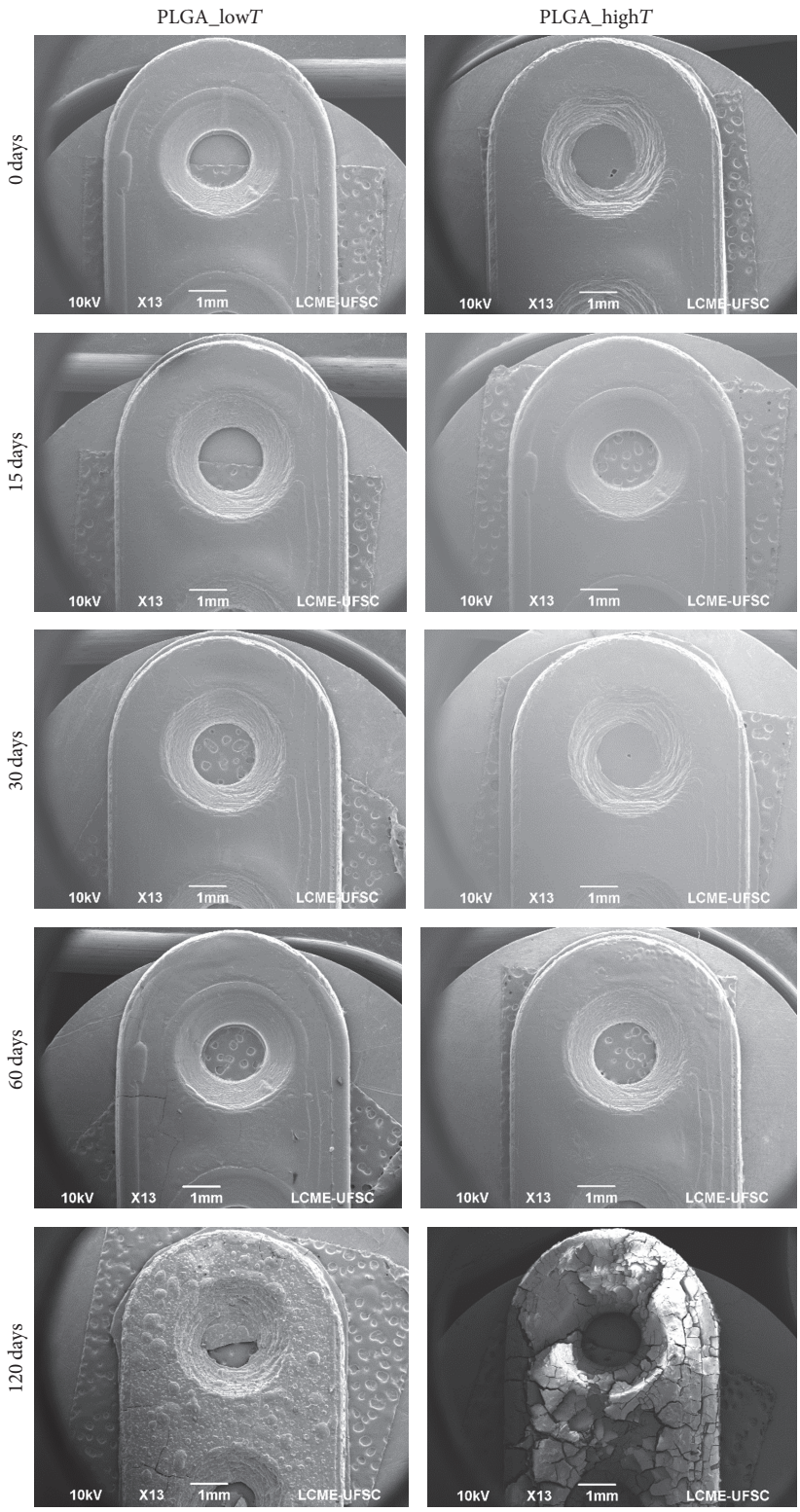

Figure 6: SEM images of the PLGA_low$T$ and PLGA_high$T$ plates at different degradation time (0, 15, 30, 60, and 120 days) (bar scale = 1 mm).

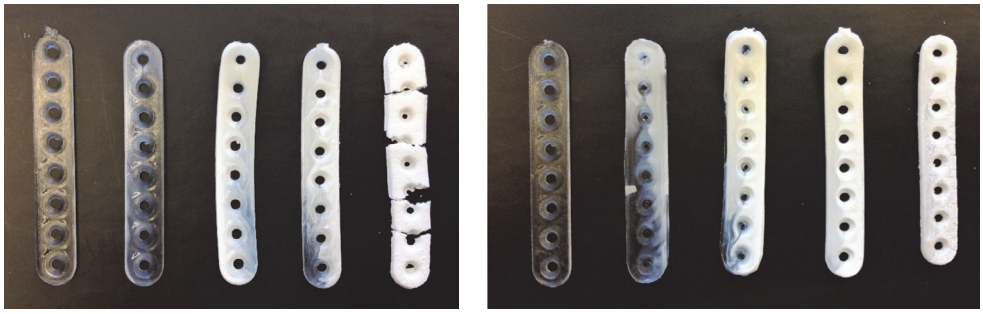

(a) (b)

Figure 7: Visual appearance images of the degradation of the PLGA_low$T$ (a) and PLGA_high$T$ (b) plates at the different degradation points: 0, 15, 30, 60, and 120 days from left to right.

molecular weight chains of PLGA prior to degradation of the higher molecular weight fractions renders the material stiffer after 15 days but with continuing decrease after degradation of the material.

Moreover, Table 3 shows crystallinity and thermal properties on degradation of the plates which could be associated with chains hydrolysis, diffusion, and erosion. At the beginning of the degradation, the phenomenon of surface erosion can be observed, where molar weight loss is exclusively from the outside to the inside of the material, where diffusion of the water molecules, for example, is slower than the release of fragments from the surface. In another case, the volumetric degradation occurs when water penetrates the polymer matrix homogeneously, causing hydrolysis throughout. In this event, there is a relationship between hydrolysis of the chains and their diffusion and erosion. If any disturbance occurs, this equilibrium may be undone and a variation of the mechanism known as autocatalysis via carboxylic and hydroxyl groups may occur. This autocatalysis in volumetric degradation causes an acid gradient in the inner part of the body, causing accelerated degradation to occur at this site compared to the surface. The oligomers generated in the central regions can easily diffuse to the surface. This effect, accompanied by the presence of acid products, may result in inflammatory reactions in *in vivo* cases. It is worth mentioning that the degradation of devices implanted in the human body, an object of interest in this work, tends to present an increase in the rate of diffusion and consequent degradation due to the body temperature around 37°C, variations in pH, and eventual efforts which may increase the probability of breaking connections [13, 18, 19, 31]. An increase in molecular weight will result in more covalent bonds and thus an increased number of entanglements and thereby increasing resorption/degradation time [32].

The decrease of properties (Figure 8) was evident at each time point of the degradation for PLGA_low$T$; however, viscoelasticity properties possibly influenced the dispersion for PLGA_high$T$ in the first 60 days of degradation, which showed stable values of the properties found, with drop in the last two points.

In DSC curves, it was evident that the PLGA_high$T$ plates would have greater propensity to crystallize than PLGA_low$T$ plates due to their greater steric regularity

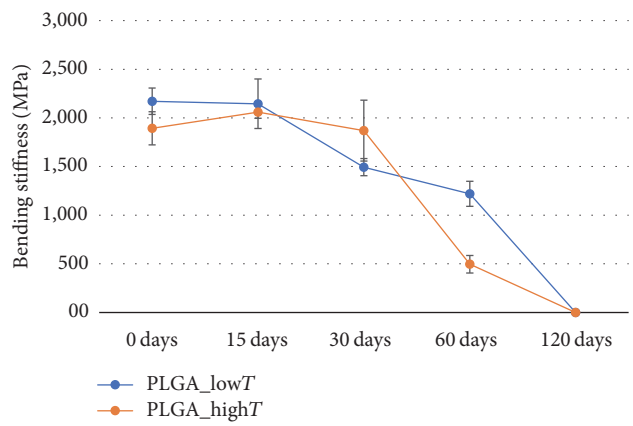

Figure 8: Bending stiffness along the hydrolytic degradation of PLGA_low$T$ and PLGA_high$T$ plates.

along the polymer chain during processability [33]. Injection molded PLGA_high$T$ and rapid cooling had the effect to reduce T_g by about 4°C. Furthermore, the cooling time (i.e., 90 s) of injection molding was the same for both plates' conditions. It means that the cooling rate to reach the temperature of the mold (23°C) was faster for PLGA_high$T$ plates. Because of this difference, different crystalline phases were formed, which may have resulted in the formation of different sizes of spherulites and irregular crystals in polymer structure [26, 34, 35].

Moreover, several polymers properties that are important in terms of their processability and applications are directly related to the specific molar mass. That could be related to the fact that mechanical, chemical, and physical properties are drastically affected by the crystallinity and especially by the low and high molar mass fractions. Devices for this application need to be deeper investigated to overcome complications on manufacturing and designs that could influence the degradation rate after placement such as properties stability.

5. Conclusion

We have proposed a work limit of temperatures (low and high) on medical devices as PLGA craniofacial plates

manufactured by injection molding and tested biomechanical function degradation of the two conditions of melt process temperature. Both working temperatures allowed producing craniofacial plates devices. At low and high temperature conditions (i.e., 240 and 280°C, resp.), the PLGA plates were evaluated for mechanical properties (apparent elastic modulus, maximum stress, and storage modulus) and crystallinity. The mechanical properties (i.e., 2.2 ± 0.1 and 1.9 ± 0.1 GPa of flexural stiffness) of the plate are suitable for osteosynthesis in non-load-bearing anatomical sites (e.g., craniofacial applications). The differences in crystallinity showed that we can choose the plate with degradation kinetics more suitable for the application. Based on all these results, we can conclude that the proposed process temperatures are adequate for the manufacture of PLGA craniofacial plates. In addition, the knowledge presented is useful to better understand the working limits of bioresorbable implants and the development of implant geometries with property control.

Conflicts of Interest

The authors declare that there are no conflicts of interest regarding the publication of this paper.

Acknowledgments

The authors would like to acknowledge PRONEX/FAPESC, CNPQ, and FINEP for financial support.

References

[1] R. Suuronen, P. E. Haers, C. Lindqvist, and H. F. Sailer, "Update on bioresorbable plates in maxillofacial surgery," *Facial Plastic Surgery*, vol. 15, no. 1, pp. 61–72, 1999.

[2] B. L. Eppley, "Use of resorbable plates and screws in pediatric facial fractures," *Journal of Oral and Maxillofacial Surgery*, vol. 63, no. 3, pp. 385–391, 2005.

[3] H. Peltoniemi, N. Ashammakhi, R. Kontio et al., "The use of bioabsorbable osteofixation devices in craniomaxillofacial surgery," *Oral Surgery, Oral Medicine, Oral Pathology, Oral Radiology, and Endodontics*, vol. 94, no. 1, pp. 5–14, 2002.

[4] R. E. Holmes, S. R. Cohen, G. B. Cornwall, K. A. Thomas, K. K. Kleinhenz, and M. Z. Beckett, "MacroPore resorbable devices in craniofacial surgery," *Clinics in Plastic Surgery*, vol. 31, no. 3, pp. 393–406, 2004.

[5] C. S. Leiggener, R. Curtis, and B. A. Rahn, "Effects of chemical composition and design of poly (L/DLLactide) implants on the healing of cranial defects," *Journal of Cranio-Maxillo-Facial Surgery*, vol. 26, p. 151, 1998.

[6] C. Schiller, C. Rasche, M. Wehmöller et al., "Geometrically structured implants for cranial reconstruction made of biodegradable polyesters and calcium phosphate/calcium carbonate," *Biomaterials*, vol. 25, no. 7-8, pp. 1239–1247, 2004.

[7] S.-H. Hyon, K. Jamshidi, and Y. Ikada, "Effects of Residual Monomer on the Degradation of DL-Lactide Polymer," *Polymer International*, vol. 46, no. 3, pp. 196–202, 1998.

[8] S. Ghosh, J. C. Viana, R. L. Reis, and J. F. Mano, "Effect of processing conditions on morphology and mechanical properties of injection-molded poly(L-lactic acid)," *Polymer Engineering and Science*, vol. 46, no. 7, pp. 1141–1147, 2007.

[9] J. C. Viana, N. M. Alves, and J. F. Mano, "Morphology and mechanical properties of injection molded poly(ethylene terephthalate)," *Polymer Engineering and Science*, vol. 44, no. 12, pp. 2174–2184, 2004.

[10] A. M. Harris and E. C. Lee, "Improving mechanical performance of injection molded PLA by controlling crystallinity," *Journal of Applied Polymer Science*, vol. 107, no. 4, pp. 2246–2255, 2008.

[11] H. Zhao and G. Zhao, "Mechanical and thermal properties of conventional and microcellular injection molded poly (lactic acid)/poly (ε-caprolactone) blends," *Journal of the Mechanical Behavior of Biomedical Materials*, vol. 53, pp. 59–67, 2016.

[12] J. C. Middleton and A. J. Tipton, "Synthetic biodegradable polymers as orthopedic devices," *Biomaterials*, vol. 21, no. 23, pp. 2335–2346, 2000.

[13] S. H. Barbanti, C. A. Zavaglia, and E. A. Duek, "Degradação acelerada de suportes de poli(épsilon-caprolactona) e poli(D,L-ácido láctico-co-ácido glicólico) em meio alcalino," *Polímeros*, vol. 16, no. 2, pp. 141–148, 2006.

[14] L. Lu, S. J. Peter, M. D. Lyman et al., "In vitro degradation of porous poly(L-lactic acid) foams," *Biomaterials*, vol. 21, no. 15, pp. 1595–1605, 2000.

[15] D. Bendix, "Chemical synthesis of polylactide and its copolymers for medical applications," *Polymer Degradation and Stability*, vol. 59, no. 1-3, pp. 129–135, 1998.

[16] S. Li, "Hydrolytic degradation characteristics of aliphatic polyesters derived from lactic and glycolic acids," *Journal of Biomedical Materials Research*, vol. 48, no. 3, pp. 342–353, 1999.

[17] E. W. Fischer, H. Goddar, and G. F. Schmidt, "Determination of degree of crystallinity of drawn polymers by means of density measurements," *Journal of Polymer Science Part A-2: Polymer Physics*, vol. 7, no. 1, pp. 37–45, 1969.

[18] R. T. MacDonald, S. P. McCarthy, and R. A. Gross, "Enzymatic degradability of poly(lactide): Effects of chain stereochemistry and material crystallinity," *Macromolecules*, vol. 29, no. 23, pp. 7356–7361, 1996.

[19] L.-T. Lim, R. Auras, and M. Rubino, "Processing technologies for poly(lactic acid)," *Progress in Polymer Science*, vol. 33, no. 8, pp. 820–852, 2008.

[20] D790 ASTM, *Standard Test Methods for Flexural Properties of Unreinforced and Reinforced Plastics and Electrical Insulating Materials*, ASTM International, West Conshohocken, PA, USA, 2015, https://www.astm.org/.

[21] S. Lyu and D. Untereker, "Degradability of polymers for implantable biomedical devices," *International Journal of Molecular Sciences*, vol. 10, no. 9, pp. 4033–4065, 2009.

[22] D. Zuchowska, D. Hlavatá, R. Steller, W. Adamiak, and W. Meissner, "Physical structure of polyolefin - starch blends after ageing," *Polymer Degradation and Stability*, vol. 64, no. 2, pp. 339–346, 1999.

[23] H. Essig, D. Lindhorst, T. Gander et al., "Patient-specific biodegradable implant in pediatric craniofacial surgery," *Journal of Cranio-Maxillofacial Surgery*, vol. 45, no. 2, pp. 216–222, 2017.

[24] A. U. Daniels, M. K. Chang, K. P. Andriano, and J. Heller, "Mechanical properties of biodegradable polymers and composites proposed for internal fixation of bone," *Journal of Applied Biomaterials*, vol. 1, no. 1, pp. 57–78, 1990.

[25] N. J. Ostrowski, B. Lee, A. Roy, M. Ramanathan, and P. N. Kumta, "Biodegradable poly(lactide-co-glycolide) coatings on magnesium alloys for orthopedic applications," *Journal of Materials Science: Materials in Medicine*, vol. 24, no. 1, pp. 85–96, 2013.

[26] P. Gentile, V. Chiono, I. Carmagnola, and P. V. Hatton, "An overview of poly(lactic-co-glycolic) Acid (PLGA)-based biomaterials for bone tissue engineering," *International Journal of Molecular Sciences*, vol. 15, no. 3, pp. 3640–3659, 2014.

[27] V. Hasirci, K. U. Lewandrowski, S. P. Bondre, J. D. Gresser, D. J. Trantolo, and D. L. Wise, "High strength bioresorbable bone plates: Preparation, Mechanical properties and in vitro analysis," *Bio-Medical Materials and Engineering*, vol. 10, no. 1, pp. 19–29, 2000.

[28] N. Ashammakhi, H. Peltoniemi, E. Waris et al., "Developments in craniomaxillofacial surgery: Use of self-reinforced bioabsorbable osteofixation devices," *Plastic and Reconstructive Surgery*, vol. 108, no. 1, pp. 167–180, 2001.

[29] R. B. Bell and C. S. Kindsfater, "The use of biodegradable plates and screws to stabilize facial fractures," *Journal of Oral and Maxillofacial Surgery*, vol. 64, no. 1, pp. 31–39, 2006.

[30] R. E. Lins, B. S. Myers, R. J. Spinner, and L. S. Levin, "A comparative mechanical analysis of plate fixation in a proximal phalangeal fracture model," *Journal of Hand Surgery*, vol. 21, no. 6, pp. 1059–1064, 1996.

[31] M. A. Woodruff and D. W. Hutmacher, "The return of a forgotten polymer—polycaprolactone in the 21st century," *Progress in Polymer Science*, vol. 35, no. 10, pp. 1217–1256, 2010.

[32] D. D. Wright, *Degradable Polymer Composites. In Encyclopedia of Biomaterials and Biomedical Engineering*, Marcel Dekker Inc, New York, NY, USA, 2004.

[33] W. S. Pietrzak, "Rapid cooling through the glass transition transiently increases ductility of PGA/PLLA copolymers: A proposed mechanism and implications for devices," *Journal of Materials Science: Materials in Medicine*, vol. 18, no. 9, pp. 1753–1763, 2007.

[34] J. Y. Nam, S. Sinha Ray, and M. Okamoto, "Crystallization behavior and morphology of biodegradable polylactide/layered silicate nanocomposite," *Macromolecules*, vol. 36, no. 19, pp. 7126–7131, 2003.

[35] S. Farè, P. Torricelli, G. Giavaresi et al., "In vitro study on silk fibroin textile structure for Anterior Cruciate Ligament regeneration," *Materials Science and Engineering C*, vol. 33, no. 7, pp. 3601–3608, 2013.

Hindawi
International Journal of Biomaterials
Volume 2017, Article ID 6435076, 8 pages
https://doi.org/10.1155/2017/6435076

Research Article

Influence of Processing Conditions on the Mechanical Behavior and Morphology of Injection Molded Poly(lactic-co-glycolic acid) 85:15

Liliane Pimenta de Melo,[1,2] Gean Vitor Salmoria,[1,2] Eduardo Alberto Fancello,[1,3] and Carlos Rodrigo de Mello Roesler[1]

[1] *Biomechanical Engineering Laboratory (LEBm), University Hospital (HU), Federal University of Santa Catarina, 88040-900 Florianópolis, SC, Brazil*
[2] *Laboratory of Innovation on Additive Manufacturing and Molding (NIMMA), Federal University of Santa Catarina, 88040-900 Florianópolis, SC, Brazil*
[3] *GRANTE, Department of Mechanical Engineering, Federal University of Santa Catarina, 88040-900 Florianópolis, SC, Brazil*

Correspondence should be addressed to Liliane Pimenta de Melo; liliane.eng@gmail.com

Received 3 May 2017; Accepted 19 June 2017; Published 7 August 2017

Academic Editor: Jie Deng

Copyright © 2017 Liliane Pimenta de Melo et al. This is an open access article distributed under the Creative Commons Attribution License, which permits unrestricted use, distribution, and reproduction in any medium, provided the original work is properly cited.

Two groups of PLGA specimens with different geometries (notched and unnotched) were injection molded under two melting temperatures and flow rates. The mechanical properties, morphology at the fracture surface, and residual stresses were evaluated for both processing conditions. The morphology of the fractured surfaces for both specimens showed brittle and smooth fracture features for the majority of the specimens. Fracture images of the notched specimens suggest that the surface failure mechanisms are different from the core failure. Polarized light techniques indicated birefringence in all specimens, especially those molded with lower temperature, which suggests residual stress due to rapid solidification. DSC analysis confirmed the existence of residual stress in all PLGA specimens. The specimens molded using the lower injection temperature and the low flow rate presented lower loss tangent values according to the DMA and higher residual stress as shown by DSC, and the photoelastic analysis showed extensive birefringence.

1. Introduction

Implants for medical applications using resorbable polymers derived from a class of aliphatic polyesters, polyhydroxy acids, are widely used for internal fracture fixation, wound closure, sutures, small vessel ligation, and drug delivery [1, 2]. During the injection molding process, polymeric materials undergo complex thermomechanical histories and significant changes in their rheological, mechanical, and thermochemical properties due to the large pressure variations, cooling times, mold geometry, and the manufacturing process [3–7]. The polymer's mechanical properties (apparent elastic modulus, maximum strength), morphology, crystallinity, and frozen layer thickness are also influenced by injection molding parameters, such as the melting process temperature, injection flow rate, holding pressure, mold temperature, and average bulk temperature [2, 8–11]. Poly(glycolide) and poly(L-lactide-co-glycolide), which are the synthetic copolymers of lactic acid (α-hydroxypropionic acid) and glycolic acid (hydroxyacetic acid), respectively, have good fiber-forming properties but their thermomechanical histories influence the ductility and degradability of the corresponding manufactured devices [12, 13].

The crystallinity and frozen layer thickness are controlled by the combined effect of the cooling rate and the stress fields imposed during the melting process [14–16]. Viana and collaborators [5] concluded that the thickness of the PLLA frozen layer increases with the stress level and decreases with temperature, while its degree of crystallinity increases with both shear stresses and temperature. On the other hand, Pantani et al. (2005) [17] indicated that the poly(acid

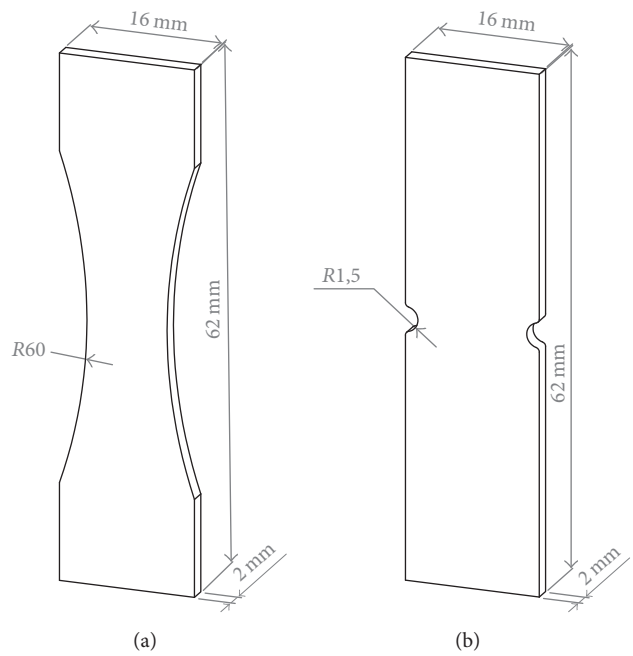

Figure 1: Illustration of the specimen's geometries used for injection molding: unnotched specimen (a) and notched specimen (b).

lactide) frozen layer thickness increased when either the flow rate or the mold temperature decreased and that a correlation existed between the two parameters. Residual stresses and molecular orientations throughout a product provide important information about how that product will perform. Residual stresses are introduced by nearly all techniques used for polymer manufacturing and they can also be introduced by nonuniform flow, differential packing, or cooling. Therefore, an assessment of the mechanical behavior and structural characteristics of PLGA resulting from distinct injection molding parameters of absorbable polymers can provide valuable information.

This study provided an overview among processing conditions, morphology, and mechanical property relationship of injection molded PLGA. Two specimen groups with different geometries (notched and unnotched) were injection molded using two melting temperatures and flow rates (low and high). These choices generated four different processing conditions for both groups. For each processing condition, the mechanical properties (apparent elastic modulus, ultimate strength, elongation at failure, storage modulus, and loss tangent), morphology at fracture surface, and residual stress were evaluated.

2. Experimental

2.1. Materials. Poly(lactic-co-glycolic acid) 85/15 granules, commercially available as Purasorb PLG 8531, purchased from Corbion Purac Biomaterials (Holland), were used in this study. The PLGA 85/15 average molecular weight of Mn = 224,271 g/mol and polydispersity of 1.87 were determined using Gel Permeation Chromatography (GPC) (Viscotek VE 2001, Viscotek detector TDA 302, USA, 2008). This copolymer has T_g of 57 ± 1°C, T_m = 140°C, and 3.04 dL/g of intrinsic viscosity (chloroform, 25°C, c = 0.1 g/dL).

Table 1: Injection molding conditions for notched and unnotched PLGA specimens.

Injection condition	T (°C)	Q (cm^3 s^{-1})
I	240	25
II	240	10
III	210	25
IV	210	10

2.2. Injection Molding Specimens. PLGA pellets were injection molded with an ARBURG 270S/250-70 machine into two groups of specimen geometries, notched and unnotched, adapted from ASTM D1822 type S and ASTM D638 type V. Both groups had a rectangular format of 62 × 16 mm of length and a cross section of 10 × 2 mm. Notched specimens had a 1.5 mm notch radius (stress concentration factor of 2.4), while unnotched specimens had a narrower section with a radius of 60 mm (see Figure 1).

Two (low and high) melt injection temperatures and two injection (low and high) flow rates were investigated, generating four injection conditions shown in Table 1.

The other processing parameters had the following fixed values: mold temperature: 25°C, injection pressure: 1500 MPa, holding pressure: 25 MPa, injection time: 2 s, cooling time: 90 s, and screw speed: 100 rpm.

Table 2: Mechanical properties of notched and unnotched PLGA specimens injected with different molding conditions.

	Injection condition	T_{inj} (°C)	Q_{inj} ($cm^3\,s^{-1}$)	E (GPa)	σ_u (MPa)	ε_f (%)
Notched	I	240	25	5.6 ± 0.4	63.1 ± 1.2	2.7 ± 0.3
	II	240	10	4.8 ± 0.2	65.5 ± 1.4	3.3 ± 0.5
	III	210	25	4.8 ± 0.4	54.0 ± 11.0	1.9 ± 1.0
	IV	210	10	4.8 ± 0.3	67.6 ± 0.7	4.5 ± 0.3
Unnotched	I	240	25	3.5 ± 0.1	63.4 ± 1.1	4.34 ± 1.9
	II	240	10	3.4 ± 0.1	62.3 ± 2.3	7.1 ± 4.3
	III	210	25	3.7 ± 0.2	62.3 ± 3.0	3.4 ± 2.0
	IV	210	10	4.0 ± 0.3	64.9 ± 1.1	4.9 ± 1.1

2.3. Mechanical Characterization

2.3.1. Tensile Test. The two different specimens were tested in an EMIC testing machine, model DL-3000, in the tensile mode as per ISO 527-1. The elongation of the specimens was measured using an extensometer, Instron/EMIC 2630-107. The tests were performed using a moving grip speed of 1 mm min^{-1} at a controlled room temperature of 23°C. Six specimens ($n = 6$) for each condition for each group were tested. The mechanical properties investigated were the apparent elastic modulus (taken as the initial slope of the engineering stress-strain curve) E, ultimate strength (maximum stress value of the engineering stress-strain curve) σ_u, and engineering strain at failure ε_f.

2.3.2. Dynamical Mechanical Analysis. A DMA-Q800 analyzer (TA Instruments) with a single cantilever clamp was used for the viscoelastic tests. Dynamic mechanical analysis (DMA) provided the storage modulus E' and $\tan\delta$ values at a frequency of 1 Hz within the temperature range of 30°C to 120°C using a heating rate of 3°C/min and a transversal displacement amplitude of 0.3% of the effective length of the specimen.

2.4. Scanning Electronic Microscopy. Scanning Electronic Microscopy (SEM) analysis was used to evaluate the fractured surface of the PLGA (85/15) specimens submitted to the tensile test and also to observe the frozen layer thickness and other morphological characteristics such as molecular orientation of shear force caused by molding injection. The analysis was conducted on all conditions of injection molding for the two groups of specimens.

In order to obtain good quality PLGA images, the specimens were fixed to a support with a double-sided carbon tape. For electronic conductivity, the specimens were covered with a thin layer of gold in a sputter model D2 Diode Sputtering System, manufactured by ISI (International Scientific Instruments). The fractured surfaces and thicknesses were observed using a JEOL JSM-6390LV (FEI Company, Japan) scanning electron microscope with an accelerating voltage of 5 kV.

2.5. Differential Scanning Calorimetry and Residual Stress Analysis. Differential scanning calorimetry (DSC) was used to determine the thermal transitions and residual stress enthalpy of the injection molded PLGA specimens in a Shimadzu DSC-6000 with nitrogen atmosphere (19 $cm^3\,m^{-1}$), using aluminum oxide as standard. The heating rate was from 10°C to 250°C at 10°C m^{-1}, using an average sample weight of 7 mg taken from the central region of the molded specimens. The residual stresses of the manufactured specimens were also evaluated by the polarized light technique using a polariscope with polarizing and quarter-wave lenses of 250 mm diameters, following the ASTM D4093 [18].

2.6. Data Analysis. Analysis of variance (ANOVA) was performed considering statistical significance set at 0.05; the p value was investigated for significance of the factors among injection molding conditions. All data are reported as mean ± standard deviation.

3. Results and Discussion

The processing conditions were systematically varied following a DOE array involving notch presence on geometry, melt temperature, and flow rate. Mechanical properties, as apparent elastic modulus, ultimate strength, elongation at failure, storage modulus, and loss tangent, were estimated by tensile test and DMA. The two morphological parameters, morphology at fracture surface and residual stress, were interpreted by the thermomechanical parameters. ANOVA was performed to measure statistically the significant response. The relationships between the morphology and mechanical properties were then established.

3.1. Tensile Test. Figure 2 shows the curves for stress versus strain for the notched and unnotched molded specimens using low and high values of melt injection temperatures and the two injection flow rates.

Table 2 contains the average values of E, σ_u, and ε_f at each injection condition for both notched and unnotched groups. Similar mechanical properties were found for the injected PLGA specimens that were molded under different processing parameters (notched or unnotched samples), as shown in Table 2. But there is an evident difference between notched and unnotched samples relative to the apparent elastic modulus E mechanical property. The apparent elastic modulus E and ultimate strength σ_u show low sensitivity to the injection conditions for both the notched and the

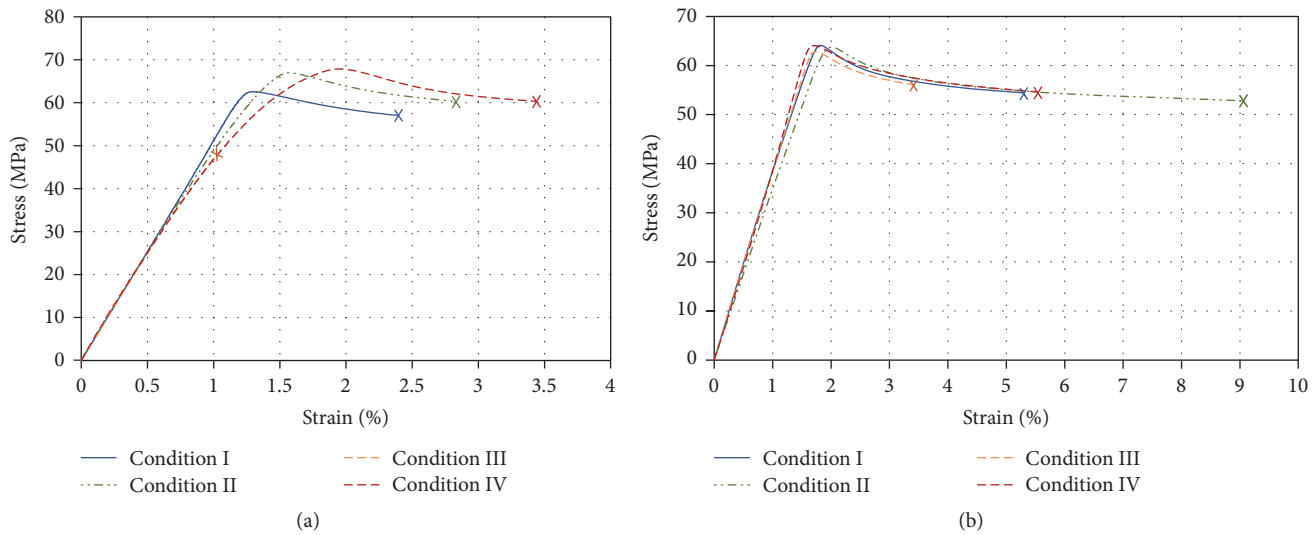

Figure 2: Stress-strain curves (means) of notched (a) and unnotched (b) specimens of injection molded PLGA.

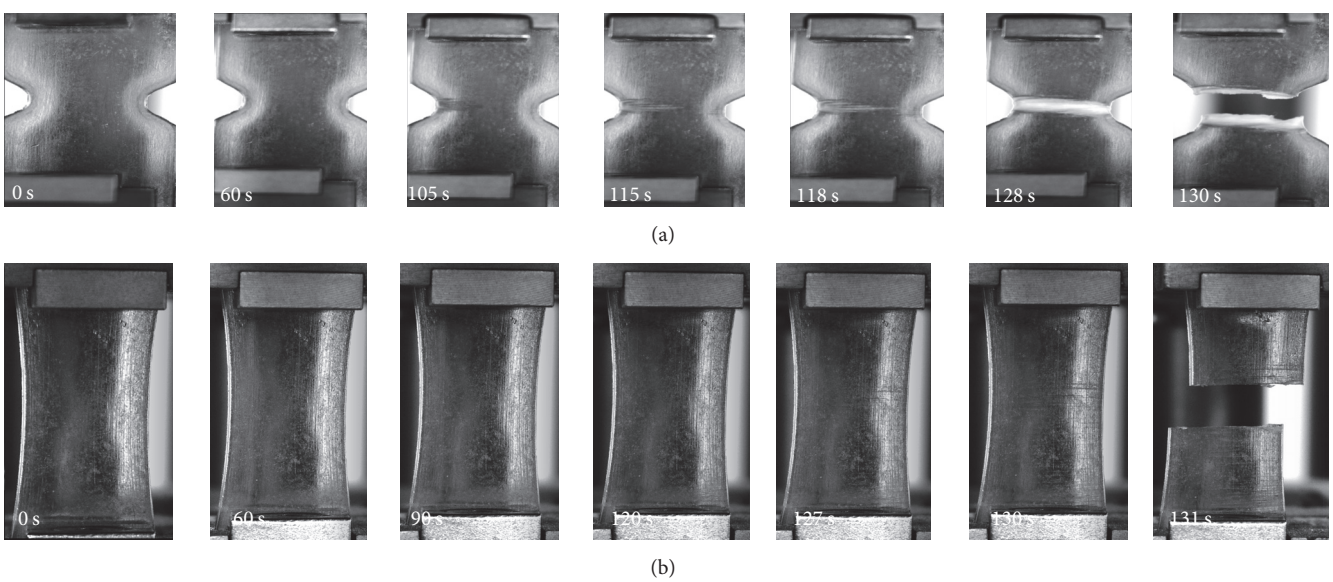

Figure 3: Sequence of images of tensile test for notched (a) and unnotched (b) specimens injected under Condition I.

unnotched groups of specimens. However, there was a high standard deviation found for σ_u in the notched group injected under Condition III (see Table 2).

This low sensitivity reveals a certain level of material toughness. In order to achieve nearly the same value of σ_u for both geometries, the material localized near the notch valley seems to allow plastic deformation during loading to finally reach an almost constant stress distribution prior to the occurrence of a complete cross section (plastic) collapse. On the other hand, it is important to note that specimens, even those injected under the same conditions, showed different macroscopic behaviors at failure. While some showed a clear necking formation, others fractured without this formation. This observation is consistent with the large standard deviation found for ε_f.

Sensitivity to the injection conditions showed that strains at failure presented slightly higher mean values for Conditions II and IV (low injection flow rates) than for Conditions I and III (high injection flow rates), for both notched and unnotched groups.

3.2. Scanning Electronic Microscopy. Figure 3 presents a sequence of images that illustrate the progressive localization (necking) of strains prior to total failure of one of the notched specimens injected under Condition I. In these pictures, the capacity of the material to withstand plastic strain is macroscopically visible, as was already mentioned when discussing ultimate strength σ_u.

Unnotched specimens, as Figure 3 shows, present elongation along the specimen with longitudinal spread failure

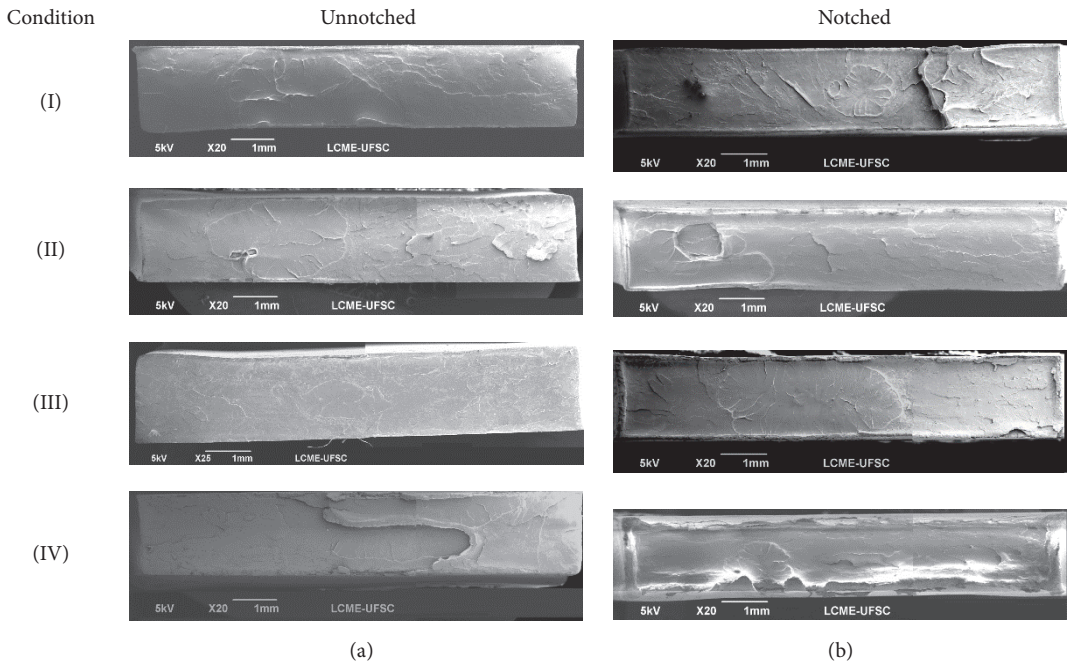

Figure 4: SEM of fractured surface unnotched (a) and notched (b) PLGA specimens molded under different processing conditions.

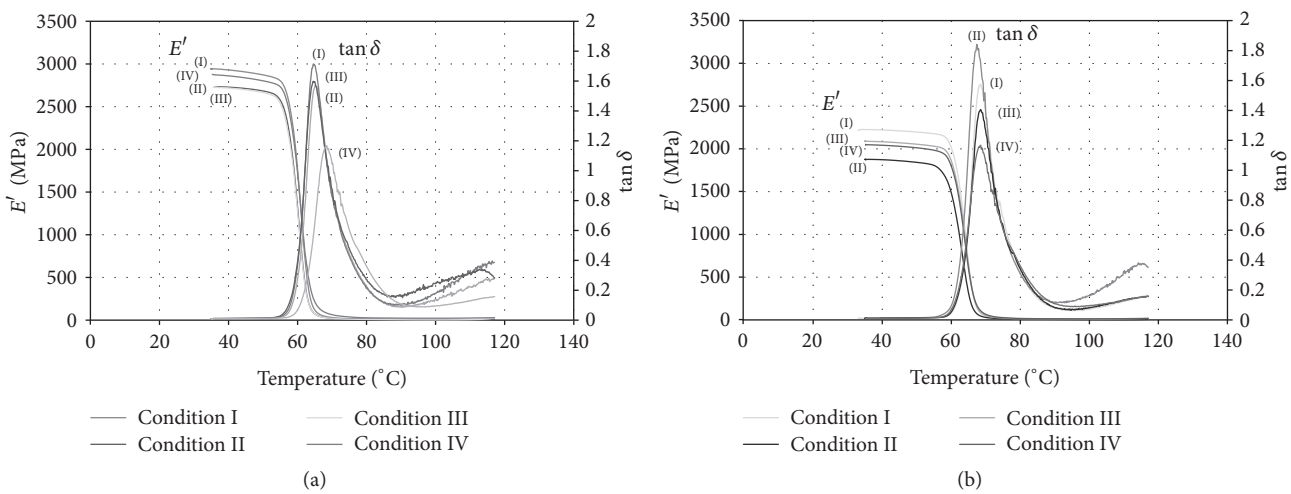

Figure 5: Storage modulus and loss tangent as a function of temperature for PLGA specimen injection molded under different conditions (I, II, III, and IV). Curve for unnotched (a) and notched (b) specimens.

after 60 s, while notched specimens present stretching in the center region due to the stress concentrator (e.g., notch). Although there were different behaviors, the brittle feature of the material occurs in both geometries (see Figure 4).

It is worth emphasizing once more that a different macroscopic behavior at failure was observed even in specimens injected under the same condition; while some specimens presented clear necking formation, others failed without this formation showing flatter fracture surfaces (Figure 3).

SEM images of fractured surfaces are shown in Figure 4. These images are representative of those samples that did not show a clear necking formation. In these figures, it is possible to see flat fractured surfaces with some evidence of localized plastic flow, mainly in the notched specimens. The plastic fractures along the borders of the notched specimens are clear. This can be related to a different behavior between the core and borders and is due to the existence of the frozen layer. The existence of a thicker frozen layer in this group of specimens seems to be consistent with the fact that thicker frozen layers are related to higher flow rates as seen in the notched region of this group.

3.3. Dynamical Mechanical Analysis. Figure 5 shows representative curves of storage modulus E' and $\tan\delta$ ($\tan\delta = E''/E'$) as functions of temperature for notched and unnotched specimens.

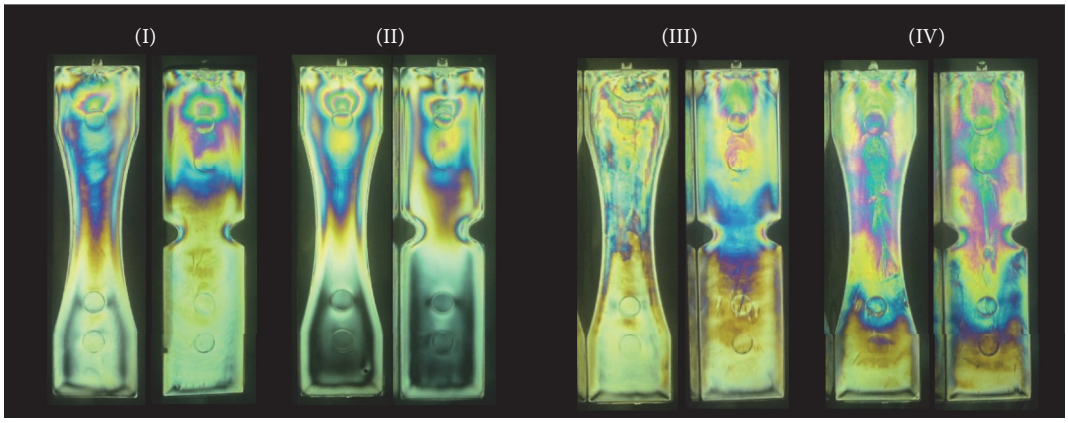

Figure 6: Photoelastic fringes of notched and unnotched specimens for Conditions I, II, III, and IV.

Table 3: Relaxation enthalpy values for PLGA specimens determined by DSC.

PLGA specimens	Condition I	Condition II	Condition III	Condition IV
Unnotched	2.8 (±0.3) J/g	4.2 (±0.6) J/g	3.7 (±0.3) J/g	3.8 (±0.5) J/g
Notched	3.6 (±0.2) J/g	3.7 (±0.5) J/g	5.2 (±0.3) J/g	4.5 (±0.4) J/g

Sensitivity of the storage modulus to the injection conditions did not show a clear trend in the notched and unnotched specimens. Remember that due to the differences in geometry the storage moduli of the notched and unnotched specimens are not comparable. The only visible response is the lowest value of the loss tangent ($\tan\delta$) reached by Condition IV (lower temperature and flow rate) for both notched and unnotched geometries, characterizing lower dissipation due to viscous micromechanisms.

Moreover, DMA was carried out to characterize the resulting copolymer in the four conditions. As shown in Figure 5, one obvious transition behavior was observed, designated as relaxation. It is well known that the glass transition temperature (T_g) of a polymer can be determined by relaxation, as it is usually related to the segment movements in the noncrystalline area. This behavior, associated with broad peaks, nonexisting in a second heating scan, is characteristic of an incomplete crosslink process of copolymers formulations. In fact, $\tan\delta$ also indicates the composite damping capacity, which has a maximum value at the amorphous transition. As a PLGA copolymer, a possible reason why the curves went up above 100°C is the presence of residual monomers.

3.4. Differential Scanning Calorimetry and Residual Stress Analysis. The injection molding of transparent polymers can induce a peculiar stress field that is clearly detected by photoelastic stress analysis [18, 19]. In Figure 6, the isochromatic maps for notched and unnotched specimens are shown. Notably, the isochromatic fringes have an asymmetric pattern distribution. This means that injection molding imposed an asymmetric thermomechanical environment onto the injected polymer that is related to the concentration of residual stresses near the injection gate.

The stress concentration decreases uniformly on the opposite side of the specimen at a different rate for each molding condition. The residual stresses arise during the filling and the packing processes. The wide distribution of residual stresses present in the specimens molded with the lower temperature is probably due to the nonuniform shear stress during cavity filling and rapid solidification. On the other hand, the concentrated residual stresses near the gate present in the specimens molded with the higher temperature are due to the compressive force caused by the holding pressure during the slower solidification.

In terms of stress shielding, Condition IV is the most propulsive to show a different behavior, since Condition 4 presents the lower temperature and lower flow rate. Then, the mold filling during injection molding along the specimen exhibited different characteristics due to the high shear stress between the polymer and the wall of the mold. The shear stress causes different lines of residual stress between notched and unnotched specimens.

DSC curves (Figure 7) show the transitions for the PLGA pellets and for the PLGA molded specimens under different conditions. The molded specimen curves present a clear endothermic peak together with the glass transition related to the stress relaxation enthalpy of PLGA [20]. The residual stress was determined by measuring this relaxation enthalpy peak area at glass transition and is presented in Table 3. The relaxation enthalpy values were higher for the notched specimens molded under Conditions III and IV; that is, the lower temperature resulted in higher residual stresses at the center of the specimens in the notched region.

The DSC curves evidence the difference in the endothermic peaks and the presence of crystallinity only for Condition II. For this condition, a shoulder indicating two melting temperatures is present, related to PGA (15%) and PLA (85%)

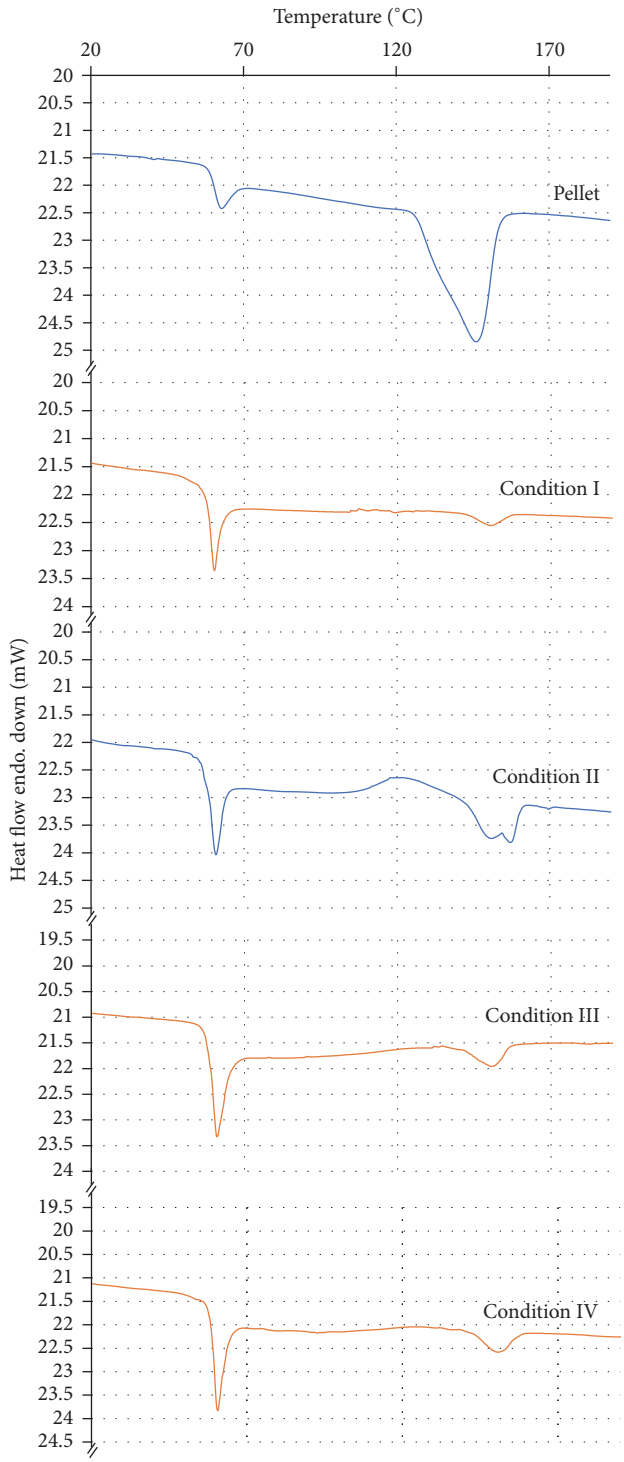

Figure 7: Calorimetry curves for PLGA pellets and molded specimens under different process conditions (I, II, III, and IV).

fractions, respectively, even though this value is very close to the detected T_m.

Moreover, it is possible for residual stress to be reduced or eliminated with heat treatment to avoid influencing mechanical properties and fracture surface morphology of PLGA specimens. The present DSC curves are about the processed specimens without any treatment to show the results of the injection molding process. Heat treatment after the manufacturing of the devices in medical applications could possibly cause degradation of the material.

4. Conclusion

Similar mechanical properties were found for the injected PLGA specimens that were molded under different

processing parameters. The melt temperature can influence the injection molded device and can be influenced by other parameters of injection molding. Flow rate is strongly associated with the shear rate and therefore has effects on melt temperature, molecular orientation, strains at failure, and residual stresses. The morphology of fractured surfaces of the notched and unnotched specimens showed flat and smooth fractures for the majority of the specimens. The macroscopic mechanical behavior of the injected specimens presented low notch sensitivity, suggesting the existence of a certain level of material toughness. The strains at failure presented slightly higher mean values for Conditions II and IV (low injection flow rate) than for Conditions I and III (high injection flow rate), for both notched and unnotched specimens. There were localized deformations near the specimen surface different from the core region. This can be related to the orientation of the skin layer, especially in the notched specimens. Polarized light techniques indicated birefringence throughout all specimens, especially in those molded under lower temperature, which suggests residual stress due to rapid solidification. DSC analysis confirmed the existence of residual stress in all PLGA specimens. The specimens molded using the lower injection temperature and lower flow rate (Condition IV) presented lower loss tangent values according to DMA and higher residual stress as shown by DSC, and photoelastic analysis demonstrated extensive birefringence along the specimen. Molecular restriction in the chain rotation and conformation due to the thick oriented skin layer can explain the less viscous behavior observed.

Conflicts of Interest

The authors declare that there are no conflicts of interest regarding the publication of this paper.

Acknowledgments

The authors would like to thank PRONEX/FAPESC, CNPQ, and FINEP for financial support and the Center of Microscopy, UFSC, for providing the micrographs.

References

[1] L. Fambri, C. Migliaresi, K. Kesenci, and E. Piskin, "Biodegradable polymers," in *Integrated Biomaterials Science*, R. Barbucci, Ed., pp. 119–187, Kluwer Academic/Plenum Publishers, New York, USA, 2002.

[2] J. W. Leenslag, A. J. Pennings, R. R. M. Bos, F. R. Rozema, and G. Boering, "Resorbable materials of poly(l-lactide). VI. Plates and screws for internal fracture fixation," *Biomaterials*, vol. 8, no. 1, pp. 70–73, 1987.

[3] S. Ghosh, J. C. Viana, R. L. Reis, and J. F. Mano, "Effect of processing conditions on morphology and mechanical properties of injection-molded poly(L-lactic acid)," *Polymer Engineering and Science*, vol. 46, no. 7, pp. 1141–1147, 2007.

[4] D. Cardozo, "Three Models of the 3D Filling Simulation for Injection Molding: A Brief Review," *Journal of Reinforced Plastics and Composites*, vol. 27, pp. 1963–1974, 2008.

[5] J. C. Viana, A. M. Cunha, and N. Billon, "The thermomechanical environment and the microstructure of an injection moulded polypropylene copolymer," *Polymer*, vol. 43, no. 15, pp. 4185–4196, 2002.

[6] S.-L. Yang, Z.-H. Wu, W. Yang, and M.-B. Yang, "Thermal and mechanical properties of chemical crosslinked polylactide (PLA)," *Polymer Testing*, vol. 27, no. 8, pp. 957–963, 2008.

[7] L.-T. Lim, R. Auras, and M. Rubino, "Processing technologies for poly(lactic acid)," *Progress in Polymer Science*, vol. 33, no. 8, pp. 820–852, 2008.

[8] C. D. Han, *Rheology and Processing of Polymeric Materials*, vol. 1, Polymer Technology Oxford University Press, New York, USA, 2007.

[9] D. F. Gibbons, "Tissue response to resorbable synthetic polymers," in *Degradation Phenomena on Polymeric Biomaterials*, H. Planck, M. Dauner, and M. Renardy, Eds., pp. 97–104, Springer, New York, USA, 1992.

[10] S. Ghosh, J. C. Viana, R. L. Reis, and J. F. Mano, "Bi-layered constructs based on poly(l-lactic acid) and starch for tissue engineering of osteochondral defects," *Materials Science and Engineering C*, vol. 28, no. 1, pp. 80–86, 2008.

[11] H. Ben Daly, B. Sanschagrin, K. T. Nguyen, and K. C. Cole, "Effect of polymer properties on the structure of injection-molded parts," *Polymer Engineering & Science*, vol. 39, no. 9, pp. 1736–1751, 1999.

[12] T. Kijchavengkul, R. Auras, M. Rubino, S. Selke, M. Ngouajio, and R. T. Fernandez, "Biodegradation and hydrolysis rate of aliphatic aromatic polyester," *Polymer Degradation and Stability*, vol. 95, no. 12, pp. 2641–2647, 2010.

[13] G. L. Racey, W. R. Wallace, C. J. Cavalaris, and J. V. Marguard, "Comparison of a polyglycolic-polylactic acid suture to black silk and plain catgut in human oral tissues," *Journal of Oral Surgery*, vol. 36, no. 10, pp. 766–770, 1978.

[14] S.-H. Hyon, K. Jamshidi, and Y. Ikada, "Synthesis of polylactides with different molecular weights," *Biomaterials*, vol. 18, no. 22, pp. 1503–1508, 1997.

[15] A. M. Brito, A. M. Cunha, A. S. Pouzada, and R. J. Crawford, "Predicting the Skin-Core Boundary Location in Injection Moldings," *International Polymer Processing*, vol. 4, pp. 307–404, 1991.

[16] H.-C. Kuo and M.-C. Jeng, "Effects of part geometry and injection molding conditions on the tensile properties of ultra-high molecular weight polyethylene polymer," *Materials and Design*, vol. 31, no. 2, pp. 884–893, 2010.

[17] R. Pantani, I. Coccorullo, V. Speranza, and G. Titomanlio, "Modeling of morphology evolution in the injection molding process of thermoplastic polymers," *Progress in Polymer Science*, vol. 30, no. 12, pp. 1185–1222, 2005.

[18] ASTM, "Standard test method for photoelastic measurements of birefringence and residual strains in transparent or translucent plastic materials," ASTM D4093, ASTMA, Consshohocken, PA, USA, 2014.

[19] W. Dally and F. R. William, *Experimental Stress Analysis*, College House Enterprises, LLC, New York, third edition, 1991.

[20] W. S. Pietrzak, "Rapid cooling through the glass transition transiently increases ductility of PGA/PLLA copolymers: A proposed mechanism and implications for devices," *Journal of Materials Science: Materials in Medicine*, vol. 18, no. 9, pp. 1753–1763, 2007.